Master's thesis

NTNU
Norwegian University of Science and Technology
Faculty of Information Technology and Electrical Engineering
Department of Electric Power Engineering

Mathias Melby

Comparison of virtual oscillator control and droop control in an inverter-based stand-alone microgrid

Master's thesis in Energy and Environmental Engineering
Supervisor: Olav Bjarte Fosso and Marta Molinas
June 2019

NTNU
Norwegian University of
Science and Technology

Mathias Melby

Comparison of virtual oscillator control and droop control in an inverter-based stand-alone microgrid

Master's thesis in Energy and Environmental Engineering
Supervisor: Olav Bjarte Fosso and Marta Molinas
June 2019

Norwegian University of Science and Technology
Faculty of Information Technology and Electrical Engineering
Department of Electric Power Engineering

NTNU
Kunnskap for en bedre verden

Abstract

This thesis is about controlling DC/AC inverters. More specifically is the goal to compare the recently introduced virtual oscillator control (VOC) with the better known droop control. The methods are analyzed under different conditions to uncover their limitations and their strengths. It also presented how the selection parameters could make the methods equivalent. This is used as a criterion to give a fair comparison. During the analysis were some improvements of the VOC discovered, and the method was optimized to improve its performance.

To compare the controllers, were both methods implemented on parallel connected inverters in a simulation model of a stand-alone microgrid. The model consisted of two inverters supplying one common load with either virtual oscillator control or droop control applied. Both methods were set to function similarly in steady-state to ensure fair comparison on equal terms. The comparison was performed by developing time-step simulation models in MATLAB/Simulink as well as equivalent small-signal state-space representations. This way, both the steady-state behavior, the transient characteristics, and the robustness of the control methods were investigated.

One of the main differences between the control methods is related to the coupling strength between the inverters. This factor is inversely proportional to the impedance between the inverters and determines how strongly they affect each other. The analysis show that the droop controller is at its best when it operates without the inverters having a large influence on each other. When the line impedance was reduced the stability margin decreased, and when the impedance was one tenth of the base value the droop-controlled system became unstable. The virtual oscillator control, on the other hand, benefits from a tighter coupling as the system's stability margin increases with a reducing line impedance. Furthermore, the virtual oscillator-controlled system was stable for all operating conditions tested in this work. Hence, the virtual oscillator control is a more robust method.

The increased robustness entails a lower voltage quality. Whereas the droop controller provides a pure sinus waveform as a reference voltage, the virtual oscillator control gives a slightly deteriorated voltage shape as well as an oscillating instantaneous frequency. Even though the virtual oscillator control was tuned to optimize its performance, the droop controller would still be a smarter alternative for the simulated microgrid as the voltage quality and the preciseness of the frequency and voltage control were better.

Therefore, if the microgrid has a high impedance grid, either due to a long distance between the units or because of a large resistivity, it has not been found sufficient grounds to choose the VOC over the droop control. On the other hand, if there is a strong coupling between the inverters, the virtual oscillator control would be the better alternative.

Sammendrag

Denne oppgaven tar for seg regulering og styring av DC/AC-omformere. Mer spesifikt er målet med oppgaven å sammenligne en nyere kontrollmetode, kalt virtuell oscillatorkontroll (VOC), med den bedre kjente droopkontrollen. I sammenligningen er metodene analysert under flere ulike forhold for å finne ut metodenes begrensninger samt hvilke områder de er gode på. Det er også presentert hvordan parameterne til de to metodene kan velges for å gjøre metodene ekvivalente. Dette ble brukt som et kriterium for å kunne gi en rettferdig sammenligning. Underveis i analysen ble enkelte forbedringspotensialer av VOC oppdaget, og metoden optimalisert for å oppnå en forbedret ytelse.

For å sammenligne kontrollsystemene, ble begge metodene implementert på parallellkoblede omformere i en simuleringsmodell av et isolert mikronett. Modellen besto av to strømkilder med hver sin omformer som leverte effekt til en felles last hvor enten VOC eller droop-kontroll ble brukt. Testene på modellen ble utført med programmet MATLAB/Simulink i tillegg til at en ekvivalent tilstandsrommodell ble analysert. Slik kunne både den stasjonære og den transiente oppførselen bli undersøkt i tillegg til at stabiliteten til kontrollmetodene kunne bli vurdert.

En av hovedforskjellene mellom kontrollmetodene som ble oppdaget var relatert til hvor sterkt omformerne var knyttet sammen. Denne koblingsfaktoren er invers proporsjonal med den elektriske motstanden mellom omformerne og bestemmer hvor sterkt de påvirker hverandre. Analysene viste at droop-kontrollen var best når det var liten påvirkning mellom omformerne. Når linjeimpedansen ble redusert, sank stabilitetsmarginen og når impedansen var redusert til en tiendedel av opprinnelig verdi ble systemet ustabilt med droop-kontrollen. Det motsatte var tilfellet med virtuell oscillatorkontroll som fikk større stabilitetsmargin når koblingsfaktoren økte i styrke. I tillegg var VOC stabil for alle de forhold som ble undersøkt i oppgaven. Det viser at virtuell oscillatorkontroll er en mer robust metode enn droop-kontroll.

Den økte robustheten med VOC medfører en dårligere spenningskvalitet. Droop-kontrollen gir en ren sinusformet referansespenning til omformeren mens virtuell oscillatorkontroll gir en delvis forringet form på referansespenningen samt en oscillerende momentan frekvens. Selv om VOC-metoden ble tunet til å optimere ytelsen sin, var det tydelig at droop-kontrolleren ville være et bedre alternativ for mikronettet på grunn av den relativt store motstanden det var definert med. Dette fordi både spenningskvaliteten og nøyaktigheten på frekvens- og spenningskontrollen var bedre.

Derfor kan det konkluderes med at for et mikronett med stor motstand i nettet, enten på grunn av lang avstand mellom produksjonsenhetene eller en høy resistivitet i overføringslinjene, har det ikke blitt funnet gode nok grunner for å velge virtuell oscillatorkontroll i stedet for droop-kontroll. Hvis det i stedet er lav motstand i nettet og dermed en sterk kobling mellom enhetene, vil virtuell oscillatorkontroll være det beste alternativet.

Preface

This report is the delivery of my master thesis at the Department of Electric Power Engineering at the Norwegian University of Science and Technology (NTNU). The work is valued at 30 ECTS and has lasted a full semester. The delivery is a continuation of my specialization project titled ”Comparison of peer-to-peer droop control and virtual oscillator control of inverters in a stand-alone microgrid” completed in the fall of 2018.

I wish to thank my supervisors Prof. Marta Molinas and Prof. Olav Bjarte Fosso. Thank you for your guidance, commitment to perform thorough research, question the results and inspire me to never settle but always seek to expand my knowledge. I also want to thank you for giving me the opportunity to work with this interesting topic, it has been an exciting journey.

I also wish to express my gratitude to Prof. Jon Are Suul and Dr. Zhang Chen who were outermost helpful and assisted me in the derivation of the complex state-space representations.

Lastly, I would like to thank my girlfriend Amalie. I am grateful for your moral support, your ability to cope with me during stressful times, and how you always light up my days.

Trondheim, June 8th, 2019
Mathias Melby

Contents

List of Figures

List of Tables

List of Abbreviations

VSI	Voltage Source Inverter
VO	Virtual Oscillator
VOC	Virtual Oscillator Control
PWM	Pulse Width Modulated
RMS	Root Mean Square
PI	Proportional Integral
pu	Per Unit
AC	Alternating Current
DC	Direct Current
PV	Photo Voltaic
THD	Total Harmonic Distortion
KVL	Kirchhoff's Voltage Law
KCL	Kirchhoff's Current Law

1 Introduction

Microgrids are confined areas of the electric grid that can be either connected to the main grid or operate in island mode. When operating alone, the load is supplied by local distributed generation while in connected mode some or all of the demand is met by the external grid. Microgrids might become an important part of the electric grid in the future because it enables more direct control of unpredictable renewable energy sources. This is beneficial in a broad view as the stability of the power system depends on a constant balance between production and demand for electricity. This is also beneficial for the customers in the microgrid as the switching possibility results in a robust system where the power flow is uninterrupted if a fault would occur in the main grid.

Since several of the distributed generations sources produce power with a direct current (DC), they need to be connected to an inverter in order to transform the voltage into alternating current (AC) before transferring the power to the load. A multiple of sources at different locations requires a multiple of inverters. Such parallel-connected inverters are therefore key in the development of microgrids.

In order to operate the parallel-connected inverters, specific control techniques are needed to ensure synchronization and load sharing between the inverters. This field of research has been investigated for many years and existing control methods that rely on communication between the inverters achieve good voltage quality. But the need for communication limits the system and leaves the microgrid vulnerable to failures if the communication link is broken.

Communication free alternatives have therefore been developed and the droop control has been the backbone for most of these "wireless" control methods. The droop control works by emulating a synchronous generator. This means that the voltage amplitude is regulated as a function of the output reactive power and the frequency is set to vary as a function of the active power output. This droop behavior enables the parallel-connected inverters to synchronize and share the load according to the set points of the inverters. This also enables the feature of plug-and-play where inverters can be added and removed without necessarily changing the settings of the remaining inverters.

Even though the droop control is reliable and easy to implement, improvements have been searched for both in terms of robustness, expandability and recovering time following disturbances. One of the more recent developments has been a technique where the inverters are controlled using the dynamics of nonlinear oscillators. Coupled oscillators that exist in nature are known to achieve synchronization naturally. For the inverter case, the coupling exists in the electric grid between them and by making the control structure equivalent to a Van der Pol oscillator, the inverters both synchronize and share the load according to the ratings of the inverters.

This thesis will compare the conventional communication free droop control with the newly proposed method called virtual oscillator control (VOC). The comparison will be performed on a realistically simulated microgrid model in MATLAB/Simulink. The microgrid contains two distributed generation sources, both with their own inverter, connected to a common load. The only difference in the simulations when comparing the methods will be how the inverters are controlled.

In order to derive the simulation model, both control methods are first described and tuned according to the chosen size and topology of the microgrid. The two control methods will be tuned to function equivalently in steady state as a way of making the methods comparable. This equivalence is obtained by first selecting the droop parameters before deriving coherent VOC parameters.

In addition to the simulation model, a small-signal state space representation of the microgrid with both inverters is derived for the two control methods. This enables a more thorough comparison by using eigenvalue analysis of the linearized state space models. This way, the characteristics and strengths and weaknesses of the methods will be revealed.

2 Key theoretical elements

In order to be able to follow and understand the derivations and explanations in this thesis, there are a few theoretical elements that need to be known in advance. The functionality of a voltage source inverter and transformations in-between reference frames are essential and therefore presented in their own subsections below. Most of the theoretical background presented here is similar to what the author wrote in a previous work titled "Comparison of peer-to-peer droop control and virtual oscillator control of inverters in a stand-alone microgrid".

2.1 Pulse width modulated voltage source inverter

A voltage source inverter, often called just an inverter, changes its input direct voltage to an alternating voltage at its output. Both the frequency and the magnitude of the alternating voltage output is controlled by the inverter. To enable the inversion, a set of pulse-width modulated switches is turned on and off at a high frequency to shape the output and make it as close to a sinusoidal as possible [12]. The pulse-width modulation (PWM) is made by comparing a sinus wave with a periodic triangle signal as illustrated in fig. 2. When the control signal is higher than the triangle signal, the switch corresponding to that sine wave is turned on and when the control signal is lower than the triangle signal, it is turned off.

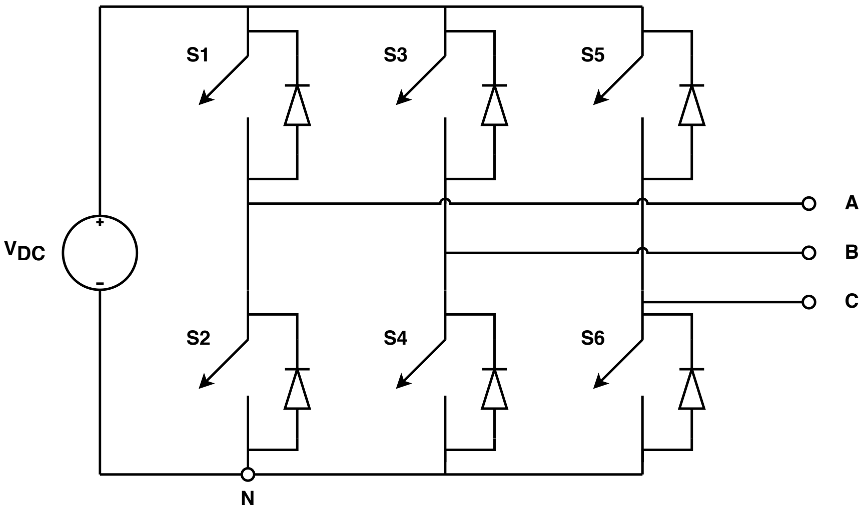

Figure 1: Three-phase voltage source inverter

In a three-phase VSI, a set of six switches is used as shown in fig. 1. Each leg corresponds with one control signal and in this case, the switches S1 and S2 correspond with $V_{control,A}$, S3 and S4 correspond with $V_{control,B}$ and S5 and S6 correspond with $V_{control,C}$.

Only one switch in each leg is conducting at a time. If $V_{control,A} \geq V_{tri}$ then S1 conducts, which makes $V_{AN} = V_{DC}$. And if $V_{control,A} < V_{tri}$, $V_{AN} = 0$ because the switch at the bottom, S2, is on. The same applies to the other legs, but since the control signals are mutually displaced by 120°, the output voltages will also be displaced by 120°. The voltage output will on average contain an equal amount of direct voltage, but this will be canceled out in the line-line voltages. As shown in fig. 2, this method will output a line-line voltage with a fundamental component with the intended frequency and magnitude.

Since the output will contain switching oscillations, it is filtered to produce a result as close to an ideal sinusoid as possible. To filter the output an LCL filter containing two inductors and a shunt capacitor is

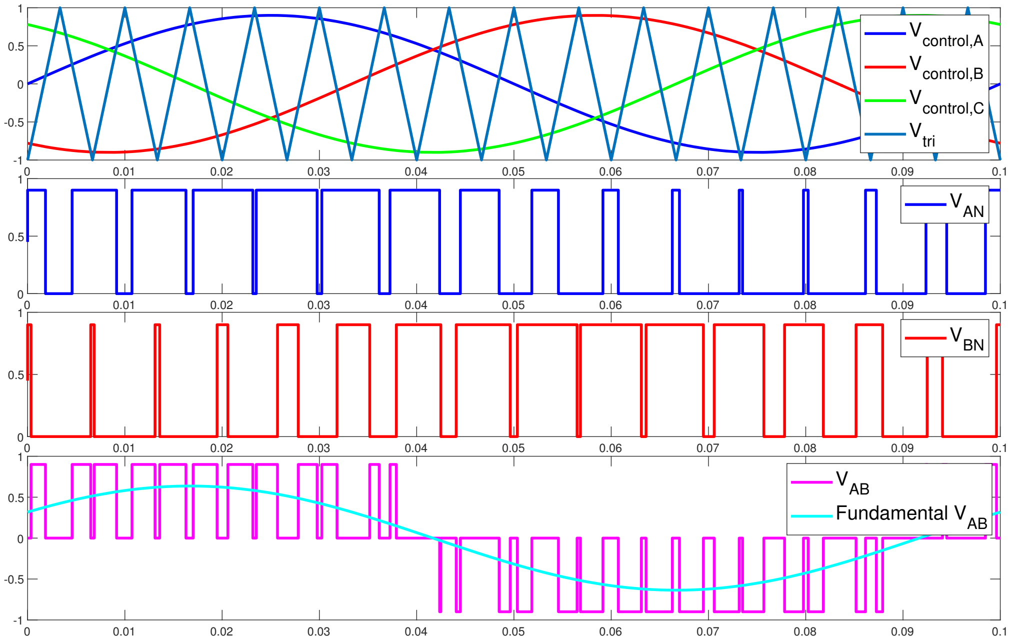

Figure 2: Switching scheme for a voltage source inverter

used. The inductance will smooth out the currents because it rejects rapid current changes while the capacitor removes high-frequency oscillations in the voltage.

2.2 Reference frames and transformations

2.2.1 Clarke Transformation

The $\alpha\beta0$-transformation, which is also known as Clarke transformation, simplifies the treatment of balanced three-phase signals. This is because one can project the balanced signals from 3D to 2D space without losing information about the magnitude and the phase angle. Then one can perform equivalent operations on two signals instead of three which reduces the complexity. The procedure is shown below for the three-phase currents i_a, i_b and i_c.

$$\begin{bmatrix} i_\alpha \\ i_\beta \\ i_0 \end{bmatrix} = \frac{2}{3} \begin{bmatrix} 1 & -\frac{1}{2} & -\frac{1}{2} \\ 0 & \frac{\sqrt{3}}{2} & -\frac{\sqrt{3}}{2} \\ \frac{1}{2} & \frac{1}{2} & \frac{1}{2} \end{bmatrix} \begin{bmatrix} i_a \\ i_b \\ i_c \end{bmatrix} \tag{1}$$

Let $i_a(t) = \hat{I}cos(\omega t - \delta)$ be balanced with $i_b(t)$ and $i_c(t)$. This means they are of same amplitude $\hat{I}$ and mutually displaced by 120°. In this case, when the current lags the reference by δ, the transformation yields

$$\begin{aligned} i_\alpha(t) &= \hat{I}cos(\omega t - \delta) \\ i_\beta(t) &= \hat{I}sin(\omega t - \delta) \\ i_0(t) &= 0 \end{aligned} \tag{2}$$

The transformed currents will now be referred to a stationary two-axis reference frame and the current phasors will rotate with angular velocity ω.

To return to the original reference frame, the inverse transformation is applied.

$$\begin{bmatrix} i_a \\ i_b \\ i_c \end{bmatrix} = \begin{bmatrix} 1 & 0 & 1 \\ -\frac{1}{2} & \frac{\sqrt{3}}{2} & 1 \\ -\frac{1}{2} & -\frac{\sqrt{3}}{2} & 1 \end{bmatrix} \begin{bmatrix} i_\alpha \\ i_\beta \\ i_0 \end{bmatrix} \tag{3}$$

2.2.2 Direct-quadrature-zero Transformation

The $dq0$-transformation is basically a continuation of the Clarke Transform where the difference is a change in the reference frame from stationary into a rotating one. The relation between them is as given in eq. (4).

$$i^{dq} = i^{\alpha\beta} e^{j\omega t} \tag{4}$$

This feature enables three-phase AC signals to be represented as DC components. The simplification is a result of the match between the rotational speed of the dq-reference frame and the frequency of the current. Being able to filter and perform control on DC representative signals make the controlling easier. The amplitude invariant transformation is

$$\begin{bmatrix} i_d \\ i_q \\ i_0 \end{bmatrix} = \frac{2}{3} \begin{bmatrix} cos(\theta) & cos(\theta - \frac{2\pi}{3}) & cos(\theta + \frac{2\pi}{3}) \\ -sin(\theta) & -sin(\theta - \frac{2\pi}{3}) & -sin(\theta + \frac{2\pi}{3}) \\ \frac{1}{2} & \frac{1}{2} & \frac{1}{2} \end{bmatrix} \begin{bmatrix} i_a \\ i_b \\ i_c \end{bmatrix} \tag{5}$$

Assuming still balanced signals and a phase current $i_a(t) = \hat{I}cos(\omega t - \delta)$ lagging the reference by δ yields constant values

$$\begin{aligned} i_d &= \hat{I}cos(\delta) \\ i_q &= 0 \\ i_0 &= 0 \end{aligned} \tag{6}$$

To reverse the transformation, the inverse variant of the $dq0$-transformation is applied.

$$\begin{bmatrix} i_a \\ i_b \\ i_c \end{bmatrix} = \frac{2}{3} \begin{bmatrix} cos(\theta) & -sin(\theta) & 1 \\ cos(\theta - \frac{2\pi}{3}) & -sin(\theta - \frac{2\pi}{3}) & 1 \\ cos(\theta + \frac{2\pi}{3}) & -sin(\theta + \frac{2\pi}{3}) & 1 \end{bmatrix} \begin{bmatrix} i_d \\ i_q \\ i_0 \end{bmatrix} \tag{7}$$

3 Droop control of inverters

Parts of the following theoretical information regarding the functionality of the droop method and tuning of the regulators is an excerpt from the author's project work titled "Comparison of peer-to-peer droop control and virtual oscillator control of inverters in a stand-alone microgrid". Some changes and clarifications are made, but the information presented is mostly the same. First, there is a short introduction to the method of droop control before the inner controllers are presented. Lastly, a tuning of the controllers for the operating conditions used in the simulation model is described.

Droop control for inverters is realized by simulating the droop characteristic of generators in a traditional grid and controlling the output voltage and frequency of the voltage source inverter according to the variation of the output power [9]. There are two main modes of operation, namely master/slave or peer-to-peer [11]. In the first case, a generation unit selected as the master determines the voltage and frequency reference. This reference is transmitted to the other units which are slaves to the reference. In the peer-to-peer mode, all units participate in the regulation of power and together agrees on a voltage and frequency reference. This mode will cause voltage and frequency deviation when the load differs but does not require communication between the inverters as in the master/slave mode. The peer-to-peer mode is chosen in this thesis because of the liberation from a communication link.

The selected version have three controllers which constitutes the droop control method. They are the droop controller, the voltage controller, and the current controller as can be seen in fig. 3. The first part of the chain is the droop controller which gives a reference to the voltage controller based on the measured power output. The voltage controller is a faster unit which enables more precise control of the voltage over the capacitor. The current controller is the fastest controller which provides the final reference voltage for the inverter to follow. This triple control ensures that the voltage reference for the inverter contains inherent characteristics to suppress harmonics caused in the inverter's switching process. This yields a more ideal output voltage than if only the droop controller was implemented.

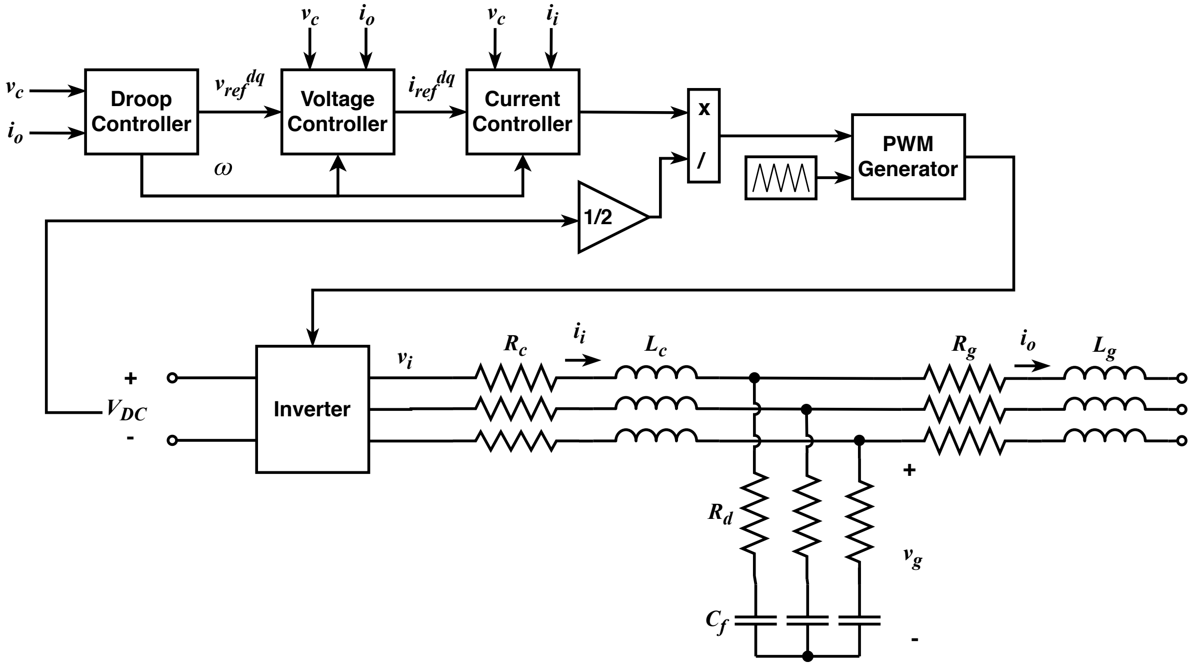

Figure 3: Droop control method of the voltage source inverter

3.1 Droop controller

In order to derive the background for the droop controller, a load flow calculation is performed for a simplified model of the inverter, its line, and its load. Since, when modeling the system as an ideal voltage source delivering power through an impedance as in fig. 4, the current flowing will be according to Ohms law

$$I = \frac{E\angle\delta - V\angle 0^\circ}{Z\angle\theta} \tag{8}$$

The output power will be $S = VI^*$, where I^* is the conjugate of I. Solving for the real and reactive power gives

$$P = \left(\frac{EV}{Z}cos(\delta) - \frac{V^2}{Z}\right)cos(\theta) + \frac{EV}{Z}sin(\delta)sin(\theta) \tag{9}$$

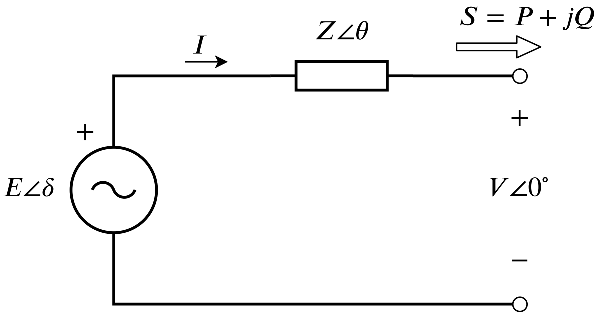

Figure 4: Power flow from a voltage source. The line impedance $Z = R + jX$

$$Q = \left(\frac{EV}{Z}cos(\delta) - \frac{V^2}{Z}\right)sin(\theta) - \frac{EV}{Z}sin(\delta)cos(\theta) \tag{10}$$

For a high voltage system, the R/X ratio in the transmission line is small [13]. Assuming $Z \approx X$, i.e. neglecting R is then a reasonable simplification. This results in $\theta = 90°$ and when assuming δ as small, this gives

$$P = \frac{EV}{X}sin(\delta) \approx \frac{EV}{X}\delta \tag{11}$$

$$Q = \frac{EV}{X}cos(\delta) - \frac{V^2}{X} \approx \frac{EV - V^2}{X} \tag{12}$$

As can be seen from the power equations, the active power, P, depends highly on δ while Q depends on V. This means that regulating the real power gives control over the phase angle and regulating the reactive power gives control over the voltage magnitude. Since the frequency of the grid is proportional to the derivative of the phase angle δ, the frequency can be controlled by measuring the active power output and comparing this with a set point, P^*. The voltage will be a function of the reactive power and can therefore be controlled by comparing the measured Q with a corresponding set point, Q^*.

For the conventional droop control in a high voltage grid, this is obtained by setting a linear variation of the frequency and voltage from given nominal values.

$$\omega = \omega^* - n_p(P - P^*) \tag{13}$$

$$V = V^* - m_q(Q - Q^*) \tag{14}$$

The left side of the equations are the reference values for voltage and frequency which are used by the voltage and current controllers to obtain a final reference voltage for the inverter. The asterisks denote nominal values and set points for the powers.

It should be noted that for the low voltage (0.4 kV) microgrid used in this thesis, the R/X ratio is close to 1 and it is not justifiable to simply neglect the resistance. In fact, for some low voltage transmission lines, the R/X ratio can be much larger than one. In such cases neglecting the line reactance is more correct which results in $\theta = 0°$. The angle, δ is still negligibly small and the derivation will then result in a reversed droop relation. In this reversed case is the active power dependent on the voltage and the reactive power dependent on the frequency. This reversed droop method is also a viable option for controlling the inverters, but will not be used in the simulations in this thesis. This is because the conventional method is the most preferred one.

3.1.1 Setting the droop coefficients

The droop controller coefficients are selected as a means of quantifying the relations between $P-f$ and $Q-V$ presented in eq. (13) and (14). The procedure is to determine a maximum voltage and frequency deviation within the range of the inverter output power. Starting out with the voltage droop coefficient, the maximum and minimum voltage are defined as

$$\begin{aligned} V_{max} &= (1+\Delta_V)V_n \\ V_{min} &= (1-\Delta_V)V_n \end{aligned} \tag{15}$$

Here, V_n is the nominal voltage and the resulting droop coefficient is

$$m_q^* = \frac{2\Delta_V V_{LN}}{Q_{rated}} = 2.31 \times 10^{-3} \tag{16}$$

However, as the inverters will be placed with a distance to the load, there will be a voltage drop over the line leading to a reduced load voltage. In order to increase the load voltage and this way maintain it within the limitations, the droop coefficient is reduced and set as

$$m_q = \frac{\Delta_V V_{max}}{Q_{rated}} = 1.21 \times 10^{-3} \tag{17}$$

Almost the same reasoning is used for the frequency droop coefficient, where the frequency varies between a maximum and a minimum value. However, since the virtual oscillator control was tuned with a resonance frequency of 50 Hz (see section 4), the maximum frequency will be equal to the nominal frequency. This vague explanation will become clear in the description of that controller. The result is that the frequency deviation becomes

$$\begin{aligned} \omega_{max} &= \omega^* \\ \omega_{min} &= (1-\Delta_\omega)\omega^* \end{aligned} \tag{18}$$

Then the droop coefficient becomes

$$n_p = \frac{\Delta_\omega \omega^*}{P_{rated}} = 1.57 \times 10^{-4} \tag{19}$$

The system values used in the calculation of these coefficients are taken from table 1 in the section describing the simulation model.

3.2 Voltage controller

The voltage control regulates the voltage over the capacitor and the damping resistance denoted v_g in fig. 3. The damping resistance is not large compared to the reactance of the filter capacitor at 50 Hz. The voltage drop over the damping resistance is therefore close to negligible. This justifies an approximation where v_g is used as the voltage drop over the capacitor.

To simplify the control structure, regulation is performed in the rotating dq-reference frame. This is obtained by deriving the governing equations in the traditional *abc*-reference frame and subsequently use the transformations in eq. (1) and eq. (4). Applying Kirchhoff's current law on a single phase equivalent of the LCL filter in fig. 3 gives

$$i_i \approx i_o + C_f \frac{dv_g}{dt} \tag{20}$$

In the $\alpha\beta$-frame, the equation remains the same for this single phase equivalent and using the relationship between $\alpha\beta - dq$ in eq. (4) gives for the separate axes

$$C_f \frac{dv_g^d}{dt} - \omega C_f v_g^q = i_i^d - i_o^d \tag{21}$$

$$C_f \frac{dv_g^q}{dt} + \omega C_f v_g^d = i_i^q - i_o^q \tag{22}$$

Transforming into the frequency domain yields

$$v_g^d = \left(i_i^d - i_o^d + \omega C_f v_g^q\right) \frac{1}{sC_f} \tag{23}$$

$$v_g^q = \left(i_i^q - i_o^q - \omega C_f v_g^d\right) \frac{1}{sC_f} \tag{24}$$

In eq. (23) and (24), there is a coupling between the two axes given by the parts $\omega C_f v_g^q$ for the d-voltage and $-\omega C_f v_g^d$ for the q-voltage. Also, the coupling between the voltages and the currents are present. To improve the dynamic response, decoupling measures are taken by removing these components with a feed-forward term in the controller. This enables the voltages to be adjusted by a PI-regulator according to the following open loop transfer function when assuming perfect decoupling.

$$H_{OL,v}(s) = H_{PI,v}(s) H_{sys,v}(s) = \left(K_{pv} + \frac{K_{iv}}{s}\right) \frac{\frac{1}{C_f}}{s} \tag{25}$$

Here K_{pv} and K_{iv} are the proportional and integral gains of the PI voltage regulator.

In this equation, the delay from the current control loop is neglected. After the decoupling, this transfer function is valid for both the d- and the q-voltage and the tuning which is presented in the next section is because of this equal in both cases.

The output of the voltage controller is the current reference for the current controller. To provide the reference current, the relation in eq. (21) and (22) is used along with the PI-regulation of the corresponding voltage.

$$i_{ref}^d = i_o^d + \left(v_{c,ref}^d - v_g^d\right) \left(K_{pv} + \frac{K_{iv}}{s}\right) - v_g^q \omega C_f \tag{26}$$

$$i_{ref}^q = i_o^q + \left(v_{c,ref}^q - v_g^q\right) \left(K_{pv} + \frac{K_{iv}}{s}\right) + v_g^q \omega C_f \tag{27}$$

3.2.1 Tuning of the voltage control

The tuning method used for both voltage and current control is described in [16] as pole placement. It compares a second order characteristic polynomial with the closed loop transfer function of the system that is tuned. The relation between the PI gains and the characteristic polynomial is found and the gain values are chosen to give a suitable response and bandwidth. The tuning presented here is derived from the previous work on this method in [4].

The system that is controlled by the PI-regulator in eq. (25) is

$$H_{sys,v}(s) = \frac{\frac{1}{C_f}}{s} \tag{28}$$

To obtain the gain parameters, the second order characteristic polynomial is used

$$A(s) = s^2 + 2\rho\omega_o s + \omega_o^2 \tag{29}$$

where ρ is the damping ratio of the system and ω_o is the natural frequency.
The closed-loop transfer function for the voltage controller follows from eq. (25)

$$H_{CL,v}(s) = \frac{H_{OL,v}(s)}{1 + H_{OL,v}(s)} = \frac{s\frac{K_{p_v}}{C_f} + \frac{K_{i_v}}{C_f}}{s^2 + s\frac{K_{p_v}}{C_f} + \frac{K_{i_v}}{C_f}} \tag{30}$$

Comparing the denominator in eq. (30) with $A(s)$ in eq. (29) yields

$$\begin{aligned} K_{p_v} &= 2\rho\omega_{o,v}C_f \\ K_{i_v} &= \omega_{o,v}^2 C_f \end{aligned} \tag{31}$$

To get a well-damped system, the damping coefficient is set to $\rho = 1.1$ as outlined in [16]. The natural frequency of the voltage controller should be sufficiently high to give a fast response in the voltage control. It should not be so high that it alters with the faster current control and therefore to ensure sufficient bandwidth between the controllers, it is set a decade lower than the natural frequency for the current controller $\omega_{o,i}$ given in eq. (45).

$$\omega_{o,v} = \frac{\omega_{o,i}}{10} = 300\pi \tag{32}$$

The resulting gain values are then

$$\begin{aligned} K_{p_v} &= 0.0624 \\ K_{i_v} &= 26.737 \end{aligned} \tag{33}$$

To verify that the tuning is stable a bode diagram of the open loop transfer function in eq. (25) is shown in fig. 5. The gain margin is infinite and the phase margin is 78.6°. This is well within the rules of having minimum 6 dB gain margin and 45° phase margin according to [1].

3.3 Current controller

The current control regulates the current out of the inverter, i_i, shown in fig. 3. This control should be faster than the voltage controller to ensure decoupling between the controllers. In the same way as with voltage control, the dq-reference frame is used for easier implementation of the controller. Using Kirchhoff's voltage law on a single phase equivalent of the circuit in fig. 3 gives for the inverter voltage

$$v_i = R_c i_i + L_c\frac{di_i}{dt} + v_g \tag{34}$$

In the $\alpha\beta$ frame, the equation remains the same and using the relationship in eq. (4) gives for the separate axes in the dq-reference frame

$$L_c\frac{di_i^d}{dt} - \omega L_c i_i^q = v_i^d - R_c i_i^d - v_g^d \tag{35}$$

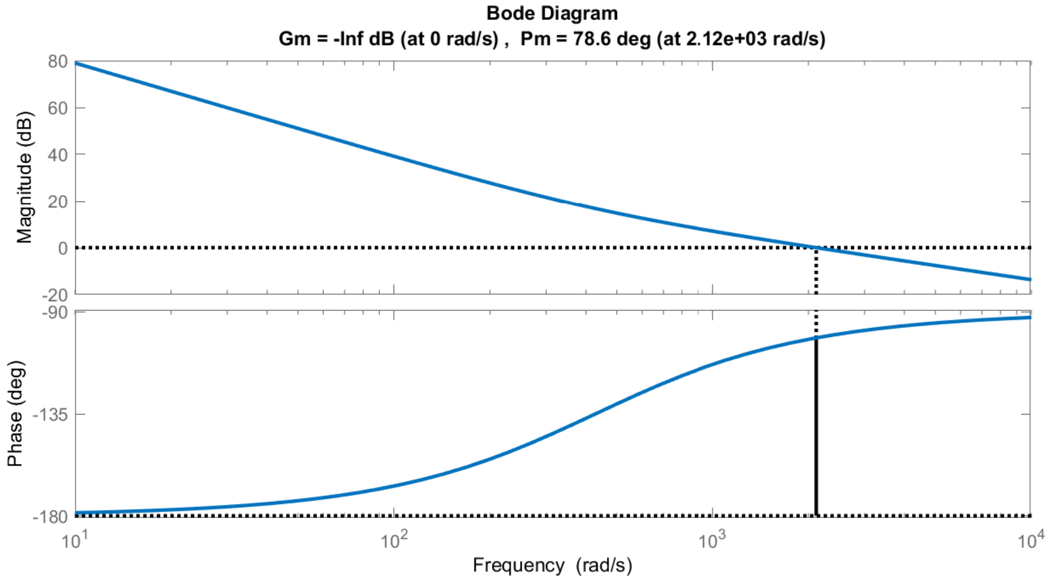

Figure 5: Bode plot for the voltage control

$$L_c \frac{di_i^q}{dt} + \omega L_c i_i^d = v_i^q - R_c i_i^q - v_g^q \tag{36}$$

Transforming into the frequency domain and rearranging yields

$$i_i^d = \left(v_i^d - v_g^d + \omega L_c i_i^q\right) \frac{\frac{1}{L_c}}{s + \frac{R_c}{L_c}} \tag{37}$$

$$i_i^q = \left(v_i^q - v_g^q - \omega L_c i_i^d\right) \frac{\frac{1}{L_c}}{s + \frac{R_c}{L_c}} \tag{38}$$

In eq. (37) and (38), there is a coupling between the two axes given by the parts $\omega L_c i_i^q$ for the d-current and $-\omega L_c i_i^d$ for the q-current. Additionally, there is a coupling between the currents and the voltages. Decoupling measures are therefore utilized by removing these components with a feed-forward term in the controller. This enables the currents to be adjusted by a PI regulator according to the following open loop transfer function

$$H_{OL,c}(s) = H_{PI,c}(s) H_{sys,c}(s) = \left(K_{pc} + \frac{K_{ic}}{s}\right) \frac{\frac{1}{L_c}}{s + \frac{R_c}{L_c}} \tag{39}$$

where K_{pc} and K_{ic} are the proportional and integral gains of the PI current regulator.

In this equation, the computational delay following the voltage source inverter is neglected. After the decoupling, this transfer function is valid for both the d- and the q-current and the tuning is therefore equal in both cases.

The output of the current controller is the voltage reference for the inverter. To provide the reference voltage, the relation in eq. (35) and (36) is used along with the PI regulation of the corresponding current.

$$v_{ref}^d = v_c^d + \left(i_{ref}^d - i_i^d\right)\left(K_{pc} + \frac{K_{ic}}{s}\right) - \omega L_c i_i^q \tag{40}$$

$$v_{ref}^{q} = v_{g}^{q} + \left(i_{ref}^{q} - i_{i}^{q}\right)\left(K_{pc} + \frac{K_{ic}}{s}\right) + \omega L_c i_i^d \tag{41}$$

Combining these references and assuming balanced conditions, i.e. ($v_{ref}^{0} = 0$), gives through the inverse Clarke transform the reference in abc-coordinates, v_{ref}. This reference is used by a PWM generator to create on/off signals to the inverter switches.

3.3.1 Tuning of the current control

The system that is controlled by the PI-regulator in eq. (39) is

$$H_{sys,c}(s) = \frac{\frac{1}{L_c}}{s + \frac{R_c}{L_c}} \tag{42}$$

The closed-loop transfer function for the current controller follows from eq. (39)

$$H_{CL,c}(s) = \frac{H_{OL,c}(s)}{1 + H_{OL,c}(s)} = \frac{\frac{K_{pc}}{L_c}s + \frac{K_{ic}}{L_c}}{s^2 + s\left(\frac{K_{pc}}{L_c} + \frac{R_c}{L_c}\right) + \frac{K_{ic}}{L_c}} \tag{43}$$

Comparing the denominator in eq. (43) and the characteristic equation in eq. (29) yields

$$\begin{aligned} K_{pc} &= 2\rho\omega_{o,i}L_c - R_c \\ K_{ic} &= \omega_{o,i}^2 L_c \end{aligned} \tag{44}$$

The natural frequency of the current controller should be high, giving a fast response in the current control. However, it should not exceed the switching frequency as this would result in regulation faster than the system can handle. To ensure sufficient bandwidth between the switching dynamics and the current control, the natural frequency is set a decade lower than the switching frequency. Since the switching frequency, $f_{sw} = 15$ kHz, this gives

$$\omega_{o,i} = \frac{2\pi 15000}{10} = 3000\pi \tag{45}$$

The resulting gain values are then

$$\begin{aligned} K_{pc} &= 10.537 \\ K_{ic} &= 45.142 \times 10^3 \end{aligned} \tag{46}$$

To verify that the tuning is stable, a bode diagram of the open loop transfer function in eq. (39) is shown in fig. 6. The gain margin is infinite and the phase margin is 78.6°. Notice that the crossover frequency is, as desired, 10 times higher for the current control than the voltage control. As previously presented, the margins state that this is a stable solution.

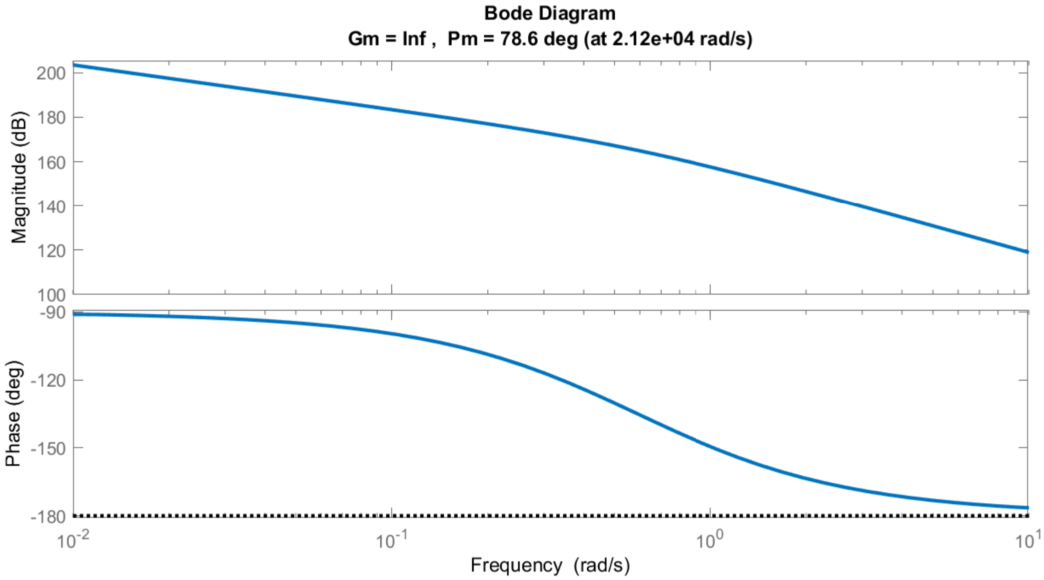

Figure 6: Bode plot for the current control

4 Virtual oscillator dynamics

Synchronization is an intriguing concept which has piqued the interest of researchers in various fields for a long time. The first concept of synchronization was described by Christiaan Huygens in the 17th century [2]. He discovered mutual synchronization between two pendulum clocks hanging on the same beam. The swing of the pendulums synchronized due to their coupling through the beam. The non-stiff beam allowed mechanical vibrations from one pendulum swing affect the other clock's swing and vice versa. This resulted in a synchronous state which the clocks returned to when imposed by perturbations. Similar phenomena can be found in other places in nature as well. For instance, the synchronization of an audience clapping or fireflies in Malaysia that flash in unison. This tendency towards synchronization is actually one of the most far-reaching drives in nature according to the mathematician Steven Strogatz [21].

There are several mathematical models of oscillators. Some of them can be used to describe the coupling effect where the oscillators synchronize their dynamics as seen in nature. The Van der Pol oscillator [8], is such a model and is used as the base of the virtual oscillator controller because it can produce stable limit-cycle oscillations. The equation for the Van der Pol oscillator in this thesis is

$$\ddot{v_C} - \epsilon\sigma\left(1 - 2v_C^2\right)\dot{v_C} + v_C = -\epsilon K_i \dot{i} \tag{47}$$

The Van der Pol oscillator has non-linear damping that is negative when v_C is small and positive when v_C is large. This way the oscillations are restricted within an area around the fixed point and the limit-cycle is obtained. This means it will approach a periodic steady state. Further, by selecting suitable model parameters, the oscillations can obtain near-sinusoidal behavior with a close to fixed period and amplitude. These oscillations can be used as a voltage reference for the PWM generator which results in the inverter being controlled as a virtual oscillator. This facilitates spontaneous synchronization between parallel inverters using this control technique.

The Van der Pol oscillator is realized by using a current source depending on the cube of the voltage as an input to an RLC parallel circuit. This circuit represents a narrow band-pass filter where the resonance frequency is amplified. The point of operation can freely be varied and the setting will make the oscillator voltage oscillate at this frequency. A natural choice is the grid frequency which can be obtained by choosing the relation between the inductor and the capacitor as

$$L = \frac{1}{(2\pi \cdot 50)^2 C} \tag{48}$$

where 50 Hz is the nominal grid frequency.

The amplitude of the voltage oscillations is regulated by measuring the current out of the inverter. The current in the oscillator, $i = K_i i_i$, introduces a forcing element in the oscillator which takes into account the loading of the inverter. This proportional regulation keeps the voltage output within its selected requirements but is not able to make the voltage output have a specific value.

The dynamics are described in depth in the following subsections where also the coherency between the droop controller and the virtual oscillator controller is presented.

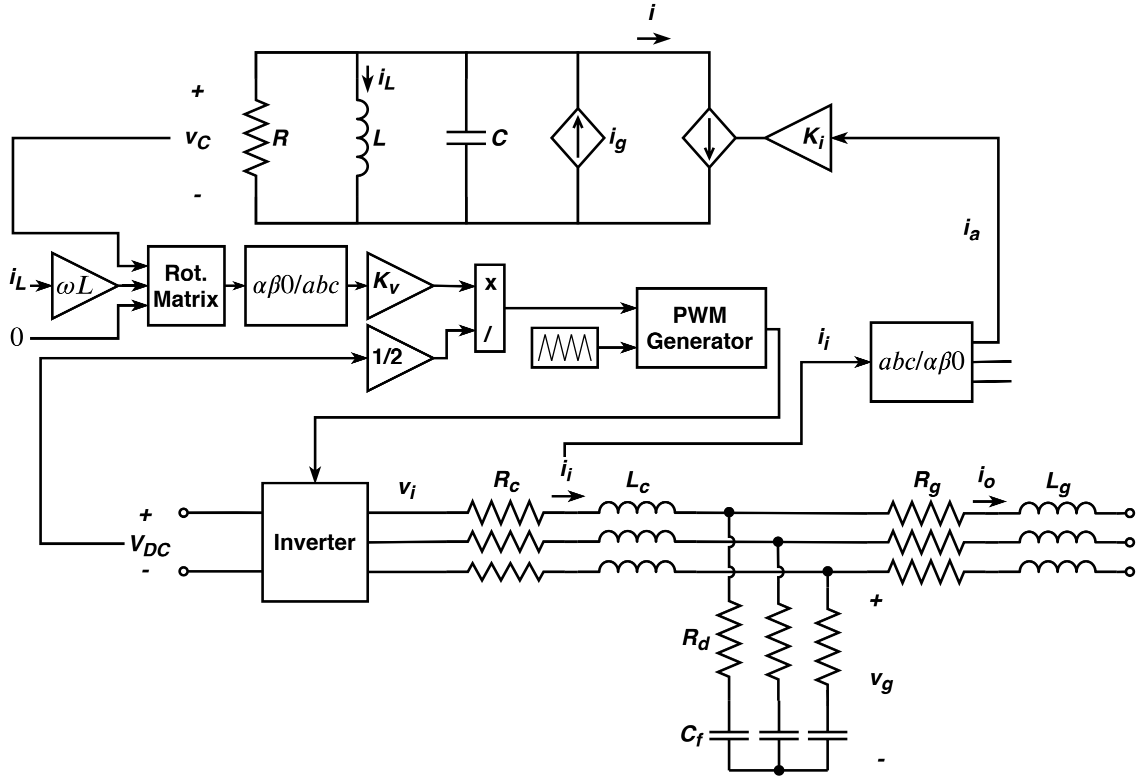

Figure 7: Virtual oscillator control method of the voltage source inverter

4.1 Deriving the dynamic equations for the virtual oscillator

The dynamic equations for the magnitude of the inverter terminal voltage and the phase angle will be derived in this section. The result will be a system of differential equations describing the characteristics of the virtual oscillator. During the derivation, polar coordinates, well-known differential rules and some integration will be applied. The derivation will switch between different times frames and might seem a bit complicated. If the reader wishes to skip the derivation and trust that the relations in eq. (70) are valid, feel free to jump to section 4.3.

The derivation is made by following the procedure presented by Brian Johnson et al. in [6], [19] and [20]. In order to make the derivation more understandable, parts of the procedure are described more clearly in this thesis.

The starting point of describing the virtual oscillator dynamics is to apply Kirchhoff's voltage- and current law on the RLC-parallel in fig. 7.

$$\frac{di_L}{dt} = \frac{v_C}{L} \tag{49}$$

$$\frac{dv_C}{dt} = \frac{1}{C}\left(-\frac{v_C}{R} - i_L + i_g - K_i i\right) = \frac{1}{C}\left(\sigma v_C - i_L - \alpha v_c^3 - K_i i\right) \tag{50}$$

where $i_g = -\alpha v_C^3$ is a voltage-dependent current source and $R = -\frac{1}{\sigma}$ is the resistance.

For subsequent analysis, some useful designations are defined as

$$\begin{aligned} \epsilon &= \sqrt{\frac{L}{C}} \\ \omega^* &= \frac{1}{\sqrt{LC}} \\ \tau &= \frac{t}{\sqrt{LC}} = \omega^* t \end{aligned} \tag{51}$$

This yields in the equivalent time frame of τ

$$\frac{di_L}{d\tau} = \sqrt{LC}\frac{di_L}{dt} = \frac{v_C}{\epsilon} \tag{52}$$

$$\frac{dv_C}{d\tau} = \sqrt{LC}\frac{dv_C}{dt} = \epsilon\left(\sigma v_C - \alpha v_C^3 - i_L - K_i i\right) \tag{53}$$

By choosing scaled versions of the inductor current and the capacitor voltage as states enable further simplification.

$$\begin{aligned} x &\equiv K_v \epsilon i_L \\ y &\equiv K_v v_C \end{aligned} \tag{54}$$

Since, when differentiating these states

$$\begin{aligned} \dot{x} &= \frac{dx}{d\tau} = y \\ \dot{y} &= \frac{dy}{d\tau} = \epsilon\left(\sigma y - \frac{\alpha y^3}{K_v^2} - K_i K_v i\right) - x \end{aligned} \tag{55}$$

The scaled oscillator voltage is parameterized with time-varying amplitude and phase as

$$K_v v_C = \sqrt{2}V(t)cos(\omega t + \theta(t)) \tag{56}$$

where ω is the electrical frequency of the terminal voltage and θ is the phase offset. This can be more compactly formulated with the instantaneous phase angle $\phi(t) = \omega t + \theta(t)$. Since the frequency of the terminal voltage might deviate slightly from the nominal frequency ω^*, the voltage can also be expressed with the offset from the nominal frequency as $\omega^* t + \theta^*(t) = \phi$ where θ^* is the phase offset with respect to $\omega^* t$.

To extract information about the phase and magnitude, the equations are transformed into polar coordinates. Since x and y are orthogonal and sinusoidal, they relate with the magnitude and phase as

$$\begin{aligned} \sqrt{2}V &= \sqrt{x^2+y^2} \\ \phi &= tan^{-1}\left(\frac{x}{y}\right) \end{aligned} \tag{57}$$

Differentiating with respect to τ and inserting for x and y yields the dynamical model for the RMS voltage amplitude V and the instantaneous angle ϕ as in eq. (58).

$$\begin{aligned} \dot{V} &= \epsilon\left(\sigma V cos(\phi) - \frac{2\alpha}{K_v^2}V^3 cos^3(\phi) - \frac{K_i K_v i}{\sqrt{2}}\right) cos(\phi) \\ \dot{\phi} &= 1 - \frac{\epsilon}{V}\left(\sigma V cos(\phi) - \frac{2\alpha}{K_v^2}V^3 cos^3(\phi) - \frac{K_i K_v i}{\sqrt{2}}\right) sin(\phi) \end{aligned} \tag{58}$$

The derivation of eq. (58) are explained below starting with the RMS voltage amplitude and applying the chain rule of differentiation.

$$\dot{V} = \frac{1}{\sqrt{2}}\frac{d(\sqrt{2}V)}{d\tau} = \frac{1}{\sqrt{2}}\frac{1}{2}\left(x^2+y^2\right)^{-1/2} \cdot \frac{d}{d\tau}\left(x^2+y^2\right) = \frac{1}{4V} \cdot (2x\dot{x} + 2y\dot{y}) \tag{59}$$

Inserting for x and y gives

$$\dot{V} = \frac{1}{2V}\left(2V^2 sin(\phi)cos(\phi) + \sqrt{2}V cos(\phi)\left(-\sqrt{2}V sin(\phi) - \frac{2\sqrt{2}\epsilon\alpha}{K_v^2}V^3 cos^3(\phi) + \sqrt{2}\epsilon\sigma V cos(\phi) - \epsilon K_i K_v i\right)\right) \tag{60}$$

Simplifying this equation results in the formulation presented in eq. (58).

Next, differentiating the instantaneous phase angle with respect to τ gives

$$\dot{\phi} = \frac{d}{d\tau}\left(\tan^{-1}\left(\frac{x}{y}\right)\right) \tag{61}$$

The chain rule gives

$$\dot{\phi} = \frac{1}{1+\left(\frac{x}{y}\right)^2} \cdot \frac{d}{d\tau}\left(\frac{x}{y}\right) \tag{62}$$

Using the quotient rule yields

$$\dot{\phi} = \frac{1}{1+\left(\frac{x}{y}\right)^2} \cdot \frac{\dot{x}y - x\dot{y}}{y^2} = \frac{1}{2V^2} \cdot (\dot{x}y - x\dot{y}) \tag{63}$$

Inserting for x and y in polar coordinates

$$\dot{\phi} = \frac{1}{2V^2}\left(2V^2 cos^2(\phi) - \sqrt{2}V sin(\phi)\left(-\sqrt{2}V sin(\phi) + \sqrt{2}\epsilon\left(\sigma V cos(\phi) - \frac{2\alpha}{K_v^2}V^3 cos^3(\phi)\right) - \epsilon K_i K_v i\right)\right) \tag{64}$$

Simplifying this equation gives the same formulation as previously presented in eq. (58).

The final dynamical model written in the original time coordinates and the nominal frequency of oscillations are derived by evaluating $\frac{dV}{dt} = \omega^*\dot{V}$ and $\frac{d\phi}{dt} = \omega^*\dot{\phi}$ as well as applying the relation $\frac{d\phi}{dt} = \omega^* + \frac{d\theta^*}{dt}$ on the phase dynamics. The resulting oscillator dynamics are

$$\begin{aligned}\frac{dV}{dt} &= \frac{1}{C}\left(\sigma V cos(\omega^* t+\theta^*) - \frac{2\alpha}{K_v^2}V^3 cos^3(\omega^* t+\theta^*) - \frac{K_iK_v i}{\sqrt{2}}\right) cos(\omega^* t+\theta^*)\\ \frac{d\theta^*}{dt} &= -\frac{1}{CV}\left(\sigma V cos(\omega^* t+\theta^*) - \frac{2\alpha}{K_v^2}V^3 cos^3(\omega^* t+\theta^*) - \frac{K_iK_v i}{\sqrt{2}}\right) sin(\omega^* t+\theta^*)\end{aligned} \tag{65}$$

4.2 Averaging the virtual oscillator dynamics

The non-linear behavior in eq. (65), is difficult to work with. A common approach in non-linear theory is to obtain an approximation of the system. One technique, the periodic averaging method, approximates the solution of this system by the solution of an "average system", obtained by averaging $f(t,x,\epsilon)$ at $\epsilon = 0$ [10]. This gives qualitative knowledge of the behavior without solving the system explicitly. The method is to integrate the system f over a cycle, since for a small value of ϵ, an autonomous average system

$$\dot{x} = \epsilon f_{av}(x) = \frac{\epsilon}{T}\int_0^T f(\tau,x,\epsilon)d\tau \tag{66}$$

is associated with the system

$$\dot{x} = \epsilon f(t,x,\epsilon) \tag{67}$$

The autonomous system approximates the behavior of the non-autonomous system with an error $\mathcal{O}(\epsilon)$ on time intervals of order $\mathcal{O}(1/\epsilon)$ [10]. This simply means that the approximation becomes more valid when reducing ϵ. This is well suited for the control dynamics of the virtual oscillator since a target for the controller is to reduce ϵ. The reason is that this will, in turn, give a more ideal reference voltage for the inverter to follow. More details of this will be given in later sections.

The virtual oscillator control dynamics consist of fast oscillations (3rd harmonic) coming from the term $cos^3(\phi)$ in addition to the fundamental frequency components. As a means of ironing out the fast oscillations, periodic averaging is applied to the dynamics in eq. (58). In the quasi-harmonic limit $\epsilon \to 0^+$, the dynamics are approximated by averaging the trajectory over one cycle. In the time frame of τ, a cycle is equal to 2π. Let $\overline{V}$ and $\overline{\theta}^*$ denote the average value of V and θ^* which gives

$$\begin{aligned}\dot{\overline{V}} &= \frac{\epsilon}{2\pi}\int_0^{2\pi}\left(\sigma\overline{V}cos(\tau+\overline{\theta}^*) - \frac{2\alpha}{K_v^2}\overline{V}^3 cos^3(\tau+\overline{\theta}^*) - \frac{K_iK_v}{\sqrt{2}}i\right) cos(\tau+\overline{\theta}^*)d\tau\\ \dot{\overline{\theta}}^* &= -\frac{\epsilon}{2\pi\overline{V}}\int_0^{2\pi}\left(\sigma\overline{V}cos(\tau+\overline{\theta}^*) - \frac{2\alpha}{K_v^2}\overline{V}^3 cos^3(\tau+\overline{\theta}^*) - \frac{K_iK_v}{\sqrt{2}}i(\tau)\right) sin(\tau+\overline{\theta}^*)d\tau\end{aligned} \tag{68}$$

Evaluating the first terms in the integral gives

$$\begin{aligned}\dot{\overline{V}} &= \frac{\epsilon}{2\pi}\left(\sigma\overline{V}\pi - \frac{2\alpha}{K_v^2}\overline{V}^3\frac{3\pi}{4} - \int_0^{2\pi}\frac{K_iK_v}{\sqrt{2}}i(\tau)cos(\tau+\overline{\theta}^*)d\tau\right)\\ \dot{\overline{\theta}}^* &= -\frac{\epsilon}{2\pi\overline{V}}\left(0 - 0 - \frac{K_iK_v}{\sqrt{2}}\int_0^{2\pi} i(\tau)sin(\tau+\overline{\theta}^*)d\tau\right)\end{aligned} \tag{69}$$

Notice that the first terms in $\dot{\overline{\theta}}^*$ average to zero which simplifies to

$$\begin{aligned}\dot{\overline{V}} &= \epsilon\left(\frac{\sigma\overline{V}}{2} - \frac{3\alpha}{4K_v^2}\overline{V}^3\right) - \frac{K_iK_v\epsilon}{2\pi\sqrt{2}}\int_0^{2\pi} i(\tau)cos(\tau+\overline{\theta}^*)d\tau\\ \dot{\overline{\theta}}^* &= \frac{K_iK_v\epsilon}{2\pi\sqrt{2}\overline{V}}\int_0^{2\pi} i(\tau)sin(\tau+\overline{\theta}^*)d\tau\end{aligned} \tag{70}$$

4.3 Uncovering droop similarities

The relation in eq. (70) is close to resembling the average power from the inverter. In this section, the power is derived in those relations and a rotational matrix which enables selection between conventional and reversed droop is introduced. Both possibilities are described even though only the conventional one is used in the simulations. This is to illustrate that the virtual oscillator control is able to emulate both methods. The rotational matrix at the oscillator output in fig. 7, is utilized to define a set of orthogonal signals, $v^{\alpha}(t)$ and $v^{\beta}(t)$ which will make up the reference voltage in the $\alpha\beta$ coordinate system. The rotational matrix gives the value of these voltages as

$$\begin{bmatrix} v^{\alpha}(t) \\ v^{\beta}(t) \end{bmatrix} = \begin{bmatrix} cos(\Phi) & sin(\Phi) \\ -sin(\Phi) & cos(\Phi) \end{bmatrix} \begin{bmatrix} y \\ x \end{bmatrix} \tag{71}$$

where x and y are the states from eq. (54) and Φ is an angle chosen as either 0° or 90°.

The instantaneous active and reactive power out of the inverter is for a single phase

$$\begin{aligned} p(t) &\equiv v(t)i(t) = v^{\alpha}(t)i(t) \\ q(t) &\equiv v(t-\frac{\pi}{2})i(t) = v^{\beta}(t)i(t) \end{aligned} \tag{72}$$

Assuming that the fundamental frequency of the current $i(t)$ is also ω^*, the average real and reactive power is

$$\begin{aligned} \overline{p} &= \frac{\omega^*}{2\pi}\int_0^{\frac{2\pi}{\omega^*}} p(t)dt \\ \overline{q} &= \frac{\omega^*}{2\pi}\int_0^{\frac{2\pi}{\omega^*}} q(t)dt \end{aligned} \tag{73}$$

For a balanced system, the three-phase power is three times the per phase power i.e

$$\begin{aligned} \overline{P} &= 3\overline{p} \\ \overline{Q} &= 3\overline{q} \end{aligned} \tag{74}$$

These power equations are almost present in the VOC dynamics. By multiplying and dividing by $\sqrt{2}\overline{V}$ in the integrals of eq. (70) gives after referring back to the original time frame of t

$$\begin{aligned} \frac{d}{dt}\overline{V} &= \epsilon\omega\left(\frac{\sigma\overline{V}}{2} - \frac{3\alpha}{4K_v^2}\overline{V}^3\right) - \frac{K_iK_v\epsilon(\omega^*)^2}{2\pi\sqrt{2}}\int_0^{\frac{2\pi}{\omega^*}} \frac{\sqrt{2}\overline{V}}{\sqrt{2}\overline{V}} i(t)cos(\omega^* t + \overline{\theta}^*)dt \\ \frac{d}{dt}\overline{\theta}^* &= \frac{K_iK_v\epsilon(\omega^*)^2}{2\pi\sqrt{2}\overline{V}}\int_0^{\frac{2\pi}{\omega^*}} \frac{\sqrt{2}\overline{V}}{\sqrt{2}\overline{V}} i(t)sin(\omega^* t + \overline{\theta}^*)dt \end{aligned} \tag{75}$$

Neglecting $\mathcal{O}(\epsilon^2)$ terms that occur when inserting for $\overline{V}$ and $\overline{\theta}$ in the integral [20] and then integrating by parts yields as in [19],

$$\begin{aligned} \frac{d}{dt}\overline{V} &\approx \frac{1}{C}\left(\frac{\sigma\overline{V}}{2} - \frac{3\alpha}{4K_v^2}\overline{V}^3\right) - \frac{K_iK_v}{6C\overline{V}}\left(cos(\Phi)\overline{P} + sin(\Phi)\overline{Q}\right) \\ \frac{d}{dt}\overline{\theta}^* &\approx \frac{K_iK_v}{6C\overline{V}^2}\left(-sin(\Phi)\overline{P} + cos(\Phi)\overline{Q}\right) \end{aligned} \tag{76}$$

Depending on the value of Φ, the VOC will either subsume conventional or reversed droop behavior. (The difference is previously explained in section 3). The reversed droop is obtained by setting $\Phi = 0°$ and the conventional by having $\Phi = 90°$.

4.4 Deriving the embedded droop laws

In steady-state, the virtual oscillator control behaves similarly to the droop control in the sense of trading voltage and frequency for either active or reactive power. This claim is supported by the derivation in the following subsection.

At steady-state, the voltage will be in equilibrium $\overline{V} = \overline{V}_{eq}$. From this point, and throughout this section, all variables in equilibrium will be denoted $(\cdot)_{eq}$. To extract the steady-state magnitude dynamics one utilizes that in steady-state

$$\frac{d\overline{V}}{dt} = 0 \tag{77}$$

Combining this with eq. (76) gives

$$0 = \frac{1}{2C}\left(\sigma\overline{V}_{eq} - \frac{3\alpha}{2K_v^2}\overline{V}_{eq}^3\right) - \frac{K_iK_v}{6C\overline{V}_{eq}}\left(cos(\Phi)\overline{P}_{eq} + sin(\Phi)\overline{Q}_{eq}\right) \tag{78}$$

which is equivalent to

$$\frac{3\alpha}{2K_v^2}\overline{V}_{eq}^4 - \sigma\overline{V}_{eq}^2 + \frac{K_iK_v}{3}\left(cos(\Phi)\overline{P}_{eq} + sin(\Phi)\overline{Q}_{eq}\right) = 0 \tag{79}$$

This is a suitable description of the voltage as a function of either the active or reactive power. A solution for the voltage will be derived in section 4.5

For the phase angle and phase dynamics at the inverter terminal, one must remember that $\theta(t) + \omega t = \theta^*(t) + \omega^* t$. This equality is also valid if both sides are differentiated with respect to time.

$$\frac{d\theta}{dt} + \omega = \frac{d\theta^*}{dt} + \omega^* \tag{80}$$

Combining this with the fact that $d\theta/dt = 0$ at steady state and assuming $\overline{\theta}^* \approx \theta^*$ gives

$$\frac{d\overline{\theta}^*}{dt} \approx \frac{d\theta^*}{dt} = 0 + \omega_{eq} - \omega^* \tag{81}$$

Inserting for the phase dynamics in eq. (76) gives

$$\omega_{eq} \approx \omega^* + \frac{K_iK_v}{6C\overline{V}_{eq}^2}\left(-sin(\Phi)\overline{P}_{eq} + cos(\Phi)\overline{Q}_{eq}\right) \tag{82}$$

4.4.1 Deriving the droop coefficients

Since the voltage and frequency were found to be dependent on the power output, the link between the droop coefficients in a droop controller and the VOC parameters is established in this section.

Conventional droop behavior is characterized by

$$\omega_{eq} = \omega^* - n_p\overline{P}_{eq} \text{ and } \overline{V}_{eq} = \overline{V}_{max} - m_q\overline{Q}_{eq} \tag{83}$$

while reversed droop is characterized by

$$\omega_{eq} = \omega^* + n_q\overline{Q}_{eq} \text{ and } \overline{V}_{eq} = \overline{V}_{max} - m_p\overline{P}_{eq} \tag{84}$$

where $\overline{V}_{max}$ is the maximum RMS phase voltage and the power set points are zero. The droop coefficients are denoted m for voltage and n for frequency with subscripts following the type of power that is associated.

From these equations, it can be understood that the droop coefficients are the first-order derivative of $\overline{V}_{eq}$ and/or ω_{eq} as a function of $\overline{P}_{eq}$ and/or $\overline{Q}_{eq}$ around the working point $\overline{V}_{max}$.

Starting with the conventional droop where $\Phi = \pi/2$ yields

$$\begin{aligned} m_q &= -\frac{d\overline{V}_{eq}}{d\overline{Q}_{eq}}\Big|_{\overline{V}_{eq}=\overline{V}_{max}} \\ n_p &= -\frac{d\overline{\omega}_{eq}}{d\overline{P}_{eq}}\Big|_{\overline{V}_{eq}=\overline{V}_{max}} \end{aligned} \tag{85}$$

From eq. (82) it can be seen that when $\overline{V}_{eq} = \overline{V}_{max}$

$$n_p = \frac{K_i K_v}{6C\overline{V}_{max}^2} \tag{86}$$

For the voltage vs. reactive power droop coefficient, m_q, it is a bit more complicated. But implicit differentiation of eq. (79) with respect to $\overline{Q}_{eq}$ gives

$$\frac{3\alpha}{2K_v^2} 4\overline{V}_{eq}^3 \frac{d\overline{V}_{eq}}{d\overline{Q}_{eq}} - 2\sigma\overline{V}_{eq}\frac{d\overline{V}_{eq}}{d\overline{Q}_{eq}} + \frac{K_i K_v}{3} = 0 \tag{87}$$

Solving this for $d\overline{V}_{eq}/d\overline{Q}_{eq}$ at the working point gives

$$m_q = \frac{K_i K_v}{3}\left(\frac{6\alpha}{K_v^2}\overline{V}_{max}^3 - 2\sigma\overline{V}_{max}\right)^{-1} \tag{88}$$

For the reversed droop, where $\Phi = 0$, the coefficients are given as

$$\begin{aligned} m_p &= -\frac{d\overline{V}_{eq}}{d\overline{P}_{eq}}\Big|_{\overline{V}_{eq}=\overline{V}_{max}} \\ n_q &= \frac{d\omega_{eq}}{d\overline{Q}_{eq}}\Big|_{\overline{V}_{eq}=\overline{V}_{max}} \end{aligned} \tag{89}$$

The same derivation as for the conventional droop now returns

$$\begin{aligned} m_p &= \frac{K_i K_v}{3}\left(\frac{6\alpha}{K_v^2}\overline{V}_{max}^3 - 2\sigma\overline{V}_{max}\right)^{-1} \\ n_q &= \frac{K_v K_i}{6C\overline{V}_{max}^2} \end{aligned} \tag{90}$$

These equations relating the VOC parameters to the droop coefficients are in the next section solved in order to have the VOC and the droop behave similarly in steady state.

4.5 Deriving coherent variables between droop control and virtual oscillator control

In this section, the VOC parameters are selected in order to be coherent with the droop coefficients m and n. This ensures that the virtual oscillator control and the droop control are equivalent in steady state. This is desired to be able to compare the models on equal terms. Before solving for the VOC parameters from the droop relation derived in the previous section, the voltage and current gains are chosen. The voltage gain is selected such that a 1 V RMS voltage in the oscillator corresponds with the maximum voltage at the terminal. Secondly, the current gain is picked so that the scaled current out of the oscillator is 1 A RMS when rated three-phase power is delivered. If the conventional droop is desired, the gain is associated with the reactive power and if the reversed droop is desired, the gain is associated with the active power. These relations are ensured if

$$\begin{aligned} K_v &= \overline{V}_{max} \\ K_i &= \frac{3\overline{V}_{min}}{cos(\Phi)\overline{P}_{eq} + sin(\Phi)\overline{Q}_{eq}} \end{aligned} \tag{91}$$

Next, the relation between α and σ is investigated. Using eq. (79) for the reversed droop as a basis and deriving the roots of this equation yield a relation between $\overline{V}_{max}, K_v, \alpha$, and σ. The same derivation could have been done with the conventional droop which would give the same outcome.

Knowing that the equilibrium voltage is positive, the two positive roots of eq. (79) are (notice the ±)

$$\overline{V}_{eq} = K_v \left(\frac{\sigma \pm \sqrt{\sigma^2 - 2\alpha \frac{K_i}{K_v} \overline{P}_{eq}}}{3\alpha} \right)^{\frac{1}{2}} \tag{92}$$

The equilibrium voltage will be real if both

$$\sigma^2 - 2\alpha \frac{K_i}{K_v} \overline{P}_{eq} > 0 \tag{93}$$

and

$$\sigma - \sqrt{\sigma^2 - 2\alpha \frac{K_i}{K_v} \overline{P}_{eq}} > 0 \tag{94}$$

are fulfilled. This is obtained if

$$0 < \overline{P}_{eq} > \frac{\sigma^2 K_v}{2\alpha K_i} \tag{95}$$

Equation (92) imply that when $\overline{P}_{eq} = 0$, meaning it is no-load or an open circuit on the inverter terminals, the voltage magnitude will be the highest

$$\overline{V}_{max} = K_v \sqrt{\frac{2\sigma}{3\alpha}} \tag{96}$$

Since $K_v = \overline{V}_{max}$, it is found that

$$\alpha = \frac{2\sigma}{3} \tag{97}$$

By knowing K_v, K_i and α there are only two unknowns left in eq. (89) and (90). These two equations can then be solved for C and σ. Solving first for C gives

$$C = \frac{K_i}{6K_v} \frac{1}{n} \tag{98}$$

where n could be either n_q or n_p. Solving for σ gives

$$\sigma = \frac{K_i}{6} \frac{1}{m} \tag{99}$$

where m could be either m_q or m_p.

5 Description of the simulation model

The setup of the simulation model is schematically shown in fig. 8. The level of details of the model is set to focus on a realistic version with a time frame ranging from milliseconds and up to a few seconds. The source of power in the grid are two direct voltage sources that each represent PV panels and associated energy storage systems. Such power sources will typically have a larger time constant than the focus in this thesis. These sources are therefore modeled as constant voltage sources. Since the voltage amplitude of the generation unit in a real situation will vary according to the weather conditions etc., a DC/DC boost converter is needed to transform the voltage into the required input level for the inverter. The boosted voltage will vary as the DC side capacitor is charged and discharged when power is drawn by the load. These voltage oscillations are, for this setup, well within the selected time frame and this behaviour is therefore implemented in the model.

The main focus, in this thesis, is the inverter control. The controllers give a voltage reference to a pulse width generator which controls the inverter switches. These switches are assumed ideal and set to turn on/off at a frequency of 15 kHz. The voltage output is a direct result of this switching process and needs to be filtered to obtain a nice sinusoidal shape. The LCL filter at the output is therefore included as it smooths the voltage and current before the transmission line brings the power to the load. The line out of the two inverters are of the same type but vary in length. The load is common for both inverters and is assumed resistive and inductive. Depending on the load demand, either one or two inverters are in operation.

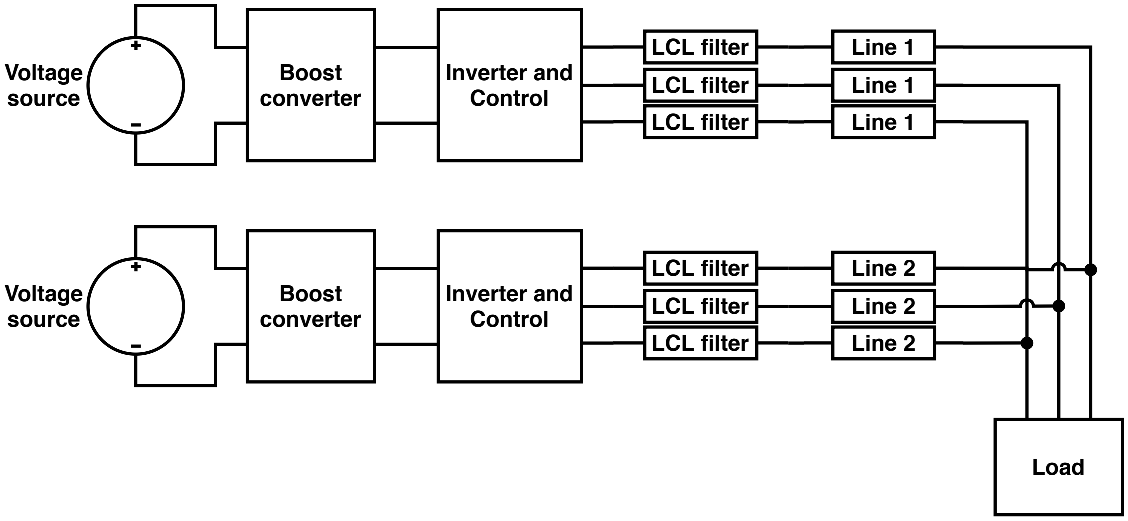

Figure 8: Topology of the simulated microgrid.

The boost converter, LCL filter, transmission line, and load are in turn explained and their sizing is determined, but first are the system basics determined and the controller parameters are chosen.

5.1 System basics

The inverters will transform power from a direct voltage with 750 V amplitude to a three-phase alternating voltage with an amplitude of 400 V (line-line). The inverters will be rated for 10 kVA and be able to supply equal amounts of both active and reactive power. According to the regulations on voltage quality, [22], the maximum allowed deviation on the voltage magnitude in Norway is ± 5%. There is also a requirement of how balanced the three-phase voltages have to be. The unbalance factor V_{-}/V_{+}, defined as the ratio of the negative sequence to the positive sequence voltage, should be less than 2%. In addition, there is a requirement for how much harmonic distortion that is allowed in the grid. The authorities in Norway say that a total harmonic distortion of 5% in the voltage as an average over a week is the absolute maximum. This is therefore set as the upper limit for the load voltage. The same regulation states that the frequency in an isolated microgrid should be within ± 2% of 50 Hz. In the main grid, the frequency is more tightly controlled and therefore a maximum deviation of ± 0.5% is chosen also for this model. The requirements are together with the base values summarized in table 1.

Name	Symbol	Value
Nominal phase voltage	V_n	230.94 V (RMS)
Nominal frequency	f_n	50 Hz
Rated active power	P_{rated}	10 kW
Rated reactive power	Q_{rated}	10 kVAR
Voltage deviation	Δ_v	0.05
Frequency deviation	Δ_ω	0.005
Switching frequency	f_{sw}	15 kHz
Upper limit THD	THD_{max}	5%
Nominal DC side voltage	V_{DC}	750 V

Table 1: System parameters for the microgrid.

5.2 Parameter values for droop control

In the simulation model, both inverters in the grid are assumed to be equal and controlled equally. The base values for the droop control of both inverters are therefore as given in table 2. The regulator gains and the droop coefficient are derived previously in section 3. The additional parameter ω_f is the cut off frequency for a low pass filter used in the active and reactive power calculation. The filter gives a stable output which enables the power measurement to be used in the droop controller.

The droop controller can regulate its set points of output active and reactive power in order to control the frequency and the voltage magnitude. This kind of regulations is called secondary control and is used to change the operating point. By increasing the active power set point, the grid frequency will increase and by increasing the reactive power set point, the voltage will increase. The sharp eye might have noticed that the virtual oscillator control is not defined with such capabilities. With that control method is the no-load operation used as an effective set point. To be consistent in the comparison, the droop controller is also set to behave in the same way. This is obtained if the set points of the active and reactive power output are set to zero. It should, however, be clearly stated that this is not a common set point and it will lead to deviations in voltage and frequency that could have been avoided with the droop control method.

5.3 Parameter values for virtual oscillator control

The virtual oscillator control parameter values are for the base case given in table 3. The gains, σ, α and C are derived in section 4.5 where their values are also determined. The inductance is calculated according to the resonance frequency relation in eq. (48). This ensures that the oscillator oscillates at 50 Hz. The resistance of the RLC parallel in the oscillator control is simply the negative inverse of σ. This is as presented in [19] in order to make the control circuit behave as a Van der Pol oscillator.

Name	Symbol	Value
$P - f$ Droop coefficient	n_p	1.586×10^{-4}
$Q - V$ Droop coefficient	m_q	1.21×10^{-3}
Cutoff frequency for the lowpass filter	ω_f	31.416 rad/s
Proportional gain in voltage regulator	K_{pv}	62.411×10^{-3}
Integral gain in voltage regulator	K_{iv}	26.737
Proportional gain in current regulator	K_{pc}	10.537
Integral gain in current regulator	K_{ic}	4.514×10^{4}
Active power set point	$P*$	0
Reactive power set point	Q^*	0

Table 2: Base case parameters for the droop control

Name	Symbol	Value
Voltage gain	K_v	242.287
Current gain	K_i	65.818×10^{-3}
Oscillator conductance	σ	9.048 S
Current source factor	α	6.032
Oscillator capacitance	C	286.562×10^{-3} F
Oscillator inductance	L	35.357×10^{-6} H
Oscillator resistance	R	$-0.110\ \Omega$

Table 3: Base case parameters for the virtual oscillator control

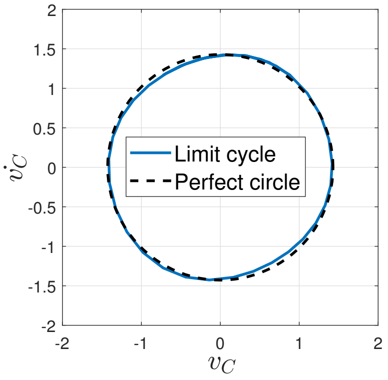

Figure 9: Limit cycle with $C = 0.286$ F and $\sigma = 9.05$ as in the base case.

The oscillations in the Van der Pol oscillator will not behave as a perfect fundamental sinusoid but have a slightly shifted waveform. The deviation from a perfect sinus can be visualized in a phase plot of the oscillator. The derivation of the plot is shown in section 12.1 and the result with the parameters as in table 3 is shown in fig. 9. The more cylindrical the phase plot is, the more similar to an ideal sinus will the voltage in the oscillator be. With the base values that were chosen in this thesis, there is not much deviation from the perfect circle that is added for comparison.

5.4 Description of simulation model components

5.4.1 Boost Converter

In order to model the DC side of the inverter, a voltage source and a boost converter are implemented in the simulation. The voltage source resembles a group of PV panels and an associated battery storage system generating power at a constant voltage. The boost converter increases the voltage up to the designated level. Real PV panels would vary the generation and voltage level according to the irradiation and temperature, but these variations are usually at a much slower time scale than the system dynamics of the inverter control. Additionally, since the PV panels are set to be connected with batteries the constant voltage approximation is increasingly justified.

Having a variable DC side enables harmonic distortions to propagate between the DC and the AC side of the inverter. This could be of importance in the review of the controller. A simpler model with a constant direct voltage would conceal the slightly oscillating voltage input to the inverter that occurs when a boost converter is applied. This model is for that reason closer to a real situation and provides more valid results.

Fig. 10 shows the DC side of the inverter used in the simulations. The boost converter in simple terms works by charging the capacitor to a level corresponding to the reference point set as V_{DC} in the figure. This is obtained by controlling the switch which is turned on and off to make the diode conduct or block the current from the inductor. The size of the capacitor determines the voltage ripple, and the size of the inductor is proportional to the current ripple.

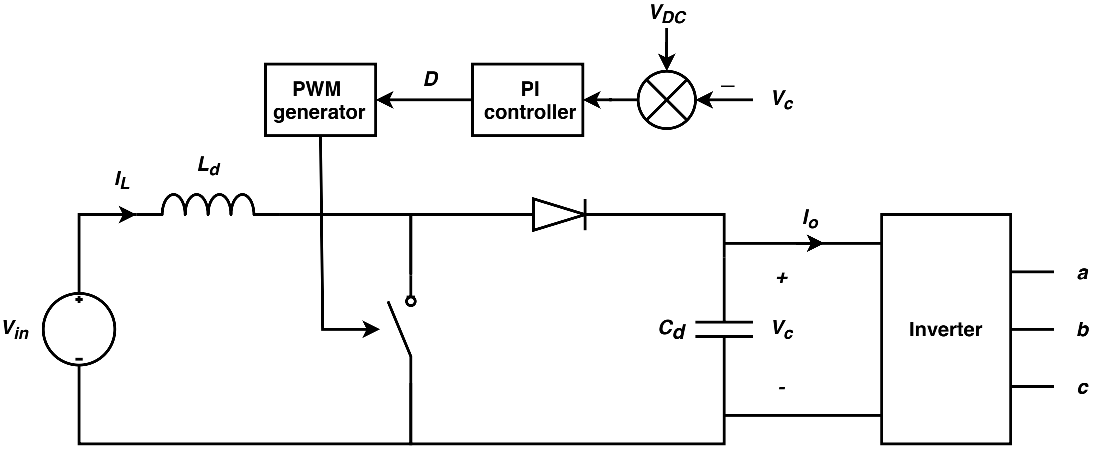

Figure 10: Diagram of the boost converter connected between the voltage source and the inverter. The PI control used to maintain the capacitor voltage is also shown.

Following the procedure in [23], the inductance L_d is set to achieve continuous conduction mode. This yields a minimum value for the inductance. In order to have a stable voltage, the current should be varying with a ripple of 20 - 40%. This creates a boundary for the maximum inductor size. The inductor is set to be in between these values. The voltage at the capacitor is required to have as constant voltage as possible without making the capacitance too large as this would increase the necessary size and cost of the converter. Since the boost converter is connected to an inverter which can represent a varying load, simulations were performed to find a fitting capacitance that enabled voltage ripples of no more than 1% at rated load.

To regulate the input voltage to the inverter at its nominal value, a PI regulator is implemented. The regulator outputs the duty ratio of the switch as

$$D(s) = K_p \left(1 + \frac{1}{T_i s}\right) \frac{V_{DC} - V_c}{V_{DC}} \tag{100}$$

Using the Ziegler-Nichols tuning method presented in [24], possible proportional gain and integration time constants are found. The classical method gave too large overshoots, more than 1% voltage ripple. This made it necessary to change the regulator gains slightly. The resulting values giving satisfying regulation are shown in table 4.

5.4.2 LCL filter

The output of all inverters contains higher order harmonics as a result of the switching process. This output needs to be filtered in order to achieve a decent alternating voltage. Typically a passive LC or LCL filter is used to attenuate the higher order harmonics. The LC filter is able to attenuate 40 dB/decade at frequencies above its cut off frequency, while the LCL filter provides 60 dB/decade. The more efficient LCL filter is

Parameter	Symbol	Value
PV voltage source	V_{in}	400 V
Nominal input voltage	V_{DC}	750 V
Average duty cycle	$\overline{D}$	0.467
DC side inductor	L_d	1.659 mH
DC side capacitor	C_d	2000 μF
Switching frequency	f_{sw}	15×10^3 Hz
Proportional gain	K_p	0.225
Integration time	T_i	0.0131 s

Table 4: Parameter values for the boost converter

chosen as this also provides better decoupling between the filter and the grid impedance [7]. A single-phase equivalent of the LCL filter is shown in fig. 11. The series resistances, R_c and R_g model the parasitic resistances related to the inductors L_c and L_g. The resistance, R_d, in series with the capacitor, is a damping resistor. This kind of passive damping is often included in the filter as this will reduce the amplification near the filter's resonance frequency. But, it comes with the cost of slightly reduced attenuation as well as giving increased power losses. The gain was found to outweigh the cost during initial simulations and the damping resistor was therefore implemented. The design of the filter values is regarded outside of the scope of this thesis. The values are therefore, without further explanation, calculated according to the method described in [7]. The result is given in table 5.

R_c	L_c	R_g	L_g	R_d	C_f
0.3 mΩ	339 μH	0.2 mΩ	203 μH	0.84 Ω	45.1 μF

Table 5: Filter parameter values. The parasitic resistances are taken from the datasheet of a typical inductor with the calculated inductance

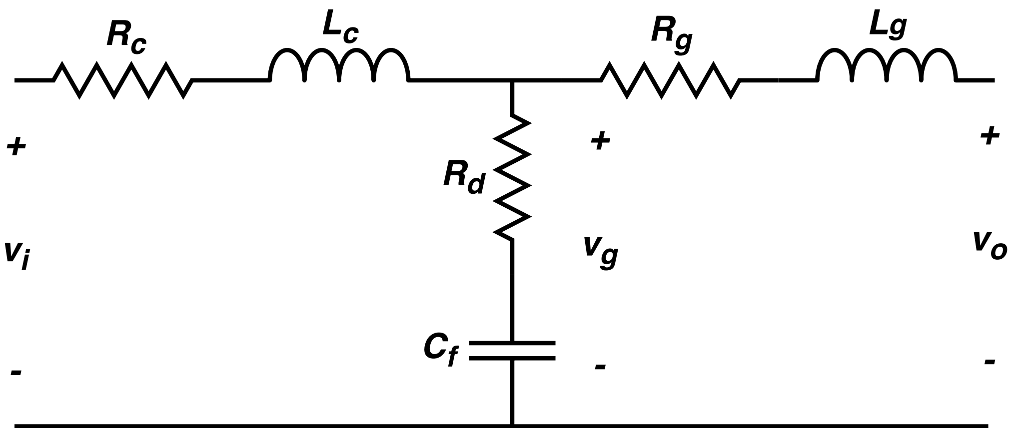

Figure 11: LCL filter at the inverter output

5.4.3 Line impedance

The distributed generation in the microgrid is not assumed to be located at the same spot as where the demand is. Instead, the sources are placed with varying distances between them and the common load. The distances vary from 2 to 4 km. To model these transmission lines, the short line model presented in [15] is used. Due to the short lengths and low voltage level, the capacitance in the line can be neglected. The line is therefore represented by a series connection of a resistor and an inductor.

The per length resistance and reactance of the transmission line is taken from [13]. Here CIGRE, International Council on Large Electric Systems, presented a benchmark microgrid with typical line impedances. The values for the chosen overhead line and the resulting line impedances are presented in table 6. Note that the R/X ratio is much higher than in the traditional transmission lines because of the low voltage level.

From	To	Resistance	Reactance	Length	Impedance
Inverter 1	Load	0.397 Ω/km	0.279 Ω/km	2 km	$0.794 + j0.558\ \Omega$
Inverter 2	Load	0.397 Ω/km	0.279 Ω/km	4 km	$1.588 + j1.116\ \Omega$

Table 6: Line impedances between the inverters and the load

5.4.4 Common load

The demand in the microgrid is modeled as one common load. The load draws power depending on the voltage. This means it is represented by a constant impedance if the frequency is constant. The load is assumed to be inductive and have a per phase resistance, R_L, and inductance, L_L with values calculated according to

$$R_L + j\omega L_L = 3\frac{V_n^2}{(P_L + jQ_L)^*} \tag{101}$$

Here, the voltage V_n is the nominal load voltage with respect to ground and $(P_L + jQ_L)^*$ is the conjugate of the apparent power drawn by the load.

The base case scenario is set to have a load demand of $8.0 + j2.0$ kVA at rated voltage if one inverter is operating. If two inverters are simulated, they share a load twice this big, i.e. $16.0 + j4.0$ kVA at the rated voltage. The load impedances used in the analytical analysis are then as given in table 7.

Inverters	R_L	L_L
1	18.824 Ω	4.706 H
2	9.412 Ω	2.353 H

Table 7: Load impedance for the base cases used in the simulation

5.4.5 Variable resistor, inductor, and capacitor

Since part of this thesis is devoted to examining how a varying $\epsilon = \sqrt{\frac{L}{C}}$ and a varying $\sigma = -\frac{1}{R}$ is influencing the performance of the virtual oscillator controller, the simulation model should be able to handle variations of these two parameters. However, the Simscape Electrical environment in Simulink does not contain variable models of either resistors, inductors or capacitors. The component values need to be known in advance of the simulation. Since these electrical components are part of the virtual oscillator, and thus artificial in a physical sense, the action needed to actually vary the L and the C does not need to be considered. The oscillator dynamics will for a real inverter just be programmed onto a circuit board. Therefore, to bypass this simulation issue, the resistor, inductor, and capacitor are manually implemented following the general relationships in eq. (102).

$$\begin{aligned} v_R(t) =& R(t) i_R(t) \\ v_L(t) =& \frac{d}{dt}(L(t) \cdot i_L(t)) \\ i_C(t) =& \frac{d}{dt}(C(t) \cdot v_C(t)) \end{aligned} \tag{102}$$

This yields

$$\begin{aligned} i_R(t) =& \frac{v_R(t)}{R(t)} \\ i_L(t) =& \frac{1}{L(t)} \int_0^t v_L(\tau) d\tau \\ v_C(t) =& \frac{1}{C(t)} \int_0^\tau i_C(\tau) d\tau \end{aligned} \tag{103}$$

By using a voltage/current measurement, integrate and divide by the desired value of L/C, a controlled voltage/current source can be regulated. This will then function as an inductor/capacitor of varying size. For the variable resistor it is much easier, just regulate a current source according to the voltage measurement divided by the chosen resistance. To illustrate the concept, the variable inductor and capacitor are shown in fig. 12a and 12b.

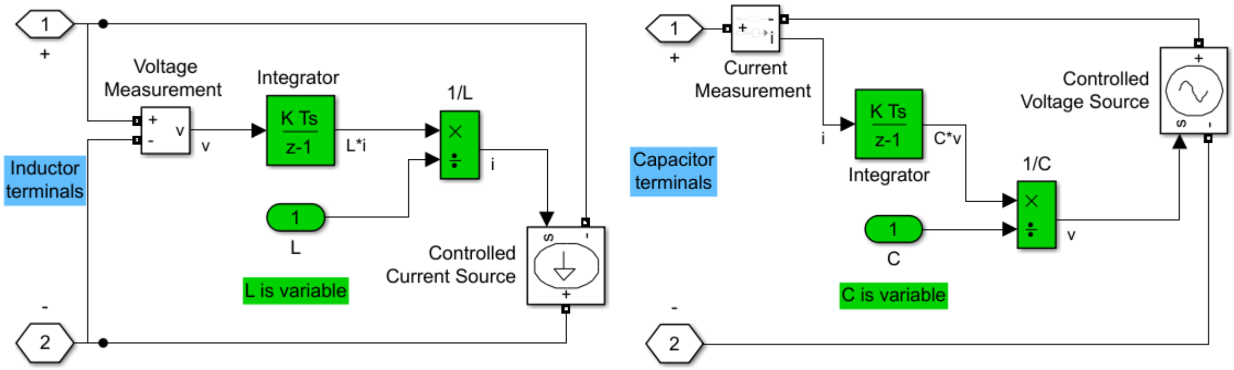

(a) Variable Inductor (b) Variable Capacitor

Figure 12: Simulink model of variable reactances.

6 Small-signal state-space model of a double-inverter system

A small-signal model is an approximated linear representation of a system around a steady-state point of operation. This representation facilitates system analysis related to stability, response characteristics, participation factors and tuning of parameters. These analyses are carried out based on the eigenvalues of the system, how the values change for small changes in operating conditions and how the states contribute to these eigenvalues. There have been performed such analysis on single inverter systems before. In [5], an idealized version of a single inverter was modeled with both droop control and virtual oscillator control.

The equilibrium points were obtained through ideal assumptions instead of steady state values and also the current flowing to the load was neglected. A more realistic comparison was performed in [17] where a three-phase system was considered. In this paper, the operating point was obtained with simulations and the control parameters were chosen to have both methods behave similarly in steady state. To the author's understanding, there have not been any eigenvalue analyzes of the virtual oscillator control method when multiple inverters are considered. The analyzes in this thesis where two inverters are cooperating to serve a common load will thus move into an unsolved field.

In order to make a small-signal model, all the relevant system dynamics must be written in a form where they are related to each other. A system of differential equations is, therefore, the end goal of the derivation. There will be different equations describing the droop method and the virtual oscillator method, but since only the inverter control is what differs between the methods, the dynamics of the line and the load will be the same. The equations for the line and the load are derived from well-known voltage and current relations. The DC side of the inverters are not taken into account in the state space model as the inverter is essentially considered as an ideal voltage source. The inverter control methods have already been described in previous sections and these will form the basis for fulfilling the system description.

The dynamic equations of each inverter are most conveniently described in the inverters local dq-reference frame. The two-inverter system will, because of this, contain two reference frames with parameters that need to be transformed between the different frames. The two reference frames are chosen to rotate at the angular speed given by the derivative of the voltage phase angle at the inverters. To reduce the number of necessary transformations, the local frame of inverter 1 is used as a common reference frame for both output impedances and for the load. Thus, only the remaining inverter is described in its local frame.

The conversion between the reference frames is obtained with the transformation matrix according to eq. (104) and (105). The first equation transforms the voltage output in inverter 2 from its separate reference frame into the common one. The second transforms the current output from the common frame to inverter 2's reference frame. The difference is the sign used for the angle difference. A generic case showing how the different reference system can be related to each other is visualized in fig. 13. The common reference frame of inverter 1 is denoted with capital letters in the figure.

$$\begin{bmatrix} v_{g2}^{D} \\ v_{g2}^{Q} \end{bmatrix} = \begin{bmatrix} cos(-\delta_{21}) & sin(-\delta_{21}) \\ -sin(-\delta_{21}) & cos(-\delta_{21}) \end{bmatrix} \begin{bmatrix} v_{g2}^{d} \\ v_{g2}^{q} \end{bmatrix} \tag{104}$$

$$\begin{bmatrix} i_{o2}^{d} \\ i_{o2}^{q} \end{bmatrix} = \begin{bmatrix} cos(\delta_{21}) & sin(\delta_{21}) \\ -sin(\delta_{21}) & cos(\delta_{21}) \end{bmatrix} \begin{bmatrix} i_{o2}^{D} \\ i_{o2}^{Q} \end{bmatrix} \tag{105}$$

The topology of the state space model is as sketched in fig. 14. The output impedances are denoted as Z_o and the load impedance as Z_L. In this representation there is an additional current i_u, which is used to model disturbances on the load. Using this approach, some of the features of the Simulink simulations can also be analyzed within the state space representation. In order to ensure a well-defined voltage at the point of common coupling a large virtual resistance, R_n, is assumed between the load node and ground.

6.1 Deriving the state equations for the output impedances and the load

The state equations are derived in the dq-reference frame after first developing the relations using well-known circuit theory such as Kirschoff's voltage and current law denoted by KVL and KCL, respectively.

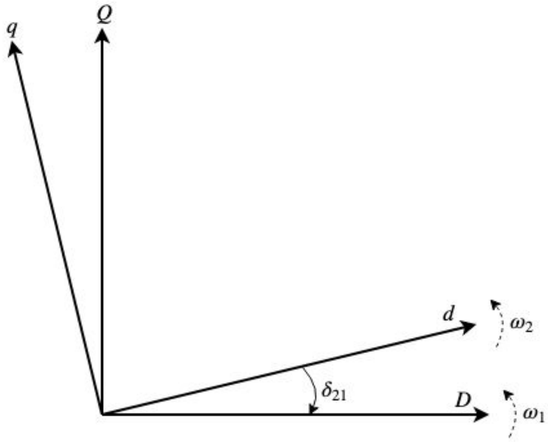

Figure 13: Plot of the difference between the two reference frames for a generic case

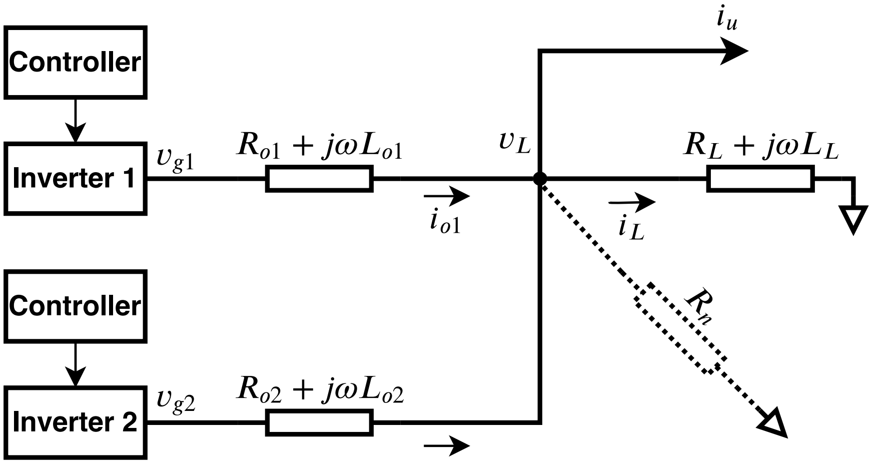

Figure 14: Simplified structure of the microgrid used in the state space representation

KVL from the output of the inverter to the load gives for the single-phase equivalent

$$\begin{aligned} v_{g1} &= R_{o1} i_{o1} + L_{o1} \frac{di_{o1}}{dt} + v_L \\ v_{g2} &= R_{o2} i_{o2} + L_{o2} \frac{di_{o2}}{dt} + v_L \end{aligned} \tag{106}$$

KVL from load to ground gives

$$v_L = R_L i_L + L_L \frac{di_L}{dt} \tag{107}$$

For the three-phase circuit, solving for the derivatives and employing space-phasor notation, these relations are equivalent to

$$\begin{aligned} L_{o1} \frac{d\vec{i_{o1}}}{dt} &= -R_{o1} \vec{i_{o1}} + \vec{v_{g1}} - \vec{v_L} \\ L_{o2} \frac{d\vec{i_{o2}}}{dt} &= -R_{o2} \vec{i_{o2}} + \vec{v_{g2}} - \vec{v_L} \end{aligned} \tag{108}$$

$$L_L \frac{d\vec{i_L}}{dt} = -R_L \vec{i_L} + \vec{v_L} \tag{109}$$

The relations are transformed into dq-coordinates by using $f(\vec{t}) = (f_D + jf_Q)\, e^{j\omega_1 t}$. The reference frame is set to rotate with angular speed ω_1, i.e 2π times the frequency of inverter 1's voltage output. In the following section, $(\cdot)^D$ and $(\cdot)^Q$ denote the d- and q-component of inverter 1's reference frame respectively. Starting with the current out of the inverters, the dq-transformation gives

$$\begin{aligned} L_{o1}\frac{d}{dt}\left[i_{o1}^D e^{j\omega_1 t} + j i_{o1} e^{j\omega_1 t}\right] &= -R_{o1}\left(i_{o1}^D + j i_{o1}^Q\right) e^{j\omega_1 t} + \left(v_{g1}^D + j v_{c1}^Q\right) e^{j\omega_1 t} - \left(v_L^D + j v_L^Q\right) e^{j\omega_1 t} \\ L_{o2}\frac{d}{dt}\left[i_{o2}^D e^{j\omega_1 t} + j i_{o2} e^{j\omega_1 t}\right] &= -R_{o2}\left(i_{o2}^D + j i_{o2}^Q\right) e^{j\omega_1 t} + \left(v_{g2}^D + j v_{c2}^Q\right) e^{j\omega_1 t} - \left(v_L^D + j v_L^Q\right) e^{j\omega_1 t} \end{aligned} \tag{110}$$

The product rule, simplification, and splitting of real and imaginary components yield

$$\begin{aligned} \frac{d}{dt} i_{o1}^D &= -\frac{R_{o1}}{L_{o1}} i_{o1}^D + \omega_1 i_{o1}^Q + \frac{1}{L_{o1}}\left(v_{g1}^D - v_L^D\right) \\ \frac{d}{dt} i_{o1}^Q &= -\frac{R_{o1}}{L_{o1}} i_{o1}^Q - \omega_1 i_{o1}^D + \frac{1}{L_{o1}}\left(v_{g1}^Q - v_L^Q\right) \end{aligned} \tag{111}$$

The exact same applies to the current out of inverter 2. Note that since the output impedance of inverter 2 is referred to inverter 1's reference frame, ω_1 is used in the transformation.

$$\begin{aligned} \frac{d}{dt} i_{o2}^D &= -\frac{R_{o2}}{L_{o2}} i_{o1}^D + \omega_1 i_{o2}^Q + \frac{1}{L_{o2}}\left(v_{g2}^D - v_L^D\right) \\ \frac{d}{dt} i_{o2}^Q &= -\frac{R_{o2}}{L_{o1}} i_{o2}^Q - \omega_1 i_{o2}^D + \frac{1}{L_{o2}}\left(v_{g2}^Q - v_L^Q\right) \end{aligned} \tag{112}$$

The load current is equivalently described as

$$\begin{aligned} \frac{d}{dt} i_L^D &= -\frac{R_L}{L_L} i_L^D + \omega_1 i_L^Q + \frac{1}{L_L} v_L^D \\ \frac{d}{dt} i_L^Q &= -\frac{R_L}{L_L} i_L^Q - \omega_1 i_L^D + \frac{1}{L_L} v_L^Q \end{aligned} \tag{113}$$

The load voltage is treated as an input to the inverter subsystems. To ensure a well-defined voltage, a large virtual resistance, R_n, between the load node and ground is assumed. The resistance is set to be large so it will have a minimum impact on the system dynamics [14]. Additionally, this resistance aids in connecting the current disturbance, i_u, to the rest of the system dynamics. This current represent load changes and is treated as an input to the system. This way, the state space model and the time-step simulation model both are able to describe the system trajectory following load disturbances.

Ohm's law on the load node yields then

$$v_L = R_n\left(i_{o1} + i_{o2} - i_L - i_u\right) \tag{114}$$

and in the common dq reference frame

$$\begin{aligned} v_L^D &= R_n\left(i_{o1}^D + i_{o2}^D - i_L^D - i_u^D\right) \\ v_L^Q &= R_n\left(i_{o1}^Q + i_{o2}^Q - i_L^Q - i_u^Q\right) \end{aligned} \tag{115}$$

6.2 Deriving state equations in the droop controller

The droop controller measures the current out of and the voltage over the capacitor in the LCL filter. These measurements are used to calculate the output power of the inverter. After filtering the instantaneous power with a low-pass filter and comparing this with its reference value, the voltage amplitude and frequency is set. This reference is further improved by the inner control loop, i.e. the voltage and the current controller. This reference is used in the PWM generator to control the inverter switches.

The substructures are working in different time frames with the PWM generator and the inverter switching as the fastest unit. The current regulator is set to have a bandwidth of one-tenth of the switching frequency. The factor of one-tenth is also used between the voltage and the current regulator. This is according to the rule of thumb sufficient bandwidth between the controllers to ensure they are not inflicting the faster units regulation. With the chosen switching frequency of 15 kHz, the current and voltage regulator will have a bandwidth of 9.42×10^3 rad/s and 942 rad/s respectively. This is 30 times the bandwidth for the low-pass power filter, 31.4 rad/s. The large difference in time constants enables a reduction of model complexity. Since the droop dynamics is of main interest and the regulators in the inner loop are so much faster, they can be assumed ideal indicating that they can be neglected in the state space model.

Continuing in the inverters separate dq-reference frames, the instantaneous real and reactive power output of the inverters are given in eq. (116). Note that inverter 2's dq-reference frame is denoted by $(\cdot)^{dq}$ and differ from the common reference frame set by inverter 1.

$$\begin{aligned} P_{1,ins} &= \frac{3}{2}\left(v_{g1}^{D} i_{o1}^{D} + v_{g1}^{Q} i_{o1}^{Q}\right) \\ Q_{1,ins} &= \frac{3}{2}\left(v_{g1}^{Q} i_{o1}^{D} - v_{g1}^{D} i_{o1}^{Q}\right) \\ P_{2,ins} &= \frac{3}{2}\left(v_{g2}^{d} i_{o2}^{d} + v_{g2}^{q} i_{o2}^{q}\right) \\ Q_{2,ins} &= \frac{3}{2}\left(v_{g2}^{q} i_{o2}^{d} - v_{g2}^{d} i_{o2}^{q}\right) \end{aligned} \tag{116}$$

The droop relation is as given in eq. (83), but is here given in dq-reference frame.

$$\begin{aligned} \omega_i &= \omega^* - n_p\left(P - P^*\right) \\ v_g^D &= V^* - m_q\left(Q - Q^*\right) \\ v_g^Q &= 0 \end{aligned} \tag{117}$$

As shortly described above, the real and reactive power are measured and filtered using a first order low-pass filter. The filter is described by the transfer function in eq. (118) which means it attenuates components with a frequency higher than the selected cutoff frequency, w_f.

$$\begin{aligned} P &= \frac{w_f}{s + w_f} P_{ins} \\ Q &= \frac{w_f}{s + w_f} Q_{ins} \end{aligned} \tag{118}$$

This relation can be altered to find the state equation for the filter since $s \implies d/dt$ in time domain.

$$\begin{aligned}
sP_1 &= \frac{dP_1}{dt} = \omega_f \left(P_{1,ins} - P_1\right) = -\omega_f P_1 + \frac{3}{2}\omega_f \left(v_{g1}^D i_{o1}^D + v_{g1}^Q i_{o1}^Q\right) \\
sQ_1 &= \frac{dQ_1}{dt} = \omega_f \left(Q_{1,ins} - Q_1\right) = -\omega_f Q_1 + \frac{3}{2}\omega_f \left(v_{g1}^Q i_{o1}^D - v_{g1}^D i_{o1}^Q\right) \\
sP_2 &= \frac{dP_2}{dt} = \omega_f \left(P_{2,ins} - P_2\right) = -\omega_f P_2 + \frac{3}{2}\omega_f \left(v_{g2}^d i_{o2}^d + v_{g2}^q i_{o2}^q\right) \\
sQ_2 &= \frac{dQ_2}{dt} = \omega_f \left(Q_{2,ins} - Q_2\right) = -\omega_f Q_2 + \frac{3}{2}\omega_f \left(v_{g2}^q i_{o2}^d - v_{g2}^d i_{o2}^q\right)
\end{aligned} \tag{119}$$

The phase angle, $\delta_{21} = \delta_2 - \delta_1$, is the angle between the two voltages and thus also the angle between the two reference frames as shown in fig. 13. The change in the phase angle is therefore described by the angular speed of the reference systems. Since inverter 1 is chosen as the reference, the angle difference between inverter 1 and the reference is zero.

$$\begin{aligned}
\frac{d\delta_{11}}{dt} &= \omega_1 - \omega_1 = 0 \\
\frac{d\delta_{21}}{dt} &= \omega_2 - \omega_1 = -n_{p2} P_2 + n_{p1} P_1 + n_{p2} P_2^* - n_{p1} P_1^*
\end{aligned} \tag{120}$$

6.3 Obtaining linearized state-space model for the droop controlled parallel inverters

A state space model is of the form

$$\dot{\mathbf{x}} = \mathbf{A}\mathbf{x} + \mathbf{B}\mathbf{u} \tag{121}$$

where $\mathbf{x}$ is the state vector, $\mathbf{A}$ is the system matrix and $\mathbf{u}$ and $\mathbf{B}$ is the input vector and input matrix respectively. This kind of representation is able to provide a compact way of modeling the system. The states are evolving through time and the system of differential equations give their dynamic behavior.

Since the set of equations described above contain nonlinear equations, they are linearized at a steady-state working point according to the procedure in [1]. The procedure involves partial differentiation of the state equations, $\mathbf{f}$, with respect to the state variables, $\mathbf{x}$, and the input variables, $\mathbf{u}$. The variables are evaluated at their steady-state values denoted by $\mathbf{x^p}$ and $\mathbf{u^p}$. The steady state values are in the linearization denoted as uppercases. For instance, V_{g1}^D is the steady state d-axis voltage output of inverter 1 in the common dq reference frame.

The resulting linear state-space model is then

$$\Delta\dot{\mathbf{x}} = \frac{\partial \mathbf{f}}{\partial \mathbf{x}}\bigg|_{\mathbf{x^p}} \Delta\mathbf{x} + \frac{\partial \mathbf{f}}{\partial \mathbf{u}}\bigg|_{\mathbf{u^p}} \Delta\mathbf{u} \tag{122}$$

where states of the system are chosen as

$$\mathbf{x} = \begin{bmatrix} P_1 & Q_1 & i_{o1}^D & i_{o1}^Q & \delta_{21} & P_2 & Q_2 & i_{o2}^D & i_{o2}^Q & i_L^D & i_L^Q \end{bmatrix}^T \tag{123}$$

and the input is

$$\mathbf{u} = \begin{bmatrix} i_u^D & i_u^Q \end{bmatrix}^T \tag{124}$$

Evaluating the partial differentiation gives the linearized state equations as

$$
\begin{aligned}
\Delta\dot{P}_1 &= -\omega_f P_1 + \frac{3}{2}\omega_f \left(I_{o1}^{D}\Delta v_{g1}^{D} + I_{o1}^{Q}\Delta v_{g1}^{Q} + v_{g1}^{D}\Delta i_{o1}^{D} + v_{g1}^{Q}\Delta i_{o1}^{Q} \right) \\
\Delta\dot{Q}_1 &= -\omega_f Q_1 + \frac{3}{2}\omega_f \left(I_{o1}^{D}\Delta v_{g1}^{Q} - I_{o1}^{Q}\Delta v_{g1}^{D} + v_{g1}^{Q}\Delta i_{o1}^{D} - v_{g1}^{D}\Delta i_{o1}^{Q} \right) \\
\Delta\dot{i}_{o1}^{D} &= \frac{1}{L_{o1}}\Delta v_{g1}^{D} - \frac{R_{o1}}{L_{o1}}\Delta i_{o1}^{D} + \omega_1\Delta i_{o1}^{Q} + I_{o1}^{Q}\Delta\omega_1 - \frac{1}{L_{o1}}\Delta v_{L}^{D} \\
\Delta\dot{i}_{o1}^{Q} &= \frac{1}{L_{o1}}\Delta v_{g1}^{Q} - \frac{R_{o1}}{L_{o1}}\Delta i_{o1}^{Q} - \omega_1\Delta i_{o1}^{D} - I_{o1}^{D}\Delta\omega_1 - \frac{1}{L_{o1}}\Delta v_{L}^{Q} \\
\Delta\dot{\delta}_{21} &= \Delta\omega_2 - \Delta\omega_1 \\
\Delta\dot{P}_2 &= -\omega_f P_2 + \frac{3}{2}\omega_f \left(I_{o2}^{d}\Delta v_{g2}^{d} + I_{o2}^{q}\Delta v_{g2}^{q} + v_{g2}^{d}\Delta i_{o2}^{d} + v_{g2}^{q}\Delta i_{o2}^{q} \right) \\
\Delta\dot{Q}_2 &= -\omega_f Q_2 + \frac{3}{2}\omega_f \left(I_{o2}^{d}\Delta v_{g2}^{q} - I_{o2}^{q}\Delta v_{g2}^{d} + v_{g2}^{q}\Delta i_{o2}^{d} - v_{g2}^{d}\Delta i_{o2}^{q} \right) \\
\Delta\dot{i}_{o2}^{D} &= \frac{1}{L_{o2}}\Delta v_{g2}^{D} - \frac{R_{o2}}{L_{o2}}\Delta i_{o2}^{D} + \omega_1\Delta i_{o2}^{Q} + I_{o2}^{Q}\Delta\omega_1 - \frac{1}{L_{o2}}\Delta v_{L}^{D} \\
\Delta\dot{i}_{o2}^{Q} &= \frac{1}{L_{o2}}\Delta v_{g2}^{Q} - \frac{R_{o2}}{L_{o2}}\Delta i_{o2}^{Q} - \omega_1\Delta i_{o2}^{D} - I_{o2}^{D}\Delta\omega_1 - \frac{1}{L_{o2}}\Delta v_{L}^{Q} \\
\Delta\dot{i}_{L}^{D} &= \frac{1}{L_{L}}\Delta v_{L}^{D} - \frac{R_{L}}{L_{L}}\Delta i_{L}^{D} + \omega_1\Delta i_{L}^{Q} + I_{L}^{Q}\Delta\omega_1 \\
\Delta\dot{i}_{L}^{Q} &= \frac{1}{L_{L}}\Delta v_{L}^{Q} - \frac{R_{L}}{L_{L}}\Delta i_{L}^{Q} - \omega_1\Delta i_{L}^{D} - I_{L}^{D}\Delta\omega_1
\end{aligned}
\tag{125}
$$

In eq. (125), there are some equations containing parameters in the reference frame they are not originally defined in. These parameters are v_{g2}^{DQ} and i_{o2}^{dq}. These should be transformed to make the model unified. But since the transformations in eq. (104) and (105) are not linear, the transformation as well needs to be linearized.

Since the inverters and their output impedances are close to matching, and their set outputs are matched, the angle difference will not be large. The transformation can thus be approximated for small angle differences by applying

$$
sin(\delta_{21}) \approx \delta_{21}, \quad cos(\delta_{21}) \approx 1 \tag{126}
$$

This yield the linearized transformations as

$$
\begin{aligned}
\Delta v_{g2}^{D} &\approx \Delta v_{g2}^{d} - \Delta\delta_{21} v_{g2}^{q} - \delta_{21}\Delta v_{g2}^{q} \\
\Delta v_{g2}^{Q} &\approx \Delta v_{g2}^{q} + \Delta\delta_{21} v_{g2}^{d} + \delta_{21}\Delta v_{g2}^{d}
\end{aligned}
\tag{127}
$$

$$
\begin{aligned}
\Delta i_{o2}^{d} &\approx \Delta i_{o2}^{D} + \Delta\delta_{21} I_{o2}^{Q} + \delta_{21}\Delta i_{o2}^{Q} \\
\Delta i_{o2}^{q} &\approx \Delta i_{o2}^{Q} - \Delta\delta_{21} I_{o2}^{D} - \delta_{21}\Delta i_{o2}^{D}
\end{aligned}
\tag{128}
$$

One can also note that some state equations depend on the varying frequency of the reference inverter. This is because the microgrid does not have a fixed frequency. Additionally, some equations depend on the output voltage of the inverters. These parameters are controlled by the droop controller according to eq. (129).

$$\begin{aligned}\Delta v_{g1}^{D} &= -m_{q1}\Delta Q_1\\ \Delta v_{g1}^{Q} &= 0\\ \Delta\omega_1 &= -n_{p1}\Delta P_1\\ \Delta v_{g2}^{d} &= -m_{q2}\Delta Q_2\\ \Delta v_{g2}^{q} &= 0\\ \Delta\omega_2 &= -n_{p2}\Delta P_2\end{aligned} \tag{129}$$

Inserting these droop equations as well as the equation for the load voltage in eq. (115) in the linearized state equations enable the system to be written in matrix form as

$$\mathbf{\Delta\dot{x}} = \mathbf{A\Delta x} + \mathbf{B\Delta u} \tag{130}$$

where

$$\mathbf{A} =$$

$$\begin{bmatrix}
-\omega_f & -\frac{3}{2}\omega_f I_{o1}^{D} & \frac{3}{2}\omega_f V_{c1}^{D} & \frac{3}{2}\omega_f V_{c1}^{Q} & 0 & 0 & 0 & 0 & 0 & 0 & 0\\
0 & -\omega_f+\frac{3}{2}\omega_f m_{q1} I_{o1}^{Q} & \frac{3}{2}\omega_f V_{c1}^{Q} & -\frac{3}{2}\omega_f V_{c1}^{D} & 0 & 0 & 0 & 0 & 0 & 0 & 0\\
-n_{p1}I_{o1}^{Q} & -\frac{m_{q1}}{L_{o1}} & -\frac{R_{o1}+R_n}{L_{o1}} & \omega_1 & 0 & 0 & 0 & -\frac{R_n}{L_{o1}} & 0 & \frac{R_n}{L_{o1}} & 0\\
n_{p1}I_{o1}^{D} & 0 & -\omega_1 & -\frac{R_{o1}+R_n}{L_{o1}} & 0 & 0 & 0 & 0 & -\frac{R_n}{L_{o1}} & 0 & \frac{R_n}{L_{o1}}\\
n_{p1} & 0 & 0 & 0 & 0 & -n_{p2} & 0 & 0 & 0 & 0 & 0\\
0 & 0 & 0 & 0 & \frac{3}{2}\omega_f\left(v_{g2}^{d}I_{o2}^{Q}-v_{g2}^{q}I_{o2}^{D}\right) & -\omega_f & -\frac{3}{2}I_{o2}^{d}m_{q2} & \frac{3}{2}\omega_f\left(v_{g2}^{d}-\delta_{21}^{*}v_{g2}^{q}\right) & \frac{3}{2}\omega_f\left(v_{g2}^{d}\delta_{21}^{*}+v_{g2}^{q}\right) & 0 & 0\\
0 & 0 & 0 & 0 & \frac{3}{2}\omega_f\left(v_{g2}^{d}I_{o2}^{D}+v_{g2}^{q}I_{o2}^{Q}\right) & 0 & \frac{3}{2}\omega_f m_{q2}I_{o2}^{d} & \frac{3}{2}\omega_f\left(\delta_{21}^{*}v_{g2}^{d}+v_{g2}^{q}\right) & \frac{3}{2}\omega_f\left(-v_{g2}^{d}+\delta_{21}^{*}v_{g2}^{q}\right) & 0 & 0\\
-n_{p1}I_{o2}^{Q} & 0 & -\frac{R_n}{L_{o2}} & 0 & -\frac{v_{g2}^{q}}{L_{o2}} & 0 & -\frac{m_{q2}}{L_{o2}} & -\frac{R_{o2}+R_n}{L_{o2}} & \omega_1 & \frac{R_n}{L_{o2}} & 0\\
n_{p1}I_{o2}^{D} & 0 & 0 & -\frac{R_n}{L_{o2}} & \frac{v_{g2}^{d}}{L_{o2}} & 0 & -\frac{\delta_{21}^{*}m_{q2}}{L_{o2}} & -\omega_1-\frac{R_{o2}+R_n}{L_{o2}} & 0 & \frac{R_n}{L_{o2}} & \\
-n_{p1}I_{L}^{Q} & 0 & \frac{R_n}{L_L} & 0 & 0 & 0 & 0 & \frac{R_n}{L_L} & 0 & -\frac{R_L+R_n}{L_L} & \omega_1\\
n_{p1}I_{L}^{D} & 0 & 0 & \frac{R_n}{L_L} & 0 & 0 & 0 & 0 & \frac{R_n}{L_L} & -\omega_1 & -\frac{R_L+R_n}{L_L}
\end{bmatrix} \tag{131}$$

$$\mathbf{B} = \begin{bmatrix}
0 & 0\\
0 & 0\\
\frac{R_n}{L_{o1}} & 0\\
0 & \frac{R_n}{L_{o1}}\\
0 & 0\\
0 & 0\\
0 & 0\\
\frac{R_n}{L_{o2}} & 0\\
0 & \frac{R_n}{L_{o2}}\\
-\frac{R_n}{L_L} & 0\\
0 & -\frac{R_n}{L_L}
\end{bmatrix} \tag{132}$$

6.4 Deriving state equations in the averaged virtual oscillator controller

The calculations are shown with the version corresponding to the conventional droop, meaning that the oscillator output has been rotated by $\Phi = 90°$. The averaged dynamics of the inverter output are then given as derived in previous sections and here rendered for inverter 1.

$$\frac{d\overline{V_1}}{dt} = \frac{1}{2C_1}\left(\sigma_1\overline{V_1} - \frac{3\alpha_1}{2K_{v1}^2}\overline{V_1}^3\right) - \frac{K_{i1}K_{v1}}{6C_1\overline{V_1}}\overline{Q_1} \tag{133}$$

$$\frac{d\overline{\theta_1}^*}{dt} = -\frac{K_{i1}K_{v1}}{6C_1\overline{V_1}^2}\overline{P_1} \tag{134}$$

Total three-phase power is with the normal power variant form of the Park transform

$$\overline{P} \approx \frac{3}{2}\left(v_i^d i_i^d + v_i^q i_i^q\right) \tag{135}$$

$$\overline{Q} \approx \frac{3}{2}\left(-v_i^d i_i^q + v_i^q i_i^d\right) \tag{136}$$

since $v_{i1}^Q = 0$ and $v_{i1}^D \approx \overline{V_1}$, the VOC dynamics can be described for inverter 1 as

$$\frac{dv_{i1}^D}{dt} = \frac{d\overline{V_1}}{dt} \approx \frac{1}{2C_1}\left(\sigma_1 v_{i1}^D - \frac{\alpha_1}{2\sigma_1 K_{v1}^2}(v_{i1}^D)^3\right) + \frac{K_{i1}K_{v1}}{4C_1} i_{i1}^Q \tag{137}$$

$$\omega_1 = \omega^* + \frac{d\overline{\theta}_1^*}{dt} = \omega^* - \frac{K_{i1}K_{v1}}{4C_1 v_{i1}^D} i_{i1}^D \tag{138}$$

The phase angle for the inverters are then

$$\begin{aligned} \frac{d\delta_{11}}{dt} &= \omega_1 - \omega_1 = 0 \\ \frac{d\delta_{21}}{dt} &= \omega_2 - \omega_1 = -\frac{K_{i2}K_{v2}}{4C_2 v_{i2}^d} i_{i2}^d + \frac{K_{i1}K_{v1}}{4C_1 v_{i1}^D} i_{i1}^D \end{aligned} \tag{139}$$

Unlike the droop controller which filters the power measurement, the virtual oscillator controller only needs the current measurement into the LCL filter. By not depending on a low-pass filter, the virtual oscillator is able to react to instantaneous changes. Additionally, this implies that the active and reactive powers which were states in the droop controller, are replaced with the voltage output as the state. This also reduces the model order by one for each inverter in the system.

6.5 Obtaining linearized state space model for the virtual oscillator controlled parallel inverters

The sharp eye might have noted the difference in the power equations with dq-components between the droop and the virtual oscillator. The droop uses the voltage over the capacitor in the LCL filter and the current output of the filter. The virtual oscillator uses the voltage before the LCL filter and the current into the filter. For the complete state space representation, the LCL filter should also be considered in the virtual oscillator state space modeling. However, the difference between the voltage at the inverter terminals and the voltage over the capacitor is quite small for low frequencies when the switching process is considered as ideal. The same is valid for the current into and out of the filter. This justifies a simplification of the model. By neglecting the filter in the state space modeling, the number of states is reduced significantly with negligible impact on the system dynamics. This neglection means that $v_i \approx v_g$ and $i_i \approx i_o$. In order to be consistent with the notations, the latter variant is used in this section.

Following the same linearization process as in section 6.3 with the states of the system given as

$$\mathbf{x} = \begin{bmatrix} v_{g1}^D & i_{o1}^D & i_{o1}^Q & \delta_{21} & v_{g2}^d & i_{o2}^D & i_{o2}^Q & i_L^D & i_L^Q \end{bmatrix}^T \tag{140}$$

and the same disturbance current used as the input

$$\mathbf{u} = \begin{bmatrix} i_u^D & i_u^Q \end{bmatrix}^T \tag{141}$$

the linearized state equations are given as

$$\begin{aligned}
\Delta \dot{v}_{g1}^{D} &= \frac{1}{2C_1}\left(\sigma_1 - \frac{3\alpha_1}{2K_{v1}^2}(v_{g1}^D)^2\right)\Delta v_{g1}^D + \frac{K_{i1}K_{v2}}{4C_1}\Delta i_{o1}^Q \\
\Delta \dot{i}_{i1}^{D} &= \frac{1}{L_{o1}}\Delta v_{g1}^D - \frac{R_{o1}}{L_{o1}}\Delta i_{o1}^D + \omega_1 \Delta i_{o1}^Q + I_{o1}^Q \Delta\omega_1 - \frac{1}{L_{o1}}\Delta v_L^D \\
\Delta \dot{i}_{o1}^{Q} &= \frac{1}{L_{o1}}\Delta v_{g1}^Q - \frac{R_{o1}}{L_{o1}}\Delta i_{o1}^Q - \omega_1 \Delta i_{o1}^D - I_{o1}^D \Delta\omega_1 - \frac{1}{L_{o1}}\Delta v_L^Q \\
\Delta \dot{\delta}_{21} &= \Delta\omega_2 - \Delta\omega_1 \\
\Delta \dot{v}_{g2}^{d} &= \frac{1}{2C_2}\left(\sigma_2 - \frac{3\alpha_2}{2K_{v2}^2}(v_{g2}^d)^2\right)\Delta v_{g2}^d + \frac{K_{i2}K_{v2}}{4C_2}\Delta i_{o2}^q \\
\Delta \dot{i}_{o2}^{D} &= \frac{1}{L_{o2}}\Delta v_{g2}^D - \frac{R_{o2}}{L_{o2}}\Delta i_{o2}^D + \omega_1 \Delta i_{o2}^Q + I_{o2}^Q \Delta\omega_1 - \frac{1}{L_{o2}}\Delta v_L^D \\
\Delta \dot{i}_{o2}^{Q} &= \frac{1}{L_{o2}}\Delta v_{g2}^Q - \frac{R_{o2}}{L_{o2}}\Delta i_{o2}^Q - \omega_1 \Delta i_{o2}^D - I_{o2}^D \Delta\omega_1 - \frac{1}{L_{o2}}\Delta v_L^Q \\
\Delta \dot{i}_{L}^{D} &= \frac{1}{L_L}\Delta v_L^D - \frac{R_L}{L_L}\Delta i_L^D + \omega_1 \Delta i_L^Q + I_L^Q \Delta\omega_1 \\
\Delta \dot{i}_{L}^{Q} &= \frac{1}{L_L}\Delta v_L^Q - \frac{R_L}{L_L}\Delta i_L^Q - \omega_1 \Delta i_L^D - I_L^D \Delta\omega_1
\end{aligned} \tag{142}$$

It is the same parameters that need to be transformed with the virtual oscillator control as with the droop control. The linearized transformations used are therefore equal to the ones in eq. (127) and (128).

The frequency variation differs from the droop control as this is derived to be

$$\begin{aligned}
\Delta\omega_1 &= \frac{K_{i1}K_{v1}I_{o1}^D}{4C_1(v_{g1}^D)^2}\Delta v_{g1}^D - \frac{K_{i1}K_{v1}}{4C_1V_{c1}^D}\Delta i_{o1}^D \\
\Delta\omega_2 &= \frac{K_{i2}K_{v2}I_{o2}^d}{4C_2(v_{g2}^d)^2}\Delta v_{g2}^d - \frac{K_{i2}K_{v2}}{4C_2V_{c2}^d}\Delta i_{o2}^d
\end{aligned} \tag{143}$$

Inserting this for the frequency variation in the linearized state equations and also substituting for the load voltage in eq. (115), enables the system to be represented as

$$\boldsymbol{\Delta}\dot{\mathbf{x}} = \mathbf{A}\boldsymbol{\Delta}\mathbf{x} + \mathbf{B}\boldsymbol{\Delta}\mathbf{u} \tag{144}$$

In order to simplify the notation, the following convenient constants are defined

$$\begin{gathered}
F_1 = \frac{1}{2C_1}\left(\sigma_1 - \frac{3\alpha_1(v_{g1}^D)^2}{2K_{v1}^2}\right) \quad F_2 = \frac{1}{2C_2}\left(\sigma_2 - \frac{3\alpha_2(v_{g2}^d)^2}{2K_{v2}^2}\right) \quad G_1 = \frac{K_{i1}K_{v1}}{4C_1} \quad G_2 = \frac{K_{i2}K_{v2}}{4C_2} \\
M_1 = \frac{K_{i1}K_{v1}}{4C_1V_{c1}^D} \quad M_2 = \frac{K_{i2}K_{v2}}{4C_2V_{c2}^d} \quad N_1 = \frac{K_{i1}K_{v1}I_{o1}^D}{4C_1(v_{g1}^D)^2} \quad N_2 = \frac{K_{i2}K_{v2}I_{o2}^d}{4C_2(v_{g2}^d)^2}
\end{gathered} \tag{145}$$

The resulting state-space matrices are then

$$\mathbf{A} = \begin{bmatrix} F_1 & 0 & G_1 & 0 & 0 & 0 & 0 & 0 & 0 \\ \frac{1}{L_{o1}}+N_1 I_{o1}^Q & -\frac{R_{o1}+R_n}{L_{o1}}-M_1 I_{o1}^Q & \omega_1 & 0 & 0 & -\frac{R_n}{L_{o1}} & 0 & \frac{R_n}{L_{o1}} & 0 \\ -N_1 I_{o1}^D & M_1-\omega_1 & -\frac{R_{o1}+R_n}{L_{o1}} & 0 & 0 & -\frac{R_n}{L_{o1}} & 0 & \frac{R_n}{L_{o1}} & \\ -N_1 & M_1 & 0 & -M_2 I_{o2}^Q & N_2 & -M_2 & -M_2\delta_{21}^* & 0 & 0 \\ 0 & 0 & 0 & -G_2 I_{o2}^D & F_2 & -G_2\delta_{21}^* & G_2 & 0 & 0 \\ N_1 I_{o2}^Q & -\frac{R_n}{L_{o2}}-M_1 I_{o2}^Q & 0 & -\frac{v_{g2}^q}{L_{o2}} & \frac{1}{L_{o2}} & -\frac{R_{o2}+R_n}{L_{o2}} & \omega_1 & \frac{R_n}{L_{o2}} & 0 \\ \frac{\delta_{21}^*}{L_{o2}}-N_1 I_{o2}^D & M_1 I_{o2}^D & -\frac{R_n}{L_{o2}} & \frac{V_{g2}^d}{L_{o2}} & \frac{\delta_{21}^*}{L_{o2}} & -\omega_1 & -\frac{R_{o2}+R_n}{L_{o2}} & 0 & \frac{R_n}{L_{o2}} \\ N_1 I_L^Q & \frac{R_n}{L_L}-M_1 I_L^Q & 0 & 0 & 0 & \frac{R_n}{L_L} & 0 & -\frac{R_L+R_n}{L_L} & \omega_1 \\ N_1 I_L^D & M_1 I_L^D & \frac{R_n}{L_L} & 0 & 0 & 0 & \frac{R_n}{L_L} & -\omega_1 & -\frac{R_L+R_n}{L_L} \end{bmatrix} \tag{146}$$

$$\mathbf{B} = \begin{bmatrix} 0 & 0 \\ \frac{R_n}{L_{o1}} & 0 \\ 0 & \frac{R_n}{L_{o1}} \\ 0 & 0 \\ 0 & 0 \\ \frac{R_n}{L_{o2}} & 0 \\ 0 & \frac{R_n}{L_{o2}} \\ -\frac{R_n}{L_L} & 0 \\ 0 & -\frac{R_n}{L_L} \end{bmatrix} \tag{147}$$

7 Results

7.1 Verifying the state space representation

After making the state space representation, the model is tested and compared with the time-step simulation model in Simulink. The responses of the state space model and the model in Simulink should be the same when exposed to the same disturbance. To verify the equivalency, simulations in Simulink are made by increasing the load with 3.2 kW after steady state is obtained. The response in the output current from both inverters are then compared with the response in the state space model.

The results with the droop control method are shown in fig. 15 and 16. Here it can be seen that the d-axis currents make a jump from its starting point immediately after the load is increased. This discontinuous behavior is shown in both models. The q-axis currents show a different response where they follow a continuous trajectory until steady-state is reached. Both models show this response and they indicate the same settling time. Because of the harmonics present in the simulation model, the currents show a noisy response with oscillations on top of the fundamental response. However, it is clearly seen that both models show the same response which strongly supports the verification of the state space representation of the droop controlled inverters.

The virtual oscillator control is applied with the same test scenario as with the droop control. After steady-state is reached, a load increase of 3.2 kW is abruptly introduced. The responses are shown in fig. 17 and 18. Also here, the d-axis currents make an instant increase out of both inverters whilst i_{o1}^Q and i_{o2}^Q show a smoother response. It is less clear from the plots with the virtual oscillator control that the state space and the time-step simulation model are equivalent since there is only a small change in the q-axis current. But, overall the responses show the same characteristics with both state space and Simulink. This supports the verification and both the droop and the virtual oscillator state space representations can safely be assumed to be correct.

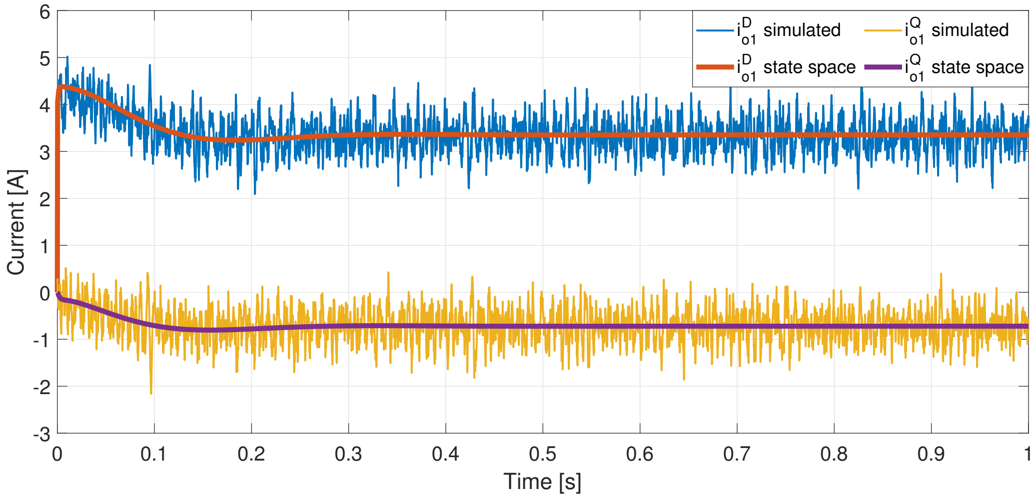

Figure 15: Droop control: Step response of load increase by 3.2 kW

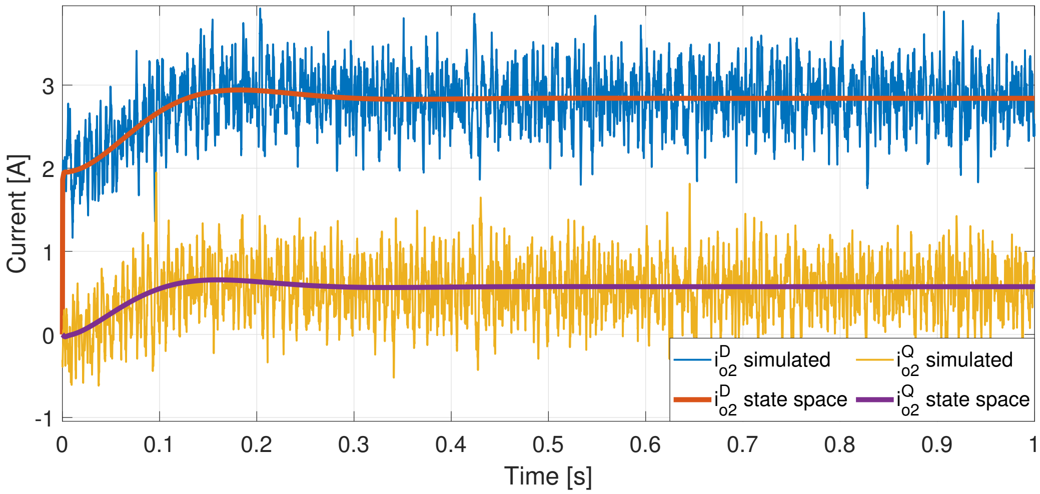

Figure 16: Droop control: Step response of load increase by 3.2 kW

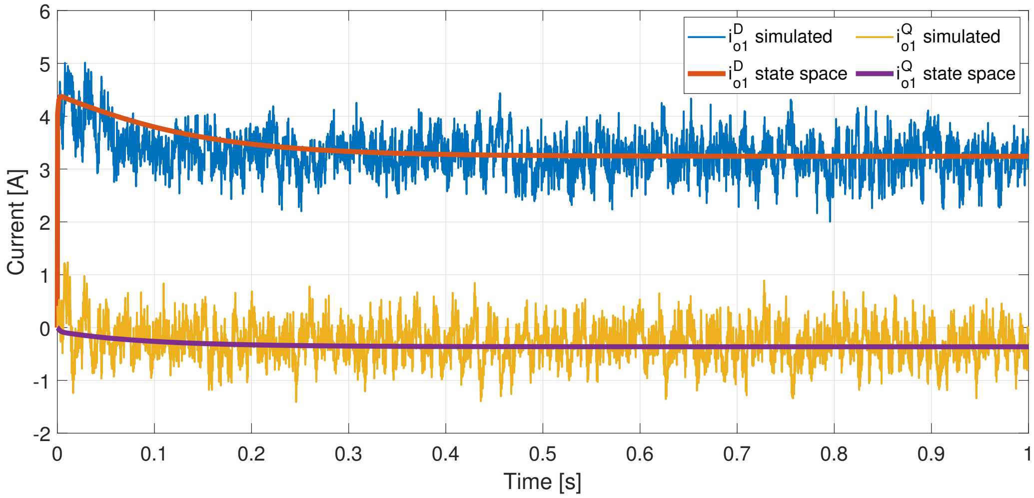

Figure 17: Virtual oscillator control: Step response of load increase by 3.2 kW

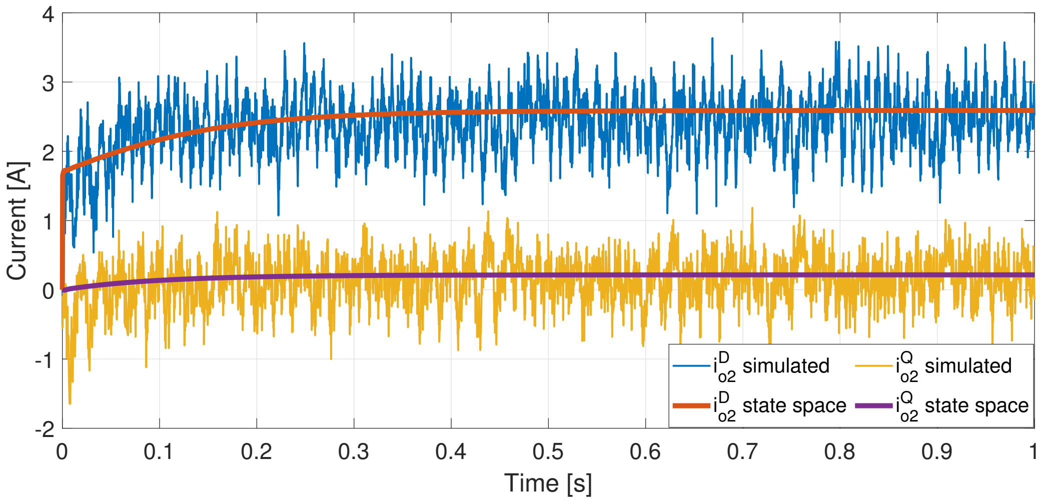

Figure 18: Virtual oscillator control: Step response of load increase by 3.2 kW

7.2 Comparing virtual oscillator and droop control for the base case

7.2.1 Step response

One way of comparing the two control methods is by analyzing the step response of the state space representations. This will provide the system's characteristic behavior to perturbations. The comparison is made with the base parameters set to give the same steady-state performance. To get the system's overall performance the characteristic polynomial of the state matrix, **A**, is calculated and used in the analysis. This is the polynomial which is used to obtain the eigenvalues (poles) of the system by equating it to zero. It is calculated according to eq. (148), with λ being the eigenvalues and I is the identity matrix. In this thesis poles and eigenvalues are used interchangeably as the system of interest is assumed to always be observable and reachable.

$$C(\lambda) = det(A - \lambda I) \tag{148}$$

The characteristic polynomial will be of the same order as the number of states in the state matrix. This means that the droop control will give two eigenvalues more than the virtual oscillator control.

Further information regarding the eigenvalues can be found by calculating the participation factor from the states on the eigenvalue. This way, it can be discovered which states are affecting the most dominant modes. By knowing which parameters that have the largest effect on these states it can be figured out which parameters that influence the system characteristics the most. The participation factor of state variable k on pole i is calculated in this thesis according to

$$P_i^k = |L_i^k \cdot R_i^k| \tag{149}$$

where L and R are the left and right eigenvalues of the state matrix **A**. The absolute value is used to clarify the comparison between different participation factors as these would originally be complex values. The factors are further normalized by making the sum of all the participation factors on one pole equal to 1.

The characteristic response of the system is found by applying a step to the transfer function $H(s) = 1/C(s)$. This gives the system's overall behavior. The responses for both state space representations are shown in fig. 19. Here, it can be observed that the droop control gives an underdamped system as the response involves an overshoot before settling. The virtual oscillator control yields an overdamped system where the final value is obtained without any overshoots and with a large settling time.

The settling time is set to be the time instant where the step response reaches ± 1% deviation from the final value and stays within this limit. Even though the droop controller has an oscillatory response it is nearly twice as fast as the virtual oscillator control in this case. The droop control obtained 1.01 after 0.42 seconds while the VOC used 0.66 seconds to reach 0.99. This is a significant difference which shows that the droop controller is much faster than the virtual oscillator control in this case.

The difference in the response is due to the location of the dominant poles for the two control methods. The dominant poles are the ones closest to the imaginary axis. The virtual oscillator control has, according to table 8, only real-valued dominant poles. This explains its overdamped characteristic as there are no complex eigenvalues among the dominant poles. The droop controller has both real value and complex dominant poles. The complex eigenvalues are also the ones with the shortest distance from the imaginary axis, this means that they are influencing the step response the most. That explains the underdamped characteristic of the droop controller. From the participation factors it can also be understood that the most dominant poles are affected by the voltage at the inverter for the virtual oscillator control and by the power outputs with the droop control.

Control method	Dominant poles	States and participation factor
Virtual oscillator control	$\lambda = -18.236$	$\delta_{21} : 0.74,\quad v_{g1} : 0.17$
	$\lambda = -15.166$	$v_{g2} : 0.65,\quad \delta_{21} : 0.20,\quad v_{g1} : 0.14$
	$\lambda = -9.680$	$v_{g1} : 0.83,\quad \delta_{21} : 0.13$
Droop control	$\lambda = -45.502$	$\delta_{21} : 0.48,\quad P_1 : 0.20,\quad P_2 : 0.20$
	$\lambda = -31.950$	$\delta_{21} : 0.48,\quad P_1 : 0.20,\quad P_2 : 0.20$
	$\lambda = -31.421$	$Q_1 : 0.40,\quad Q_2 : 0.36$
	$\lambda = -12.675 + j15.472$	$P_2 : 0.50,\quad P_1 : 0.45$
	$\lambda = -12.675 - j15.472$	$Q_2 : 0.50,\quad Q_1 : 0.45$

Table 8: Dominant poles with their participating states and their normalized participating factor. The other states participate with factors < 0.1 and the remaining poles have real values < -400.

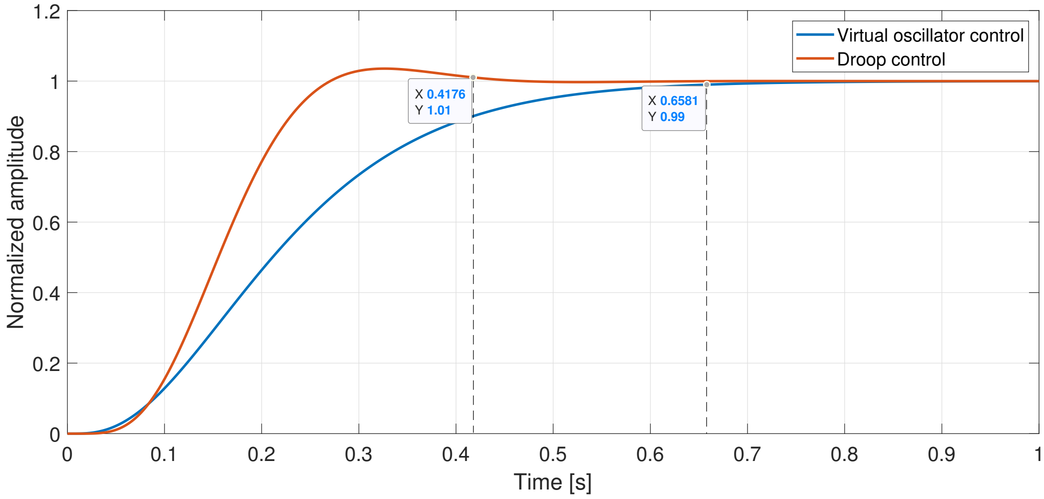

Figure 19: Step response of the state-space matrix, **A**, with both control methods. The settling time is 0.42 s for droop control and 0.66 s for virtual oscillator control.

7.2.2 Inverter control

A significant difference between the control methods becomes evident when looking at the reference voltage provided to the PWM generator on the inverter. Whereas the reference voltage with droop control in fig. 20 seems noisy, the reference voltage with virtual oscillator control is close to an ideal sinus wave. Both voltage outputs are however quite smooth and not much distorted. To be absolutely precise, the droop controlled output is in fact a bit more ideal than the output with the virtual oscillator. THD of the voltage with droop is around 1.75 % while the VOC results in a THD of 2.05 %.

The reason for the different references is due to the fact that the droop control method contains a current regulator with a bandwidth higher than the resonance frequency of the filter and the line impedance combined. This means that the current regulator is able to respond to harmonic amplification that occurs near this resonance frequency (1300 Hz). This gives the spikes in the voltage reference in order to counteract the harmonic amplification. This is also why the output voltage contains a slightly less harmonic distortion.

It should be noted that if the voltage and current controllers were not present in the system, the voltage reference with the droop control would be nearly identical to the one with virtual oscillator control. This indicates that the droop controller provides a marginally better steady state voltage output if, and only if, also the inner controllers are implemented.

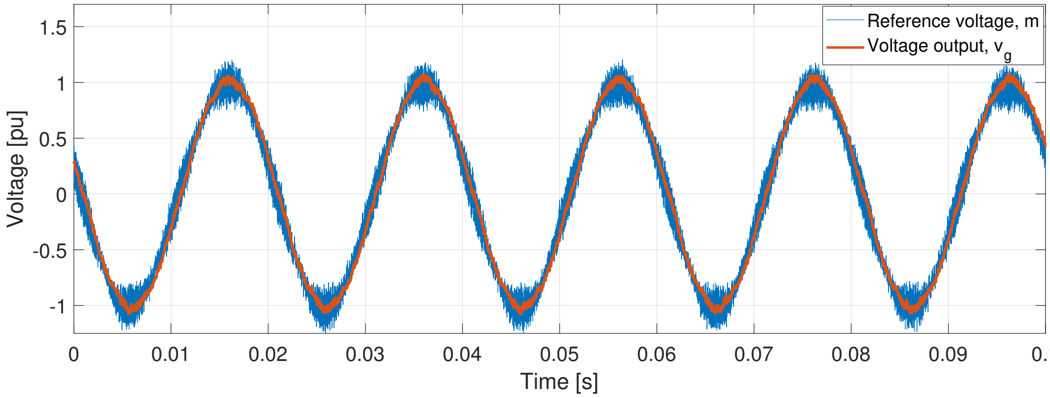

Figure 20: Droop control: Reference signal for the inverter and the voltage over the filter capacitor.

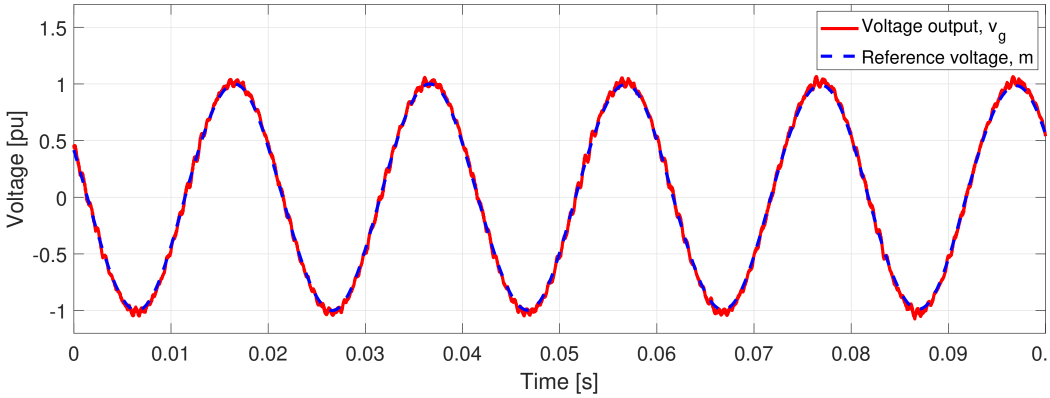

Figure 21: Virtual oscillator control: Reference signal for the inverter and the voltage over the filter capacitor.

7.2.3 Frequency and voltage control

The most important objective of the controllers is to regulate the frequency and the voltage magnitude to be within the required limits of operation. In addition, the voltage quality should also satisfy the restrictions given by the authorities. To compare the control methods, measurements of the load voltage are, for the base case with two inverters, given in table 9. In addition, a plot of the load voltages is also provided in fig. 22.

The measurements are performed with an assumed stable frequency equal to the average frequency for both methods. Since the frequency is varying, especially with the virtual oscillator control, the total harmonic distortion does not display the exact distortion level of the voltage. Furthermore, due to the frequency deviation, the unbalance factor is not absolutely precise. The deviation from the correct results are however minor for small values of ϵ and the results are reckoned to be valid, not only for comparison of the control methods but also for testing if the methods satisfy the requirements.

One clear difference between the control methods is that the distortion level in the load voltage is higher with the virtual oscillator control. It has already been shown in the previous section that a droop control with inner controllers results in a slightly cleaner voltage. Both methods are however less than half the maximum limit set by the Norwegian authorities as $\text{THD}_{max} = 5\%$.

The unbalance factor is the ratio of the negative sequence component to the positive sequence component. This is a measurement of how balanced the system is. The unbalance factor is close to identical with both control methods and both methods well below the criterion of 2%.

Control method	Load voltage	Frequency	Unbalance factor	THD
Droop control	224.5 V (RMS)	49.80 Hz	0.20 %	1.80 %
Virtual oscillator control	227.5 V (RMS)	49.76 Hz	0.24 %	2.10 %

Table 9: Voltage quality measurements with both control methods for two inverters operating the base case, i.e. a load of $16 + j4$ kVA.

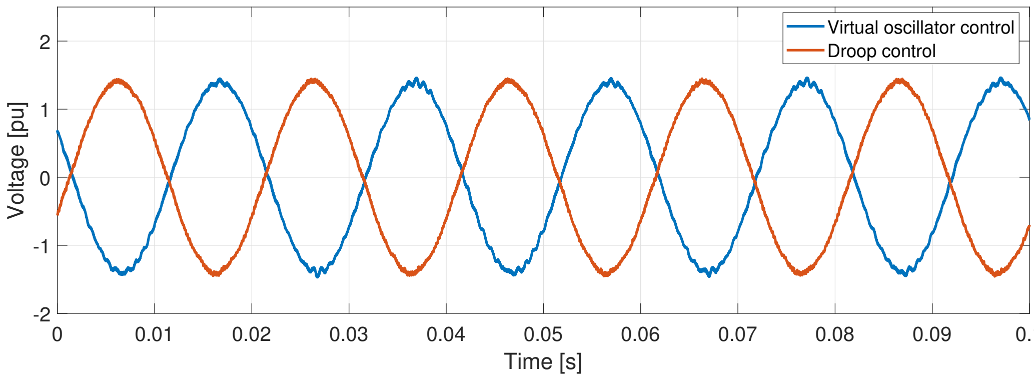

Figure 22: Load voltage at phase A in per unit with two inverters operating the base case

It should be noted that the droop method gives a lower load voltage than the VOC. This is not as expected as the power set points for the droop controller set to zero in order to match with the virtual oscillator. In turn, this should yield the same voltage with the same load. This is further investigated to see if the difference applies to all load variations. A plot of the reactive power demand versus load voltage is shown in fig. 23. To make the plot, two inverters are operated and the load is set to increase stepwise from $0 + j0$ VA to $0 + j20$ kVA. It is clear that the virtual oscillator control is higher than the droop control for the lower loads. The difference is close to 3 V in the no-load case. The decline of the VOC curve is, however, steeper and results in the methods being equivalent for the higher reactive loads. The voltage deviation between them at lower loads is not according to the expectations as both methods were set to vary between 1.05 pu and 0.95 pu, i.e. 242.5 V and 219.4 V.

To investigate why the virtual oscillator control resulted in this voltage increase at lower loads, it was compared with an average inverter model, still being controlled as a virtual oscillator. This means that the output voltage of the inverter does not contain switching harmonics, but is a pure representation of the reference voltage. This also means that the filter is no longer needed, and since a capacitor can supply reactive power and thus increase the voltage in some situations, this means one can check if the filter capacitor is the source to blame. The capacitor and the damping resistance were therefore removed in the average inverter model to test the hypothesis. The result with the average model in fig. 23 shows that the voltage is similar to the droop controller for smaller loads but at a high reactive load the voltage collapses. The voltage collapse is a result of the losses in the line increasing with increasing current and no capacitor to compensate for some of the reactive power demand. To sum up, this test shows that since the virtual oscillator does not contain a voltage regulation of the capacitor voltage, the reactive power supplied by the capacitor increases the voltage on the load more than the reduction of the current into the filter reduces the voltage reference. This gives a gross increase in load voltage when a capacitor is applied and its voltage is not controlled.

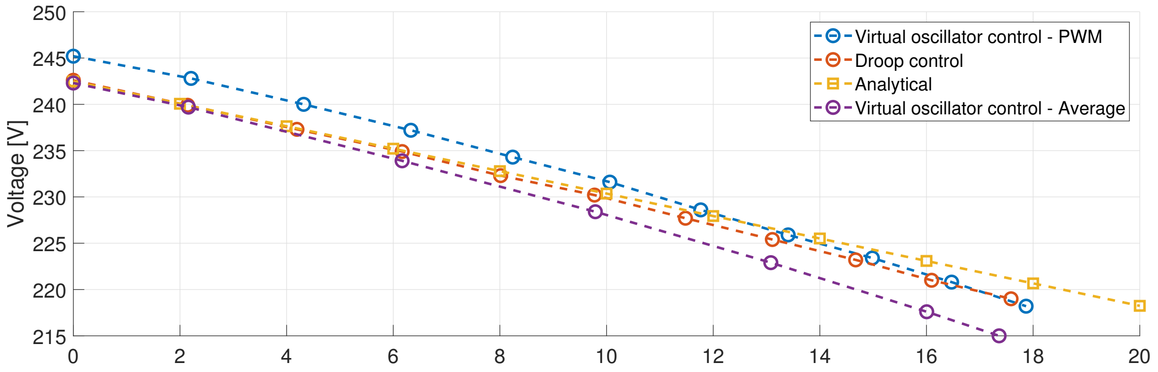

Figure 23: Voltage versus reactive power characteristic with both control methods. The analytical, i.e. the designed droop characteristic with m_q^* as in eq. (16), and the average VOC characteristic are also included.

As mentioned in section 5.2, the active and reactive power set points for the droop controller is set to zero. This will, in theory, lead to the same deviation in the frequency as with the virtual oscillator control. The base case with two inverters supplying a common load of $16 + j4$ kVA leads to almost the same frequency deviation as seen in fig. 24. The virtual oscillator control yields a lower average frequency though, and also some variations that are captured in the measurement. The reason for the varying frequency with this method is described in section 7.4. In the remaining parts of this section, the average frequency with the virtual oscillator is used.

To further analyze the frequency response over a range of loads, the frequency versus active power characteristic is made in fig. 25. Here the droop controller lies close to the linear analytical relation while the virtual oscillator control has a slightly steeper curve. The difference between the two control methods is at most 0.04 Hz which means the resemblance is strong and a clear indication that the virtual oscillator control exhibits droop laws in its control structure.

The results also show that the virtual oscillator control gives a too low frequency at the higher loads. In addition, both the droop controller and the VOC gives a voltage below the minimum requirement for rated reactive power demand. This is unsatisfactory and should be addressed in a proper tuning process of the controller parameters. Instead of adjusting all the parameters at this point, it is continued with the base case parameters in this section. This is because a tuning process for the virtual oscillator is performed for a very similar case in section 8 where an improvement of the virtual oscillator control is presented.

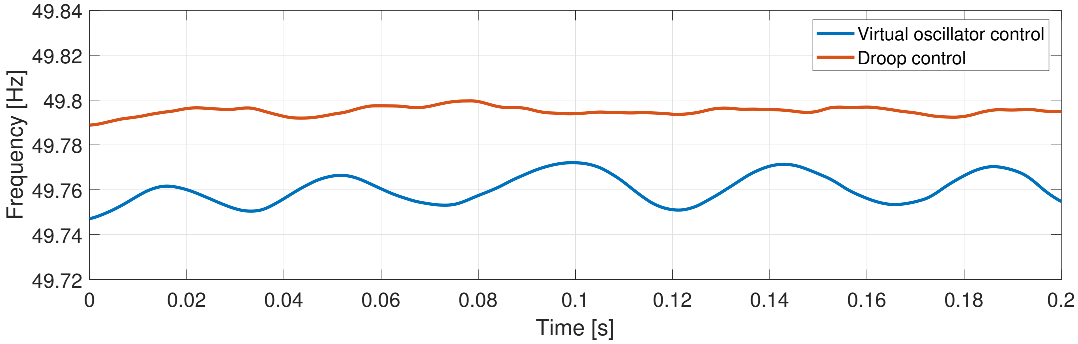

Figure 24: Measured frequency with two inverters operating the base case

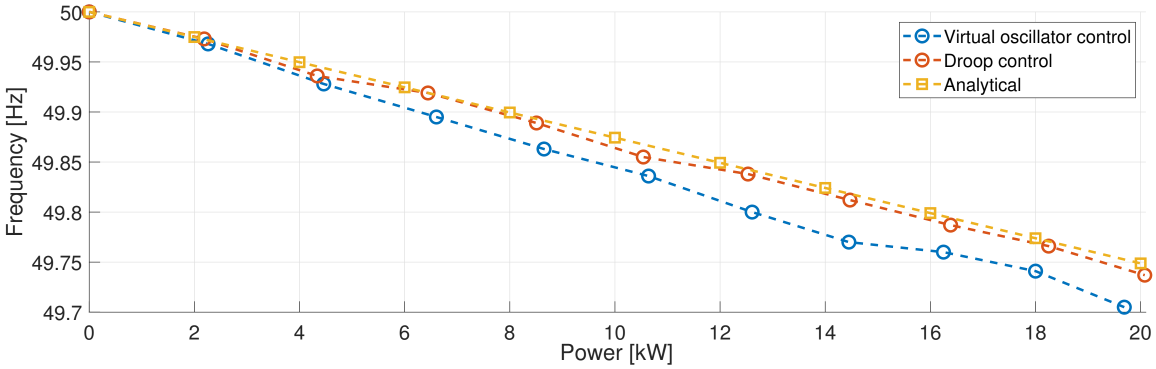

Figure 25: Frequency versus active power characteristic with both control methods. The analytical, i.e. the designed droop characteristic with n_p as in eq. (19), is also included.

7.3 Effect of change in line impedance

The droop method operates almost as if there is only one inverter in the microgrid. Since there is not a master/slave configuration, the generation units instead agree upon a voltage and frequency reference. Therefore, the stability of the system depends highly on the coupling between the units. If the presence of the second inverter becomes too strong, the system might collapse.

The coupling strength for two inverters is a function of the impedance between them and the point of common coupling. The coupling strength as defined in [18] is inverse proportional with the line impedance. This makes intuitively sense as the larger the electric distance becomes, the weaker the coupling strength becomes. The effect a reduced line impedance has on the stability is analyzed with a root locus plot in fig. 26. Here the output impedance of inverter 2 is reduced from its base value and down to a tenth of this.

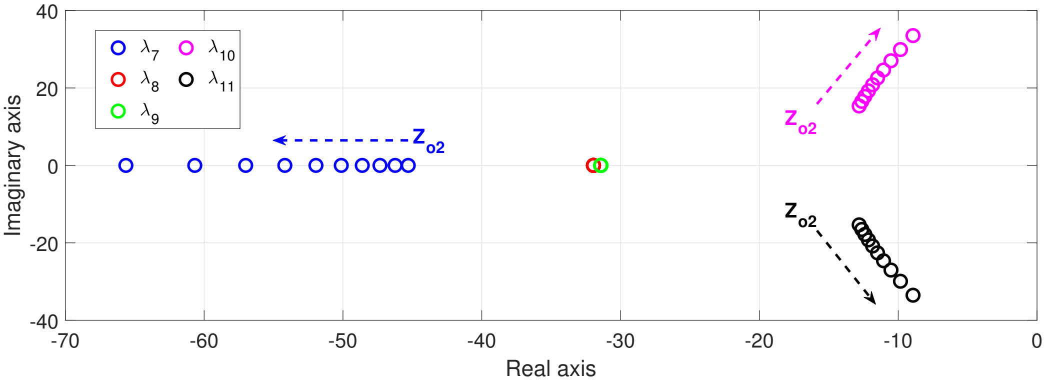

Figure 26: Droop control: Root locus plot when reducing Z_{o2} from $1.588 + j\omega 0.0039$ Ω to $0.1588 + j\omega 0.0004$ Ω

The plot includes only the dominant poles, i.e. the eigenvalues close to the origin. These poles will be most present in time plots as the other will quickly dampen out. The plot shows four clusters of eigenvalues. Each cluster contains the evolution of the concerned eigenvalue. Two clusters are on the real axis and the other two are complex conjugates of each other. The plot clearly shows that the oscillations will increase in amplitude due to the increase in the imaginary axis for the two complex eigenvalues. Also, the damping of those oscillations will reduce as the trajectory moves towards a larger real part. The reduced damping is compensated a bit by the reduced real value of one of the poles. This indicates a steeper initial response to changes. The last cluster of poles is not affected by the impedance change.

The trajectory of the complex eigenvalues will continue to move towards the real axis for a reduced impedance and when the coupling strength becomes too large the system will be unstable. This is better visualized in the step response plot in fig. 28 and 29. Here the response is initially faster and includes larger oscillations compared with the base case scenario. This results in increased settling time. When also reducing the line impedance from inverter 1, the system is no longer stable and the response never settles.

The virtual oscillator control method does not depend on the coupling strength in the same way as with the droop control. The oscillators will instead benefit from a tighter connection. The root locus plot of the dominant poles with the same variation of line impedance is shown in fig. 27. Here there are three clusters of eigenvalues. The eigenvalue with the initial smallest real part is a bit increased and goes from approximately -18 to -15.5. This becomes the most dominant pole after the two rightmost poles eventually becomes complex conjugates. This is indicated with the arrows showing that the eigenvalues first coincide and then develops an imaginary part. The complex conjugate clusters show a tendency to increase both the oscillations and the damping. This means that the inverters will have a faster response to the perturbations with a reduced impedance, but only to a certain extent as the most dominant pole is purely reactive and close to unaffected for the smaller line impedances.

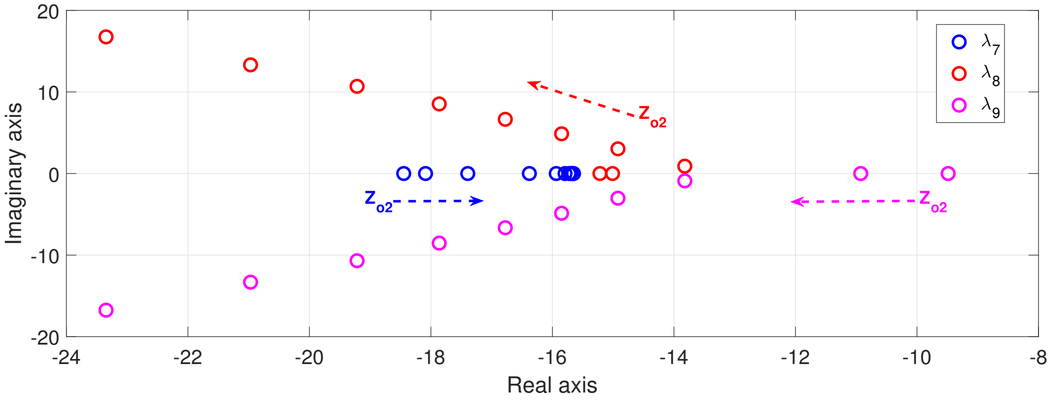

Figure 27: Virtual oscillator control: Root locus plot when reducing Z_{o2} from $1.588 + j\omega 0.0039\ \Omega$ to $0.1588 + j\omega 0.0004\ \Omega$

The step response is shown for the reduced impedance out of inverter 2 in fig. 28 and with both impedances reduced in fig. 29. The virtual oscillator controlled system is still underdamped with the stronger coupling between the inverters, but the settling time is lower. With both impedances reduced, the damping is close to critical and the settling time is down to 0.306 seconds. A solid reduction from before, more than halving the settling time from the base case scenario. With these output impedances, the virtual oscillator control stabilizes faster than the droop controller did with the initial step response of the base case in fig. 19.

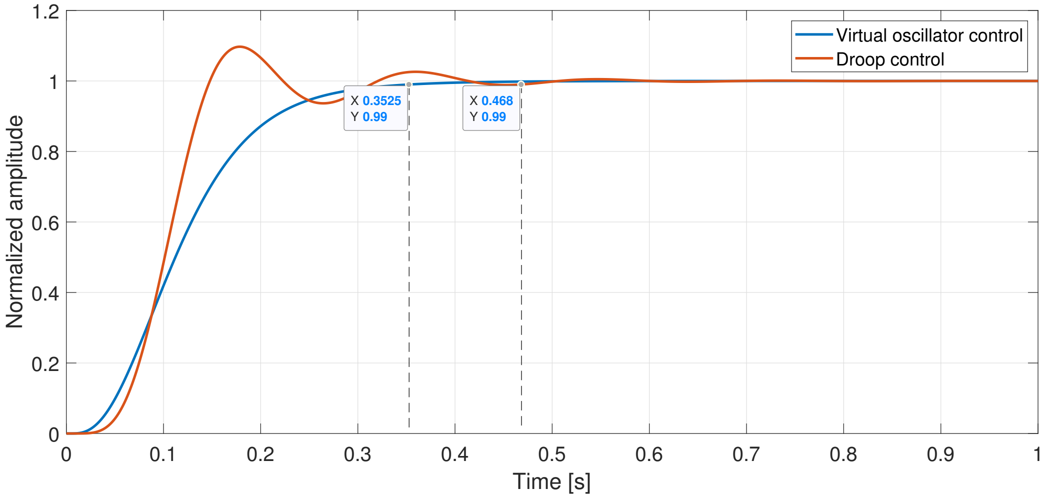

Figure 28: Overall step response of the state-space matrix, $\mathbf{A}$, with reduced $Z_{o2} = 0.1588 + j\omega 0.0004\ \Omega$, i.e. one-tenth of the base value.

These results clearly show that the virtual oscillator control is more robust in a system topology where the impedances between the inverters are small. With the parameter settings for this simulation, the VOC

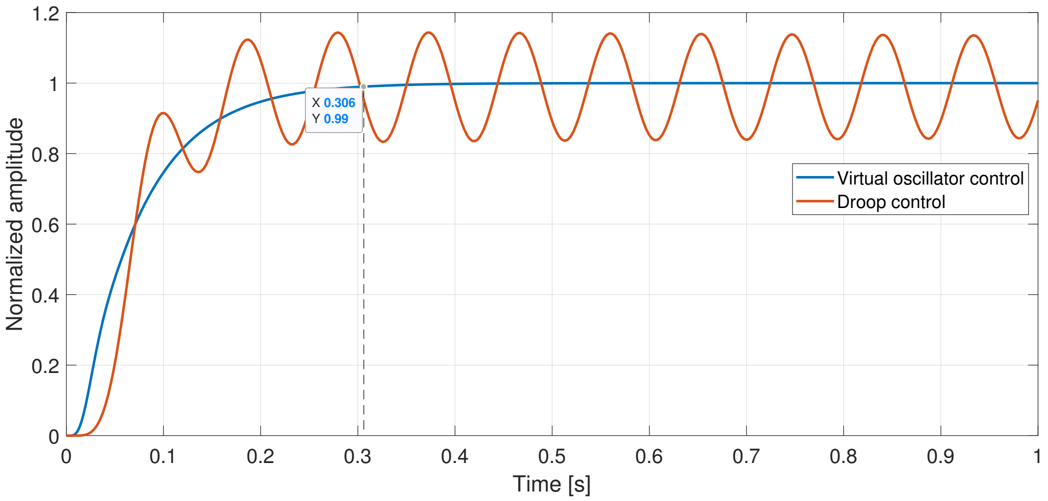

Figure 29: Overall step response of the state-space matrix, $\mathbf{A}$, with reduced $Z_{o1} = Z_{o2} = 0.1588 + j\omega 0.0004$ Ω, i.e. one fifth and one-tenth of their base value. The settling time is 0.30 s for the virtual oscillator control.

respond faster than the droop control method, and it seems to be stable for even the shortest transmission lines. This is a very important advantage with the virtual oscillator.

7.4 Effect of varying ϵ and σ in the virtual oscillator

The Van der Pol virtual oscillator is mainly characterized by two parameters. ϵ and σ. The values of these two determine the shape of the oscillations. Implicitly, also the frequency of the oscillations will be embedded in ϵ. This can be derived from the equation for the Van der Pol oscillator which is here repeated for readiness.

$$\ddot{v_C} - \epsilon\sigma\left(1 - 2v_C^2\right)\dot{v_C} + v_C = -\epsilon K_i \dot{i} \tag{150}$$

This equation is a result of differentiating eq. (50) and the variables are as presented before and shown in fig. 7.

In order to visualize the impact of the product $\epsilon \cdot \sigma$, a limit cycle for the oscillator is given in fig. 30. The derivation of this limit cycle is described in section 12.1 and the key element to notice is the circularity of the plot for different values of $\epsilon \cdot \sigma$. The more circular the trajectory is, the closer to an ideal sinus wave will the oscillations become. Here the variation of the product by multiplying and diving by an arbitrary value of 5 is shown and it is evident that for the large increase the limit cycle is no longer a circle. This will result in a deteriorated sinusoidal behavior which will give a heavily distorted voltage output of the inverter. For the reduction of the product, there is not a big difference, meaning that there is not much to gain on a reduction of ϵ or σ from the base values. This is because the degree of "sinusoidality" is only slightly improved, i.e. the circularity and thus the reduction of the distortion of the voltage will be close to negligible. At the same time, the oscillator will respond significantly slower to disturbances with a small ϵ or σ. This will be demonstrated in the following sections. In order to further investigate how the virtual oscillator control depends on ϵ and σ, the variation of both of them are independently considered in the next part of the thesis.

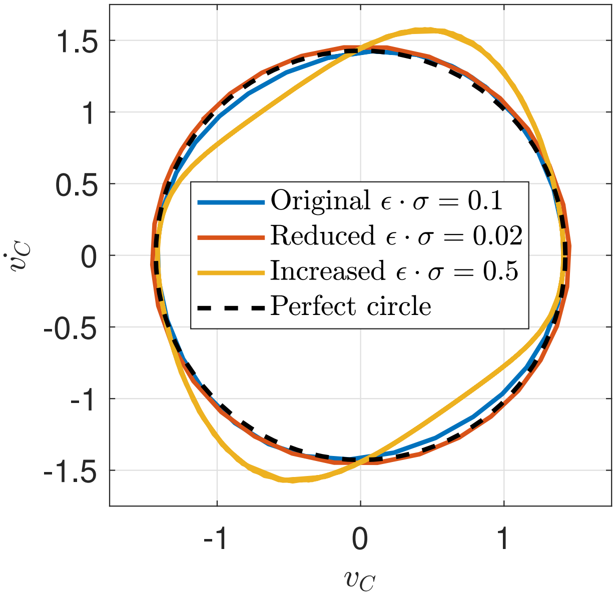

Figure 30: Limit cycles for different configurations of the virtual oscillator.

7.4.1 Influence of ϵ on the virtual oscillator

As can be understood from the derivation of the virtual oscillator dynamics, the parameter ϵ is of major influence. It is assumed to be small in order to derive the averaged dynamics of the controller and it is also directly linked with the frequency oscillations mentioned before and shown for the frequency measurement in fig. 24. This frequency measurement is not able to detect the instantaneous behavior of the oscillator and therefore not able to show the fast oscillations in the frequency. There will, in fact, be a first and third harmonic component present in the frequency as a result of the nonlinear characteristic of the Van der Pol oscillator. The reason for this is as follows.

The instantaneous frequency is defined as the derivative of the phase angle with respect to time [3]

$$f_{ins} = \frac{1}{2\pi}\frac{d\phi(t)}{dt} \tag{151}$$

This equation is close to the derivative of the instantaneous phase angle with respect to τ in eq. (58). By changing to the regular time frame and applying the definition of the instantaneous frequency gives the virtual oscillator frequency

$$f_{ins,VOC} = f^* \left[1 - \frac{\epsilon}{V}\left(\sigma V cos(\phi) - \frac{2\alpha}{K_v^2}V^3 cos^3(\phi) - \frac{K_i K_v i}{\sqrt{2}}\right) sin(\phi)\right] \tag{152}$$

where f^* is the nominal frequency, i.e. 50 Hz.

It can be seen that ϵ heavily influences how large the oscillations in frequency will be since the deviation from the nominal frequency is proportional with the value of ϵ. Ideally, its value should be zero which would result in a frequency exactly equal to the nominal one. However, this would no longer be a Van der Pol oscillator and the inverters would not properly synchronize as the varying positive and negative damping effect in the oscillators vanishes.

As a method of visualizing the frequency deviation for a varying ϵ, fig. 31 show how the instantaneous frequency varies for a larger and smaller ϵ than the base case. The plot is made with an RMS voltage $V = 240.06$ V and a current out of the inverter $i = \sqrt{2} \cdot 12.80 cos(\omega^* t + 1.38)$ A taken from simulations of the base case scenario. The increased ϵ gives large variations of the frequency while the other two values of ϵ give a more stable frequency. This behavior makes it difficult to examine the distortion of the virtual oscillator controlled voltage output with traditional tools. For instance does the total harmonic distortion rely on a fixed fundamental frequency in order to calculate the distortion factor. This will cause some errors in the measurement if the frequency is far from stable. It should be noted that this characteristic is not possible to measure directly in the simulation model due to the switching harmonics from the inverters. This is also why the frequency measurement in fig. 24 shows a completely different view because that measurement includes a low pass filter to remove high order harmonics.

Similar information on the tightness of the frequency control in the virtual oscillator can also be drawn from how the amplification factor in the RLC-parallel varies as a function of frequency. The slope of this factor near the resonance frequency (recall that the relation between L and C was set to obtain a resonance frequency of 50 Hz) determines how tightly the frequency is controlled. In fig. 32, three cases are shown. The original is made with the base case values and the reduced and increased ones with the same change as before. This RLC-parallel is working as a notch filter and the width of the filter determines how large deviations there will be in the frequency components. It is evident that the increased ϵ does not have a steep slope near 50 Hz and thus will result in larger frequency variations than in the base case. It is difficult to see form this figure how beneficial the reduction of ϵ is other than it will to some extent have a less oscillating frequency. But it is clear that a small ϵ is favored.

The reason why the value of ϵ is not set as small as possible, is that the time before the oscillator is able to respond and recover from disturbances increases when the virtual oscillator approaches a purely sinusoidal oscillator with $\epsilon = 0$. The longer settling time is a result of the dominant poles moving towards the origin for a reduction in ϵ. The root locus plot in fig. 33 shows that while the increase in ϵ gives a large increase in

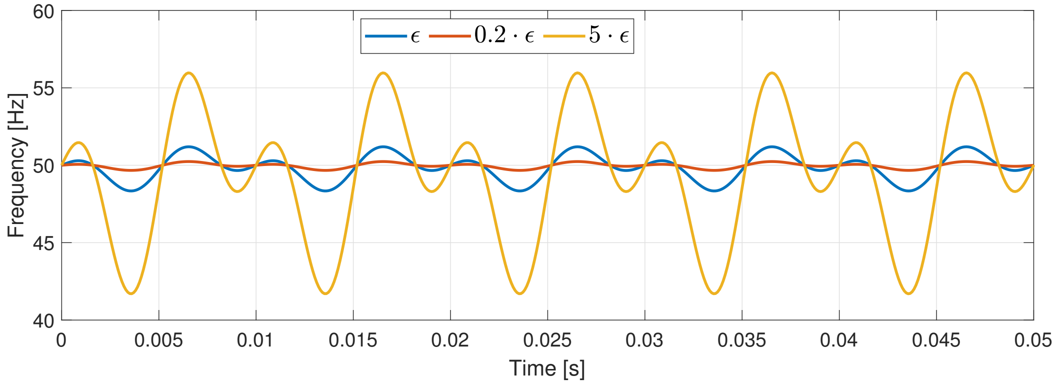

Figure 31: Visualization of the analytical instantaneous frequency in eq. (152) for the base case with $\epsilon = 0.011$ and variations of ϵ.

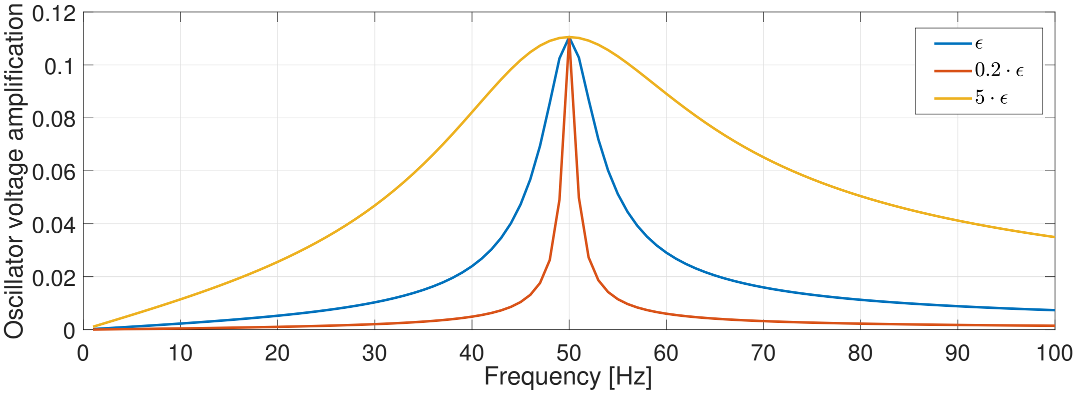

Figure 32: Voltage amplification of the oscillator voltage, v_C, as a function of frequency for different values of $\epsilon = \sqrt{\frac{L}{C}}$

damping, the reduction makes the eigenvalues in the plot move over 50 % of the distance to the origin. This gives a settling time of more than 3 seconds! Such long response times are not acceptable in this context as the virtual oscillator should be in the same range (or faster) than the droop control.

Therefore, it can be concluded that a small value is beneficial to obtain a sinusoidal waveform, but not too small as the response time of the system would increase substantially. If a perfect sinus wave is favored, the droop controller will be beneficial because it effectively operates with $\epsilon = 0$, and instead uses droop relations to synchronize the inverters.

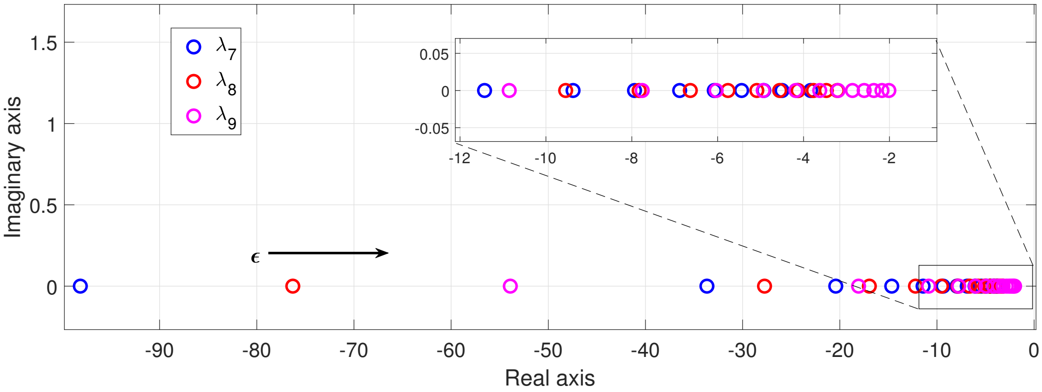

Figure 33: Root locus plot when varying ϵ from 55.53×10^{-3} to 2.22×10^{-3}. The horizontal arrow indicate the trajectory for the three eigenvalues when ϵ is reduced. The base case eigenvalues can be found in table 8.

7.4.2 Influence of σ on the virtual oscillator

The parameter σ, i.e. the oscillator conductance, is also a key parameter for the behavior of the virtual oscillator. Since the resistance in the RLC-parallel is defined as $R = -1/\sigma$, the peak value of the amplification factor will depend upon the choice of σ. Further, it will also have an impact on the current input to the RLC-parallel as the voltage-dependent current source denoted i_g in fig. 7 is scaled by $\alpha = 2\sigma/3$. These two effects will to some extent counteract each other when σ varies and, therefore, it is a bit misleading to only look at fig. 34 where the oscillator magnitude seems to increase substantially for a reduced σ. One must remember that the current into the resistor is also reduced for an increased σ which makes the net effect quite small.

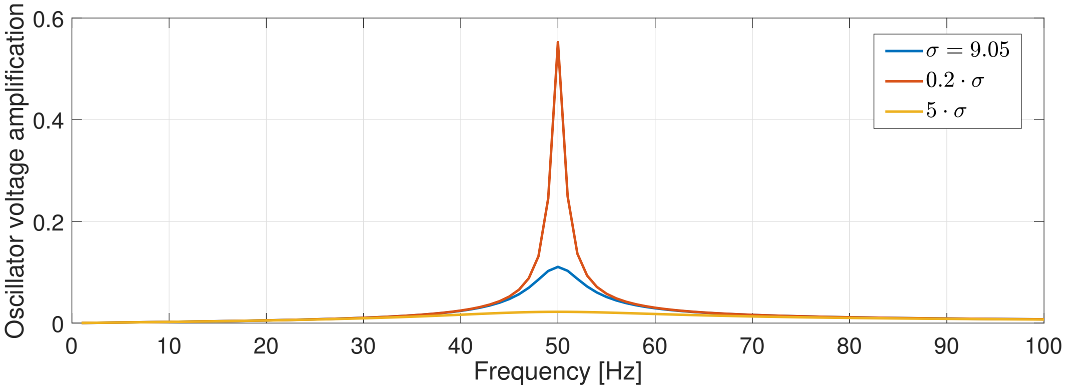

Figure 34: Voltage amplification factor of the oscillator voltage, v_C, as a function of frequency for different values of $\sigma = -1/R$.

To investigate whether a change in σ could be beneficial in some cases for the virtual oscillator control, a root locus plot is provided in fig. 35. Here there are two big differences compared with the similar variation of ϵ. First, the most dominant pole (λ_9) moves away from the origin for a reducing σ. This is indicated with the pink arrow in the plot. Such a feature might be beneficial because of the increased damping of this dominant pole. Secondly, after the σ has been reduced to 80% of the base value, λ_8 and λ_9 coincide and becomes complex conjugates of each other. At this stage, λ_7 is the most dominant pole and the overall damping is quite much reduced compared with the starting point. Now there will also be some oscillations in the step response from the virtual oscillator control.

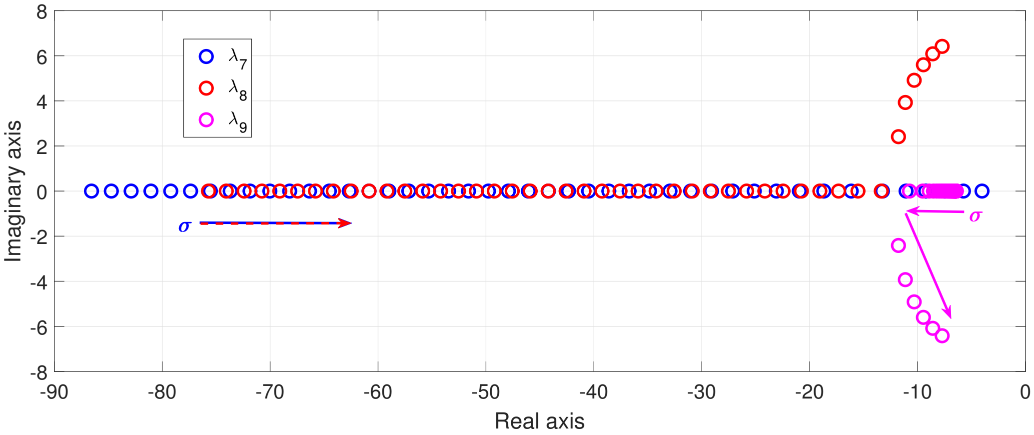

Figure 35: Root locus plot when varying σ from 45.24 to 2.24. Two poles coincide and become complex conjugates when $\sigma < 7.9885$. The different colored markers and arrows show the trajectory of each eigenvalue when σ is reduced. The base case eigenvalues can be found in table 8.

7.4.3 Influence of $\epsilon \cdot \sigma$ on the virtual oscillator

The value of $\epsilon \cdot \sigma$ dictates the shape of the oscillations. As shown in fig. 30, the smaller the value, the closer to an ideal sinus waveform will the oscillations become. This is also visualized with simulations in fig. 36 where the oscillator capacitor voltage, v_C, and the output voltage, v_g, are included for a varying $\epsilon \cdot \sigma$. In this figure, the oscillator voltage is clearly more distorted with the increased product, while the output voltage seems less affected. This is also indicated by the total harmonic distortion in table 10. Furthermore, the voltage output does not significantly improve with the reduction of $\epsilon \cdot \sigma$ while the oscillator voltage approaches an ideal sinus wave. This is quite interesting results. The reason why the output voltage can't improve beyond a THD of 2% is because of the switching process in the inverter which results in harmonics being present in the voltage. But, the reason why the THD is suddenly lower for the voltage output than for the oscillator voltage with the increased $\epsilon \cdot \sigma$ is a bit different. The reason is that the inductor current, i_L, which is used as one of the components in the Clarke Transformation to obtain the voltage reference for the inverter is not behaving as a Van der Pol oscillator. It is instead described as

$$i_L(t) = \frac{1}{L}\int_0^t v_C(s)ds + i_L(0) \tag{153}$$

or

$$\frac{\partial^2 i_L}{\partial \tau^2} - \sigma \left(1 - \frac{2}{3}(\frac{\partial i_L}{\partial \tau})^2\right) \frac{\partial i_L}{\partial \tau} + i_L = -K_i i \tag{154}$$

which differs from the Van der Pol equation that was found for the oscillator voltage. The dynamics of the current is located in these equations and it could be of interest to further analyze how the oscillator parameters influence the characteristics. It is however not investigated further in this thesis and mainly presented here as a possible field for further research. Instead, the possible benefits for reducing or increasing the value of $\epsilon \cdot \sigma$ are looked into.

$\epsilon \cdot \sigma$	v_g : THD [%]	v_C : THD [%]
0.1	2.1	1.2
0.02	2.0	0.3
0.5	4.5	6.15

Table 10: Total harmonic distortion for the voltage output, v_g, and the oscillator voltage, v_C, for different values of ϵ.

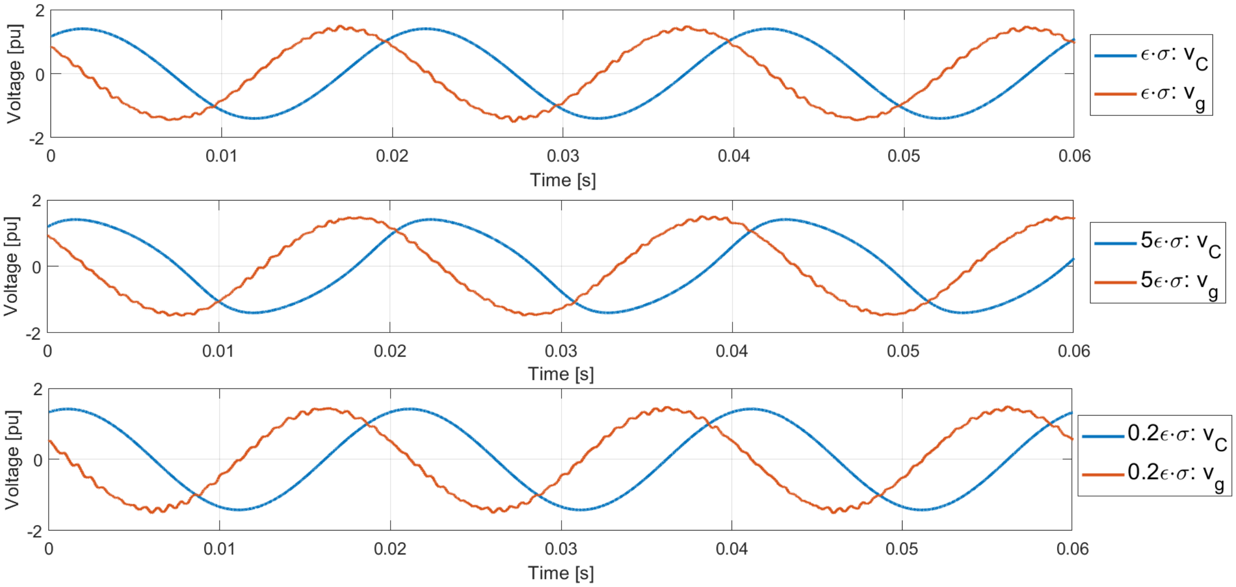

Figure 36: Oscillator voltage, v_C, and output voltage, v_g, for the base case with $\epsilon \cdot \sigma = 0.1$ and variations of $\epsilon \cdot \sigma$.

7.4.4 Simulations of variations with both σ and ϵ

In order to derive if there could be an improvement of the virtual oscillator control by either reducing or increasing σ and/or ϵ, time-step simulations are made in Simulink. The base case scenario with two inverters in operation is simulated and stepwise changes in ϵ and σ are in turn applied to the system. The results are shown in fig. 42 - 49 in the appendix. A summary of the simulation results is provided in table 11 and from this table, it is possible to draw some interesting conclusions.

The first thing to notice from the table is that the total harmonic distortion and the unbalance factor becomes saturated when the product of $\epsilon \cdot \sigma$ is reduced from the base case (marked in green). This can be seen from the waveforms in fig. 45 and fig. 49 as well as the small difference between the two orange cells regarding σ and two in magenta regarding ϵ. The improvement when either of σ or ϵ is reduced is not significant. This means that the virtual oscillator has reached its limit and the distortion level is almost as low as the droop control method was in the base case scenario. This makes sense as the droop controller gives a pure sinus wave to the voltage regulator and is regarded as an upper limit for the VOC in that sense. Furthermore, it's clear that an increase of either σ or ϵ would result in a violation of the frequency requirement while the voltage magnitude, THD and unbalance factor are within the requirements. This means that the frequency control is the limiting factor and the first constraint that becomes binding. In order to open up for a possible increase of $\epsilon \cdot \sigma$, the frequency control needs to be addressed first. Both the frequency control and the combined variation of σ and ϵ will be further developed in the next section.

σ	ϵ	**Load voltage (L-G, RMS) [pu]**	**Average Frequency [Hz]**	**THD [%]**	$\mathbf{V_-/V_+}$ **[%]**
$0.1 \cdot 9.048$	0.011	0.983	49.79	2.00	0.20
$0.5 \cdot 9.048$	0.011	0.986	49.78	2.02	0.21
9.048	0.011	0.987	49.76	2.10	0.24
$2 \cdot 9.048$	0.011	0.990	49.67	2.72	0.48
$3 \cdot 9.048$	0.011	0.995	49.50	3.52	0.64
$4 \cdot 9.048$	0.011	1.000	49.30	4.29	0.74
$5 \cdot 9.048$	0.011	1.007	49.03	5.20	0.96
9.048	$\sqrt{0.5} \cdot 0.011$	0.989	49.89	2.05	0.19
9.048	$\sqrt{0.75} \cdot 0.011$	0.987	49.83	2.07	0.19
9.048	0.011	0.987	49.76	2.10	0.24
9.048	$\sqrt{2} \cdot 0.011$	0.993	49.46	2.75	0.59
9.048	$\sqrt{3} \cdot 0.011$	0.999	49.08	3.60	0.97
9.048	$\sqrt{4} \cdot 0.011$	1.008	48.66	4.94	1.14
9.048	$\sqrt{5} \cdot 0.011$	1.019	48.18	6.38	1.90

Table 11: Results from the simulations with varying σ and ϵ. The voltage magnitude and the THD is the average of the three phase voltages. The frequency and unbalance factor, $\mathbf{V}_-/\mathbf{V}_+$, are average values as they are slightly varying in the simulations due to the frequency variation.

8 Proposing improvements of the virtual oscillator control

8.1 Utilizing the whole frequency range

During the derivation of the droop resemblance in the virtual oscillator control, the VOC was made to vary its frequency from 50 Hz to 49.75 Hz over the load range. Recall that the allowed frequency region was set to be 50 ± 0.25 Hz. This means that the controller will not be able to utilize the whole frequency range that is allowed and thus limit the parameter settings accordingly. By adjusting the maximum frequency to 50.25 Hz a larger solution space can be obtained.

In order to implement this in the controlling methods, new frequency related parameters have to be calculated. First, the new frequency droop coefficient will be

$$n_{p,new} = \frac{2\Delta_\omega \omega^*}{P_{rated}} = 3.1416 \times 10^{-4} \tag{155}$$

which corresponds to a new oscillator capacitance in the virtual oscillator

$$C_{new} = \frac{K_i}{6K_v} \frac{1}{n_{p,new}} = 143.997 \times 10^{-3} \text{ F} \tag{156}$$

In order to implement the increased frequency in the virtual oscillator controller, the resonance frequency of the RLC parallel need to be changed into the new maximum frequency. This is ensured by a new oscillator inductance given as

$$L_{new} = \frac{1}{C\omega_{max}^2} = 69.665 \times 10^{-6} \text{ H} \tag{157}$$

The increased inductance and reduced capacitance yield a doubling of $\epsilon_{new} = 2\epsilon$ without changing σ. That means that the product $\epsilon_{new} \cdot \sigma = 0.2$ is also doubled. The larger product means that the virtual oscillator will be more distorted and result in less precise control of the frequency since the oscillations will increase. This will, however, be traded off for additional damping in the system and a significantly reduced settling time for the overall system as shown in fig. 37.

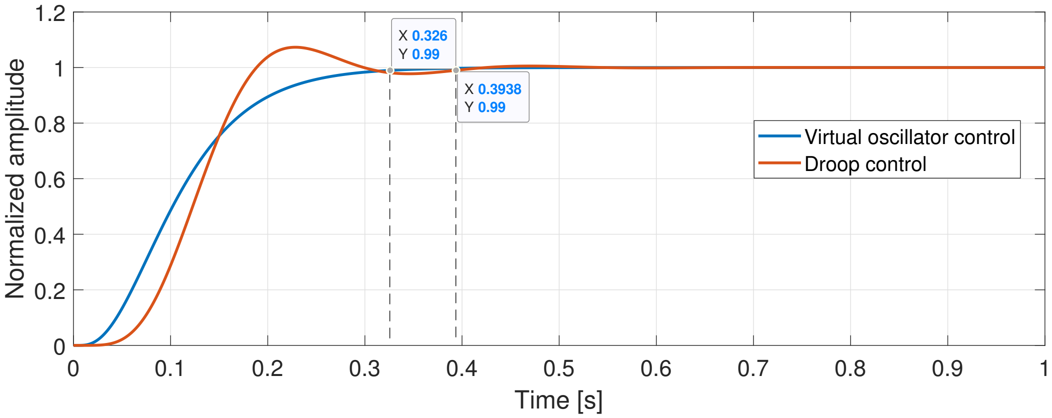

Figure 37: Step response of the overall system with the new active power droop coefficient. The settling time is in this case 0.326 s with VOC and 0.39 s with droop.

This will further result in a lower average frequency than with the tighter control that was used before. Simulations performed for the base case scenario with a load of $16 + j4$ kVA with the new ϵ and droop coefficient n_p is given in section 8.1. Here it is seen that the frequency is too low and therefore need to be dealt with in a tuning process in order to find a suitable setup for the inverters. The tuning experiment is described in the next section.

σ	ϵ	**Load voltage [pu]**	**Frequency [Hz]**	**THD [%]**	**V_-/V_+ [%]**
9.048	0.022	0.991	49.701	2.60	0.60

Table 12: Simulation results of the load voltage with the base case scenario and new active power droop coefficient.

8.2 Tuning the virtual oscillator control with the increased frequency range

With the increase of the maximum frequency and the doubling of the slope of the $f(P)$-curve as described in the previous section, the frequency for the base case with two inverters is below the minimum requirement with the virtual oscillator control. In addition, the frequency at rated active power demand will be even worse. For the record, it is noted that the droop control will lie close to the analytical relation and give a frequency of 49.74 Hz at a rated active load. The very low frequency with the new virtual oscillator means that the new parameters are not applicable. The parameters are therefore changed to give a lift in the frequency. During the tuning process it is decided to keep the voltage quality in terms of THD and unbalance factor at the same level as in section 8.1. This is ensured by keeping the product $\epsilon \cdot \sigma = 0.2$ constant.

There are two different ways the frequency can be increased for the higher loads. The first is by reducing the active power droop coefficient, i.e. reduce ϵ while at the same time increase σ. The other is to reduce σ and increase ϵ coherently. This will increase the tightness of the frequency control, i.e. make the oscillations closer to an ideal sinus wave and implicitly lift the average frequency. The last alternative will not be as efficient as the first and it is therefore decided to tune the parameters by reducing ϵ and increase σ.

In fig. 38, a simulation is performed with a reduction of γ every 0.3 seconds. This γ-factor is equivalent to how much the ϵ value is increased and at the same time how much the value of σ is decreased. The mathematical definition is given in the equation below and this factor is used to better show the variation of the parameters.

$$\gamma = \frac{\epsilon_{new}}{\epsilon} = \frac{\sigma}{\sigma_{new}} \tag{158}$$

The frequency plot in fig. 38 is made for a load at rated active power which means that when the frequency is higher than 49.75 Hz, the system will operate within the frequency requirement for every demand below the system rating. The simulation shows that for a $\gamma = 0.8$ the virtual oscillator parameters will result in a system that satisfies the limitations. With this value of γ, the optimized parameters will be as given in table 13. With these settings, the voltage level is also within the minimum requirement for a purely reactive load at the rated value. It can thus be concluded that these parameters will both keep the voltage quality at a near optimal level, close to the attainable limit of THD, and provide a system with the shortest settling time. As can be seen when comparing fig. 37 and fig. 39, the settling time is a bit increased from the initial value of ϵ and σ after the maximum frequency was set to 50.25 Hz. It is however still significantly smaller than what was the result with the base case in fig. 19. With the corresponding new droop coefficients $n_p' = \gamma \cdot n_{p,new}$ and $m_q' = m_q/\gamma$, the droop controller is now slower than in the base case, and both methods recover almost equally fast.

Name	Symbol	Value
Voltage gain	K_v	242.287
Current gain	K_i	65.818×10^{-3}
Oscillator conductance	σ	11.309 S
Current source factor	α	7.540
Oscillator capacitance	C	179.997×10^{-3} F
Oscillator inductance	L	55.732×10^{-6} H
Oscillator resistance	R	$-0.088\ \Omega$
Oscillator characterizing factor	ϵ	0.0176

Table 13: Optimal parameters for the virtual oscillator control with the increased frequency range

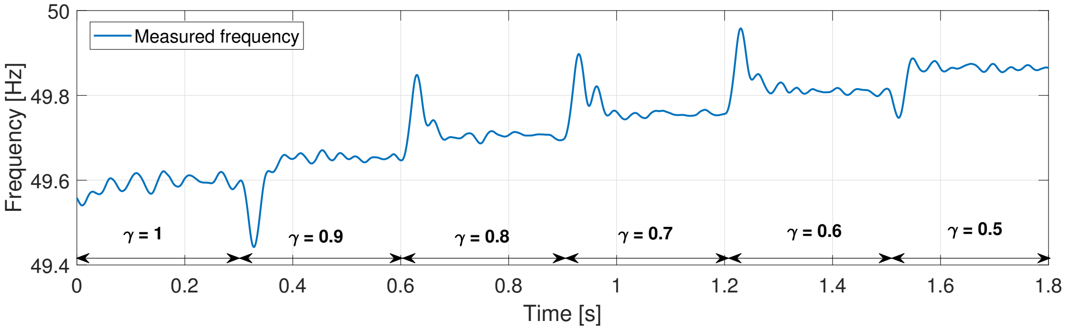

Figure 38: Simulated frequency for a reducing γ and a load of 20 kW, i.e. equal to the rated power of the two inverters.

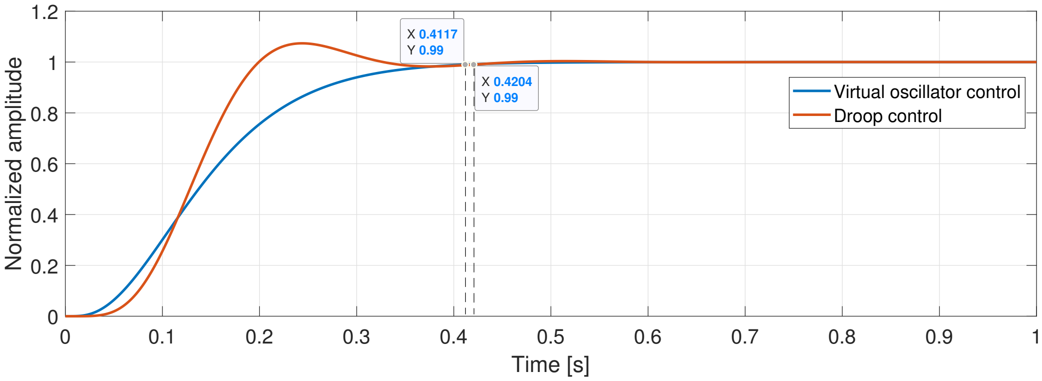

Figure 39: Step response of both virtual oscillator control and droop control with the optimal VOC parameters and the corresponding droop coefficients. The settling time for the VOC is 0.41 s and for the droop control it is 0.42 s.

8.3 Introducing frequency control

As was shortly introduced previously, the frequency was lifted by varying the resonance frequency of the virtual oscillator. By dynamically varying this resonance frequency enables the implementation of a secondary control unit similar to the one that in a real-life setup adjusts the set points in the droop controller. In order to control the frequency, the inductance, L, of the RLC-parallel can be varied. How this variable inductance is implemented is explained in section 5.4.5 and the result of this frequency control is shown in fig. 40.

The simulation is made with two inverters powering a load of $10 + j2$ kVA initially. At $t = 0.2$ s, the load is increased by 8 kW to $18 + j2$ kVA. This gives a frequency reduction from approximately 49.84 Hz down to 49.75 Hz. At $t = 0.4$ s, the inductance is reduced by a factor of 0.99, i.e. $L_{new} = 0.99L$ which means that $\epsilon_{new} = \sqrt{0.99}\epsilon$. This corresponds to a lift in the resonance frequency of 0.25 Hz and also the simulation measurement shows that the frequency is restored by 0.25 Hz.

The small variation in ϵ has a small impact on the system dynamics and the virtual oscillator almost instantly adapts to the new inductance. This opens up a way of regulating the frequency in the grid through for instance a look-up table. By associating a range of active power outputs with a given inductance factor makes the virtual oscillator control obtain a tighter frequency control. This also enables the virtual oscillator control to have a larger equivalent droop coefficient in the $P - f$ relation. In turn could this yield a

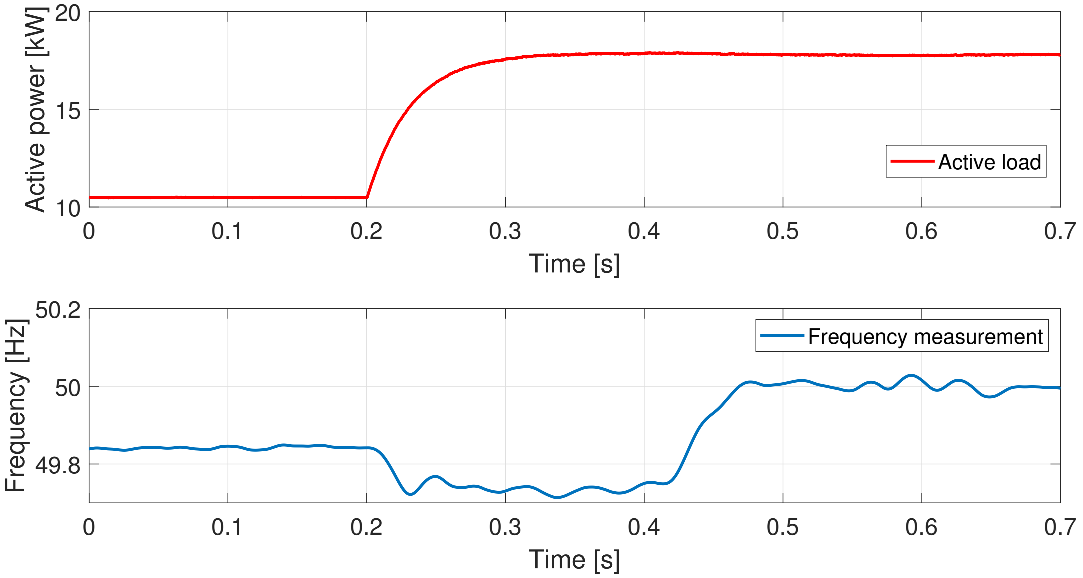

Figure 40: Result of the proposed frequency control when a load increase and a frequency lift occurs at $t = 0.2$ s and $t = 0.4$ s, respectively.

shorter settling time as the virtual oscillator would respond faster to changes with a reduced inductance and capacitance.

8.4 Introducing voltage control

As was described in section 7.4.2, the oscillator conductance, σ, is related to the voltage magnitude of the virtual oscillator and also to the $Q - V$ droop coefficient. Inspired by the control possibilities with a dynamically varying ϵ, perhaps there could also be similar possibilities for a voltage control through a varying σ?

There are two parameters that depend on σ in the virtual oscillator control. It is the oscillator resistance $R = -1/\sigma$ in the RLC-parallel, and the current amplification factor, $\alpha = 2/3\sigma$. If both are varied as σ is varied, the effect from the two are countered. I.e. the voltage increase caused by a lower R is counteracted by a voltage reduction due to an associated larger negative current input from i_g. This relation becomes obvious when looking at the control structure in fig. 7. Therefore, in order to control the voltage, only one of them is varied. Then, by choosing to vary the resistance, control of the voltage should be obtained.

To prove this, a Simulink simulation was made with two inverters initially powering a load of $12 + j4$ kVA. At $t = 0.2$ s, the load is increased to $14 + j9$ kVA. This yields a large drop in the load voltage as shown in fig. 41. The voltage drops from almost 1.02 pu and down to 0.985 pu. In order to increase the load voltage, the oscillator voltage magnitude of both inverters is increased by reducing the resistance in the oscillator as $R_{new} = 0.95R$. The increased amplification of the oscillator voltage results in a higher load voltage and, after roughly 0.1 seconds, the voltage is restored at 1.003 pu.

In the same way as with the frequency control in the previous section, it is possible to implement a lookup-table relating different reactive power output regions with a given amplification factor. This would improve the voltage control significantly. In turn, it could also reduce the overvoltage at low loads as was shown in fig. 23 to be a problem with the virtual oscillator.

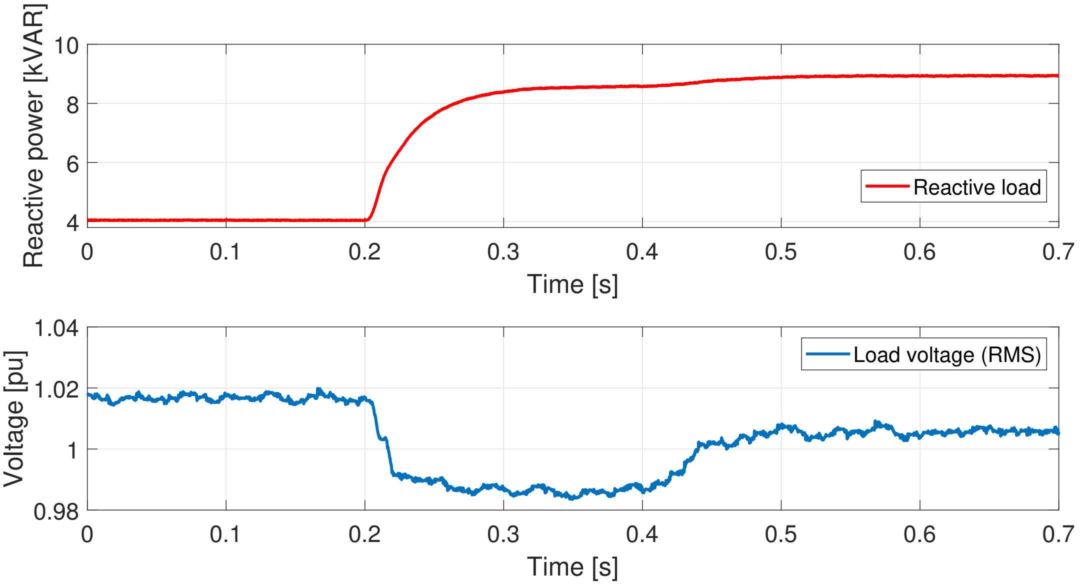

Figure 41: Reactive power demand and load voltage during the simulation of an increase in load followed by a voltage drop at $t = 0.2$ s and a voltage increase at $t = 0.4$ s.

This way of voltage control could also be obtained by varying the voltage gain, K_v, that was set to make the oscillator voltage be 1 V when the inverter was operating at rated voltage. As another development of this type of voltage control could also a PI regulator be used to give the necessary voltage gain. These further developments are not discussed in this thesis and just mentioned as possible fields of future research.

9 Overall discussion

One of the main questions to be addressed in this thesis was related to if and when the virtual oscillator control was a better alternative than the conventional droop control. This has permeated the outline for the thesis and the reason for the different topics that have been investigated. An underlying question regards how the performance of the virtual oscillator control is affected by the parameters ϵ, σ and the product of the two. Since the distortion and unbalance factor will be closely linked with the product it was decided to be of interest figuring out if and possibly which value for this product that would be optimal for the best possible control.

The initial base case comparison with two inverters supplying a common load of $16 + j4$ kVA showed that there were some differences in performance. The droop controller resulted in a lower total harmonic distortion as well as providing tighter control of the voltage and frequency. Whereas the droop controller was close to the analytically selected performance in terms of $P - f$ and $Q - V$ characteristics in fig. 25 and 23, the virtual oscillator resulted in larger deviations. The frequency with the droop controller also contained smaller oscillations as seen in fig. 24. Since the virtual oscillator control has to be defined with an ϵ-value larger than zero, it is not possible to completely avoid the frequency oscillations.

Even though these oscillations should grant a benefit in terms of faster recoveries after disturbances, the droop controller had a significantly lower settling time with the initial parameter setting. As the virtual oscillator control was set to give almost the same voltage quality as the droop controller this resulted in a system with less damping of the dominant poles. The base case setting is therefore not in favor of the virtual oscillator and the operating conditions need to change in order for the virtual oscillator to get the upper hand.

There was a clear advantage with the virtual oscillator over the droop control when it came to the lower impedance grid. The droop controller worked fine when the coupling strength between the inverters was low but quickly became sluggish and slower with the impedance reduction. The opposite relation was found for the virtual oscillator control which improved its performance when the coupling between the oscillators increased. This favors the virtual oscillator significantly and is a key factor to consider when deciding which control method that is best suited for a given grid topology. It also became clear that with strong coupling, the settling time for the VOC would be lower than for the droop controller in the initial base case. And this was without tuning of the controller.

The simulations with variations in ϵ and σ-values in table 11 showed that the voltage quality became saturated for a value of $\epsilon \cdot \sigma \approx 0.1$. Because for a lower product, the total harmonic distortion, as well as the unbalance factor and average frequency ceased to improve significantly. The upper limit for the virtual oscillator is the droop controller which provides a pure sinus reference to its voltage regulator. This means the VOC cannot improve beyond the performance of the droop controller regarding voltage quality terms for the base case scenario.

When the maximum frequency was increased and the whole frequency range was utilized, the results indicated that this was in favor of the virtual oscillator control. The settling time with the virtual oscillator improved significantly while the droop controller instead ended up with a slightly increased settling time with its equivalent parameters. The equivalent active power versus frequency coefficient for the virtual oscillator was however not acceptable as the frequency was too low for large active power demands. By tuning the values of ϵ and σ and keeping the product equal to $\epsilon \cdot \sigma = 0.2$ constant, the droop coefficient was reduced to 80% of its value. This resulted in both control methods having almost the same settling time. With this tuning will however the droop controller still outperform the virtual oscillator in terms of voltage quality if the coupling strength between the inverters is weak.

Since the droop controller regulates the voltage over the capacitor in the output filter and the virtual oscillator only uses measurements of the current into the filter, there is a clear disadvantage with the VOC when it comes to controlling the voltage output. Since the capacitor can supply reactive power, and this effect is most effective for low voltages, this results in overvoltages when the demand is low. The droop controller will, on the other hand, regulate its voltage reference at such low loads in order to counteract the reactive compensation. This increased preciseness of voltage control (and frequency control) with the droop controller is also evident in other operating conditions. A secondary controller implemented in the droop control can regulate the power setpoints in order to keep the voltage and frequency closer to the nominal values than the original virtual oscillator controller is able to.

In order to increase the precision of the virtual oscillator control, equivalent regulations were suggested. To better regulate the frequency, it was shown in fig. 40 how an online regulation of the inductance of the VOC's RLC-parallel resulted in a lift in the frequency. A similar proposal was also presented for the voltage regulation by controlling the amplification factor of the notch filter, i.e. the resistance in the RLC-parallel. In fig. 41 the load voltage was increased by online reduction of this resistance. These two proposals for improvement were mostly meant as ideas for further work and presented to give a glimpse of the capabilities. The impact on the stability for the controller with such additional regulators will then be necessary to look into.

This thesis presents clear indications on that the virtual oscillator control is more robust than the equivalent droop controller. The virtual oscillator control is functional over a wider range of grid impedances and is stable for every coupling strength that is investigated in this thesis. But, the improved robustness also results in a reduced voltage quality. The virtual oscillator cannot control the frequency and voltage magnitude as precise as the droop controller and it cannot deliver a voltage with a lower THD and unbalance factor than what the droop is capable of at the same conditions. If the virtual oscillator is forced to reduce the distortion level and approach the same quality as with the droop controller this results in a significantly reduced damping of the system and a very large settling time.

10 Conclusion

Two different communication free control methods of parallel-connected inverters in a stand-alone microgrid have been compared. The comparison have been based on two inverters delivering power to a common load. Through simulations and eigenvalue analysis have the steady-state behaviour, the transient characteristics, and the robustness of the control methods been investigated.

The droop controller is a pure sinusoidal oscillator meaning it provides a reference voltage with an ideal sinus shape and a stable frequency. The virtual oscillator control is a non-linear oscillator which result in a slightly distorted reference voltage and an oscillating instantaneous frequency. The virtual oscillator control is therefore not able to produce a voltage with as good quality as the droop controller without reducing its synchronization strength significantly.

The benefit with the virtual oscillator control is its increased robustness as it is stable for all conditions tested in this thesis. In addition, as the droop controller worsens with an increased coupling strength and eventually becomes unstable, the virtual oscillator controller improves with tighter coupling between the inverters.

It can therefore be concluded that the droop controller is the favourable choice for microgrids with high line impedances. With such a topology it has not been found sufficient reasons to choose the virtual oscillator control over the droop control. On the other hand, if the microgrid has a low impedance grid, the virtual oscillator is a better alternative.

11 Further work

In order for future research to build upon this work, the model description including parameters and Simulink models have been explicitly displayed. Several places in the thesis have proposals for further work been mentioned and explained. Some shortcomings of the model have also been stated. To sum up, a list of proposals for future research is included below.

- Improve the state-space representation of the microgrid to also include the DC side dynamics.
- Look at ways to implement the frequency and voltage control in the virtual oscillator control by for instance look-up table or a PI regulator. Comparing different alternatives will yield insight into the possibilities and shortcomings of the control method. This can further be compared with the equivalent secondary control for the droop control method.
- Take a closer look at how the inductor current i_L varies as a function of the oscillator parameters and how the three phase inverter is affected from the combination of a distorted and more ideal sinus wave in the input for the Clarke Transformation. This was unfortunately not investigated in this work due to time limitations, but is an interesting characteristic of the virtual oscillator performance.
- Extend the comparison between the control methods to include non-linear loads. Such a load scenario will be more common in the future with power electronics becoming more prominent in the electric grid.

In addition, due to the non-linearity of the virtual oscillator, such a scenario might reveal interesting differences between the controllers.

Bibliography

[1] Jens G Balchen, Trond Andresen, and Bjarne A Foss. *Reguleringsteknikk.* NTNU, Institutt for teknisk kybernetikk, 2004.

[2] Richard J Blackwell. *Christiaan Huygens' The Pendulum Clock, or, Geometrical Demonstrations Concerning the Motion of Pendula as Applied to Clocks.* Iowa State University Press, 1986.

[3] Boualem Boashash. Estimating and interpreting the instantaneous frequency of a signal. i. fundamentals. *Proceedings of the IEEE*, 80(4):520–538, 1992.

[4] Ruben Buchmann. Harmonic sharing in microgrid applications-modeling, developing and evaluating a microgrid control system with harmonic sharing capability. Master's thesis, NTNU, 2018.

[5] Brian Johnson, Miguel Rodriguez, Mohit Sinha, and Sairaj Dhople. Comparison of virtual oscillator and droop control. In *2017 IEEE 18th Workshop on Control and Modeling for Power Electronics (COMPEL)*, pages 1–6. IEEE, 2017.

[6] Brian B Johnson, Mohit Sinha, Nathan G Ainsworth, Florian Dörfler, and Sairaj V Dhople. Synthesizing virtual oscillators to control islanded inverters. *IEEE Transactions on Power Electronics*, 31(8):6002–6015, 2015.

[7] AEWH Kahlane, L Hassaine, and M Kherchi. Lcl filter design for photovoltaic grid connected systems. *the Journal of Renewable Energies*, pages 227–232, 2014.

[8] T. Kanamaru. Van der Pol oscillator. *Scholarpedia*, 2(1):2202, 2007. revision #138698.

[9] Farid Katiraei and Mohammad Reza Iravani. Power management strategies for a microgrid with multiple distributed generation units. *IEEE transactions on power systems*, 21(4):1821–1831, 2006.

[10] Hassan K Khalil and Jessy W Grizzle. *Nonlinear systems*, volume 3. Prentice hall Upper Saddle River, NJ, 2002.

[11] Fusheng Li, Ruisheng Li, and Fengquan Zhou. *Microgrid technology and engineering application.* Elsevier, 2015.

[12] Ned Mohan and Tore M Undeland. *Power electronics: converters, applications, and design.* John Wiley & Sons, 2007.

[13] Stavros Papathanassiou, Nikos Hatziargyriou, Kai Strunz, et al. A benchmark low voltage microgrid network. In *Proceedings of the CIGRE symposium: power systems with dispersed generation*, pages 1–8, 2005.

[14] Nagaraju Pogaku, Milan Prodanovic, and Timothy C Green. Modeling, analysis and testing of autonomous operation of an inverter-based microgrid. *IEEE Transactions on power electronics*, 22(2):613–625, 2007.

[15] Hadi Sadaat. *Power System Analysis.* PSA Pub., 2010.

[16] Santiago Sanchez, Gilbert Bergna, and Elisabetta Tedeschi. Tuning of control loops for grid-connected modular multilevel converters under a simplified port representation for large system studies. In *Ecological Vehicles and Renewable Energies (EVER), 2017 Twelfth International Conference on*, pages 1–8. IEEE, 2017.

[17] Zhan Shi, Hendra I Nurdin, John E Fletcher, and Jiacheng Li. Similarities between virtual oscillator controlled and droop controlled three-phase inverters. In *2018 IEEE 18th International Power Electronics and Motion Control Conference (PEMC)*, pages 434–439. IEEE, 2018.

[18] John W Simpson-Porco, Florian Dörfler, and Francesco Bullo. Droop-controlled inverters are kuramoto oscillators. *IFAC Proceedings Volumes*, 45(26):264–269, 2012.

[19] Mohit Sinha, Sairaj Dhople, Brian Johnson, Nathan Ainsworth, and Florian Dörfler. Nonlinear supersets to droop control. In *2015 IEEE 16th Workshop on Control and Modeling for Power Electronics (COMPEL)*, pages 1–6. IEEE, 2015.

[20] Mohit Sinha, Florian Dörfler, Brian B Johnson, and Sairaj V Dhople. Uncovering droop control laws embedded within the nonlinear dynamics of van der pol oscillators. *IEEE Transactions on Control of Network Systems*, 4(2):347–358, 2017.

[21] Steven Strogatz. *Sync: The emerging science of spontaneous order.* Penguin UK, 2004.

[22] Norges vassdrags-og energidirektorat. Leveringskvalitetsforskriften. `https://lovdata.no/dokument/SF/forskrift/2004-11-30-1557`, 2004.

[23] Gaurav Vijay and DK Palwalia. A novel analysis and modeling of boost and buck converter. *International Journal of Electronics, Electric al and Computational System (IJEECS)*, 6(3), 2017.

[24] John G Ziegler and Nathaniel B Nichols. Optimum settings for automatic controllers. *trans. ASME*, 64(11), 1942.

12 Appendix

12.1 Phase portrait of the Van der Pol oscillator

Differentiating $\frac{dv_C}{dt}$ in eq. (50) one more time gives

$$\frac{d^2 v_C}{dt^2} = \frac{\sigma}{C}\frac{dv_C}{dt} - \frac{3\alpha v_C^2}{C}\frac{dv_C}{dt} + \frac{1}{LC}v_C - K_i\frac{di}{dt} \tag{159}$$

substituting $\tau = \omega t$ and using $\frac{d}{d\tau} = \frac{d}{d\frac{t}{\omega}} = \omega\frac{d}{dt} = \frac{1}{LC}\frac{d}{dt}$ gives

$$\frac{d^2 v_C}{d\tau^2} = \sqrt{\frac{L}{C}}\left(\sigma - 3\alpha v_C^2\right)\frac{dv_C}{d\tau} - v_C - \sqrt{\frac{L}{C}}K_i\frac{di}{d\tau} \tag{160}$$

Moving all terms dependent on v_C to one side and inserting for ϵ

$$\frac{d^2 v_C}{d\tau^2} + \epsilon\left(3\alpha v_C^2 - \sigma\right)\frac{dv_C}{d\tau} + v_C = -\epsilon K_i\frac{di}{d\tau} \tag{161}$$

Assuming that the inverter is not loaded, i.e. the input current to the controller $i = 0$, this gives in compact form

$$\ddot{v_C} - \epsilon\sigma\left(1 - 2v_C^2\right)\dot{v_C} + v_C = 0 \tag{162}$$

This is an equation for a Van der Pol oscillator, [8], which is given as

$$\ddot{x} - \mu\left(1 - x^2\right)\dot{x} + x = 0 \tag{163}$$

where x is a dynamical variable and $\mu > 0$ a parameter.

To draw a limit cycle of the differential equation, the second order equation is first reduced to two coupled first order equations by selecting

$$x_1 = v_C,\ x_2 = \frac{dv_C}{dt} \tag{164}$$

Then

$$\dot{x_1} = x_2 \tag{165}$$

$$\dot{x_2} = -x_1 - \epsilon\sigma\left(1 - \frac{3\alpha}{\sigma}x_1^2\right)x_2 \tag{166}$$

Solving these differential equations numerically yields the time evolution for the two variables. Plotting the two variables versus each other results in a phase plot.

12.2 Simulations of varying ϵ and σ

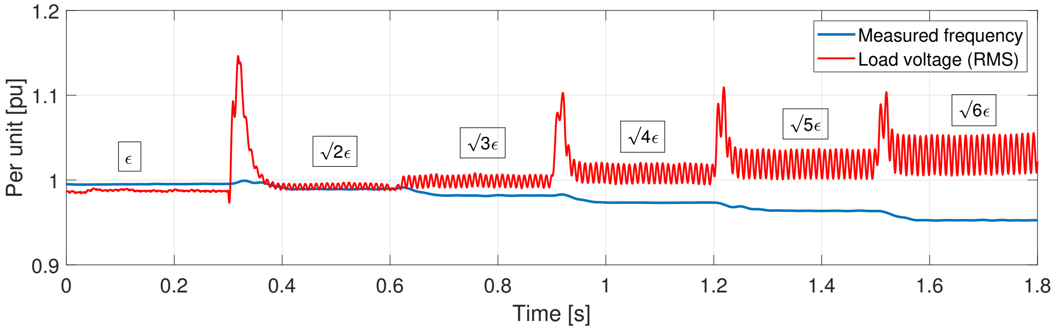

Figure 42: Virtual oscillator control: Simulation results of voltage and frequency with an increase of ϵ every 0.3 second. Note that the voltage is measured with an assumed fundamental frequency $f = 49.76$ Hz which introduces oscillations when the frequency changes.

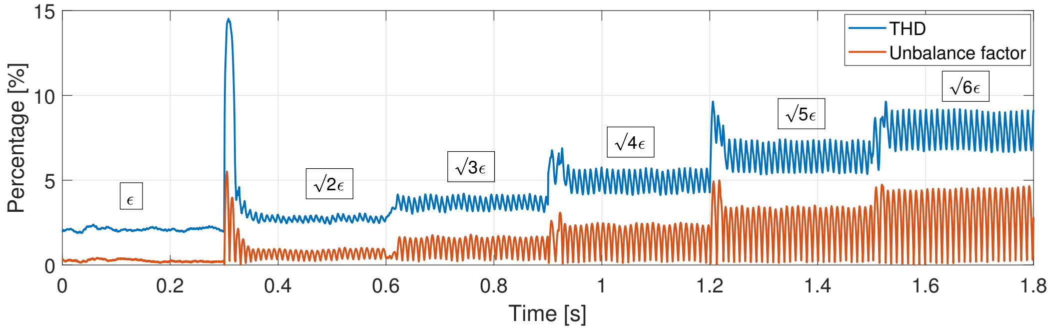

Figure 43: Virtual oscillator control: Simulation results of THD and unbalance factor with an increase of ϵ every 0.3 second. Note that the THD and ubalance factor are measured with an assumed fundamental frequency $f = 49.76$ Hz which introduces oscillations when the frequency changes.

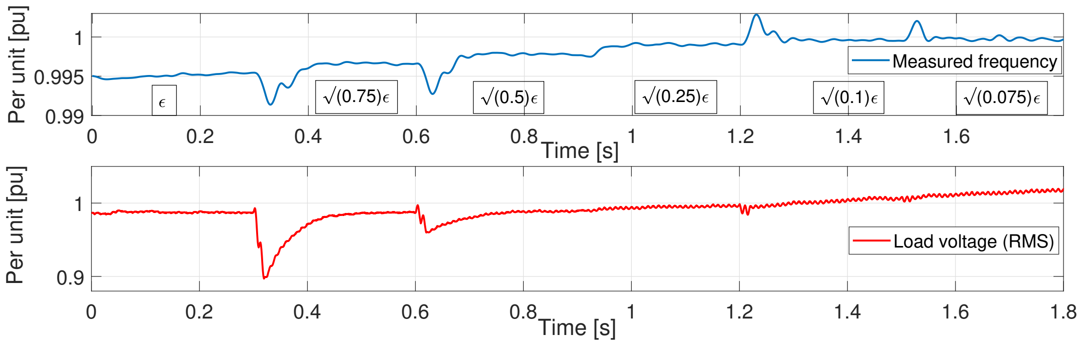

Figure 44: Virtual oscillator control: Simulation results of voltage and frequency with a reduction of ϵ every 0.3 second. The fundamental frequency is assumed to be $f = 49.76$ Hz in the measurements.

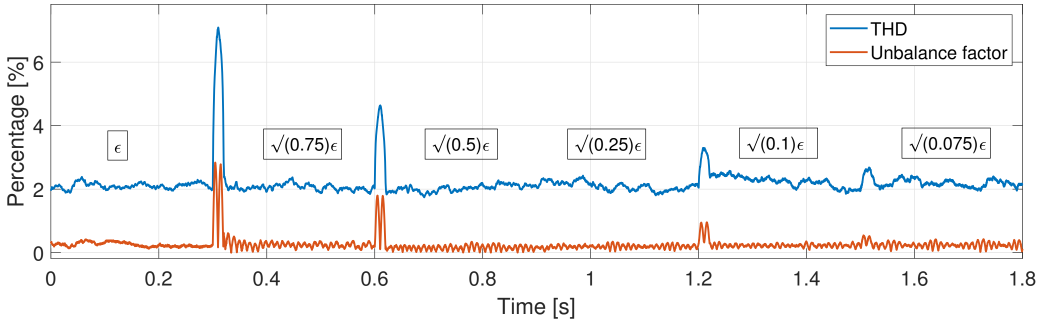

Figure 45: Virtual oscillator control: Simulation results of THD and unbalance factor with a reduction of ϵ every 0.3 second. The fundamental frequency is assumed to be $f = 49.76$ Hz in the measurements.

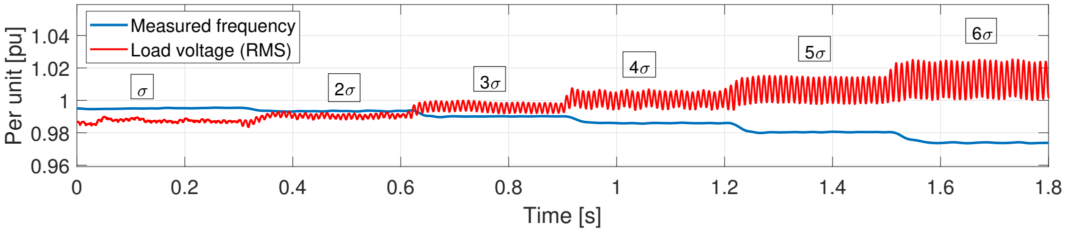

Figure 46: Virtual oscillator control: Simulation results of voltage and frequency with an increase of σ every 0.3 second. Note that the voltage is measured with an assumed fundamental frequency $f = 49.76$ Hz which introduces oscillations when the frequency changes.

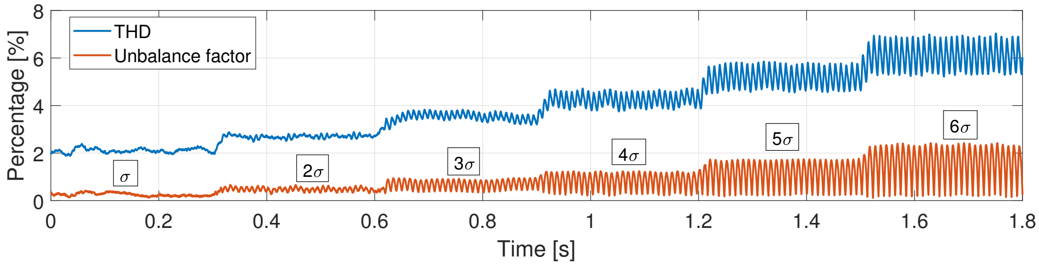

Figure 47: Virtual oscillator control: Simulation results of THD and unbalance factor with an increase of σ every 0.3 second. Note that the THD and ubalance factor are measured with an assumed fundamental frequency $f = 49.76$ Hz which introduces oscillations when the frequency changes.

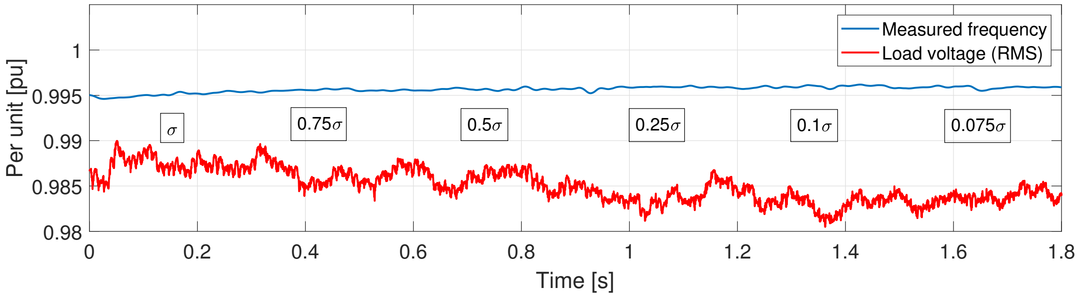

Figure 48: Virtual oscillator control: Simulation results of voltage and frequency with a reduction of σ every 0.3 second. The fundamental frequency is assumed to be $f = 49.76$ Hz in the measurements.

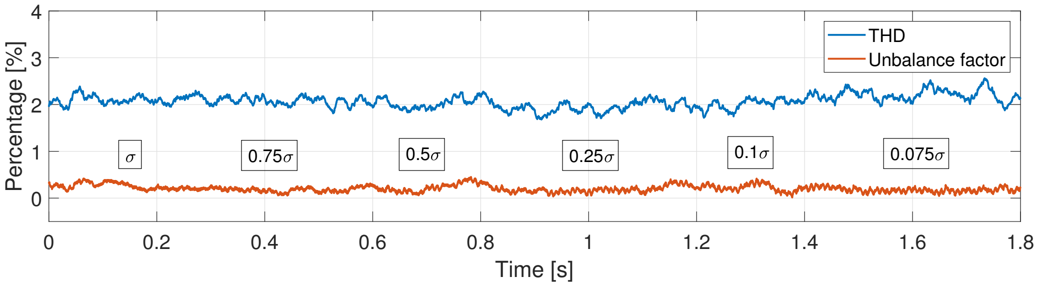

Figure 49: Virtual oscillator control: Simulation results of THD and unbalance factor with a reduction of σ every 0.3 second. The fundamental frequency is assumed to be $f = 49.76$ Hz in the measurements.

12.3 Simulink model

The microgrid and the controllers simulated in MATLAB/Simulink are included in this section.

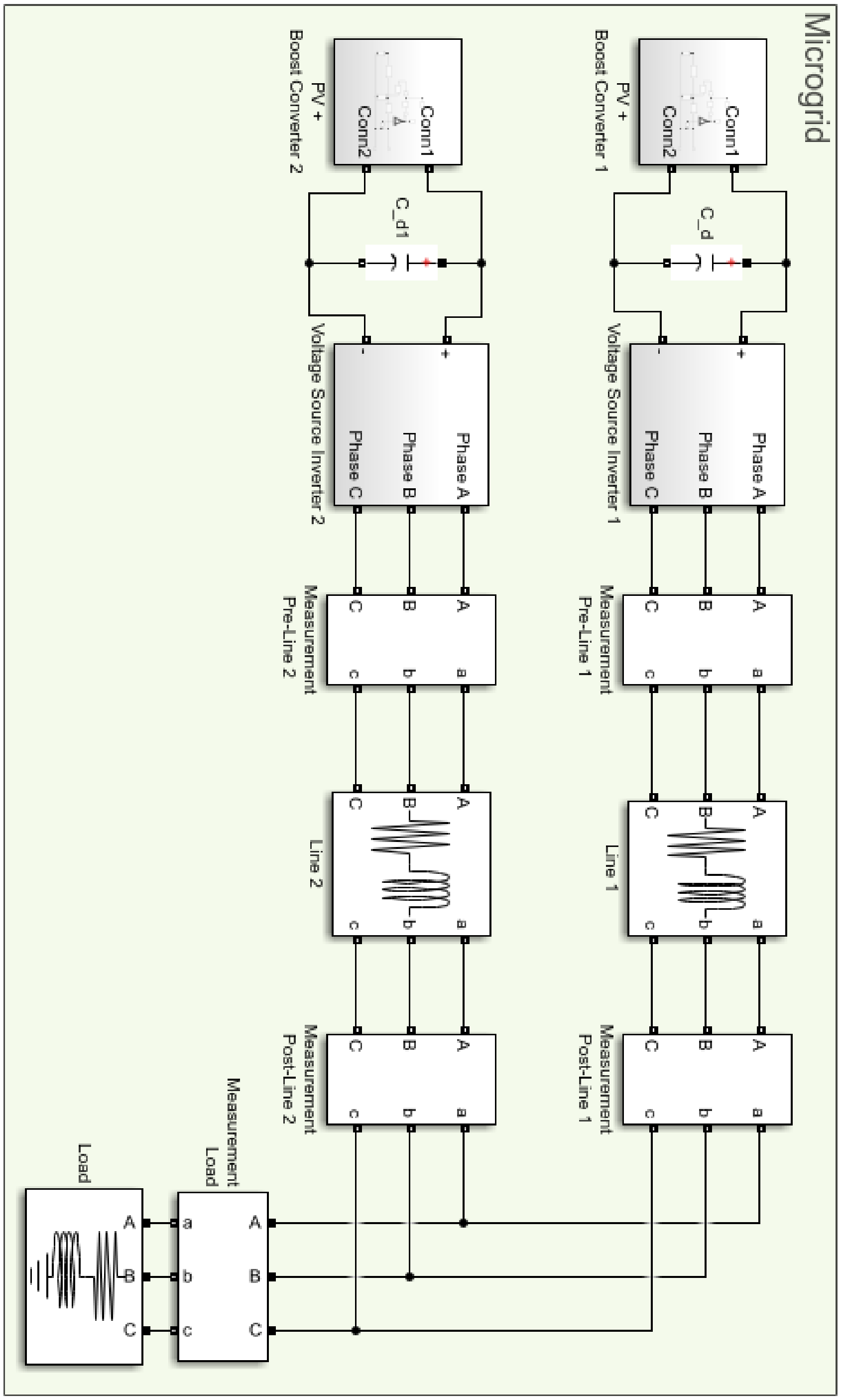

Figure 50: Simulink model: overview of the microgrid topology.

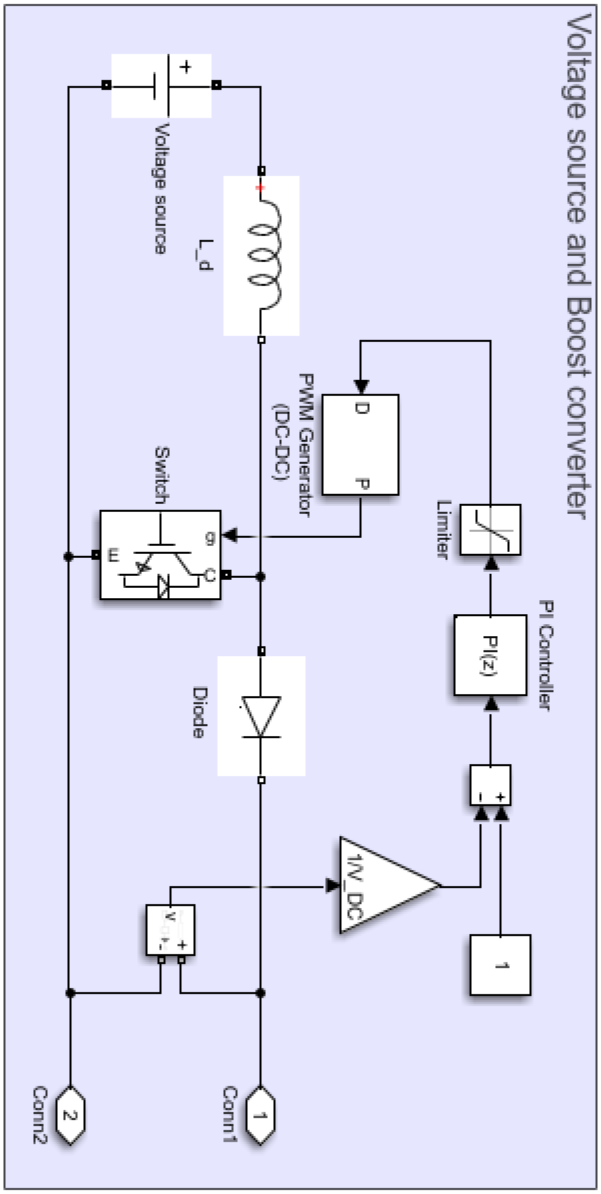

Figure 51: Simulink model: DC side of the simulation model.

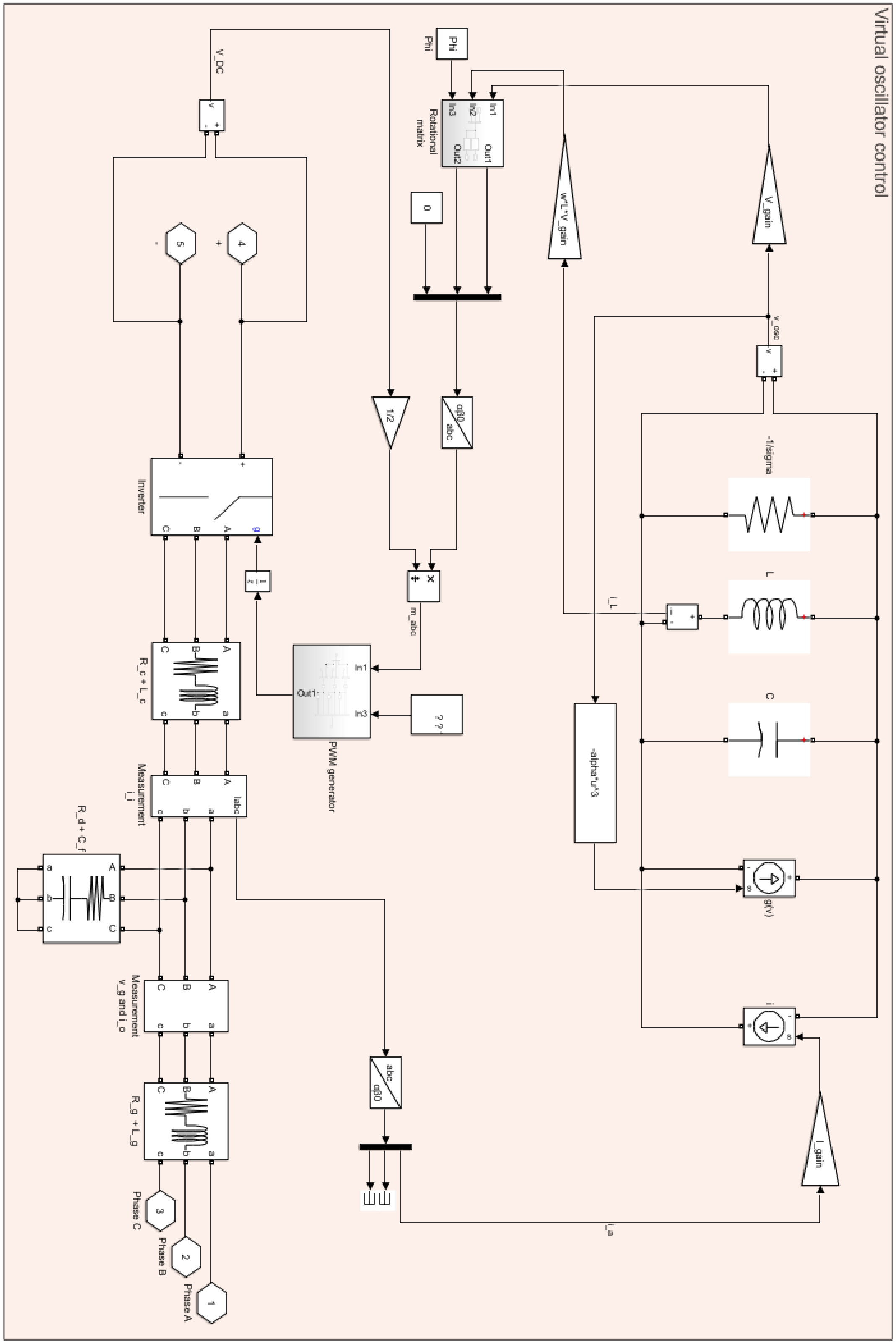

Figure 52: Simulink model: virtual oscillator controlled inverter.

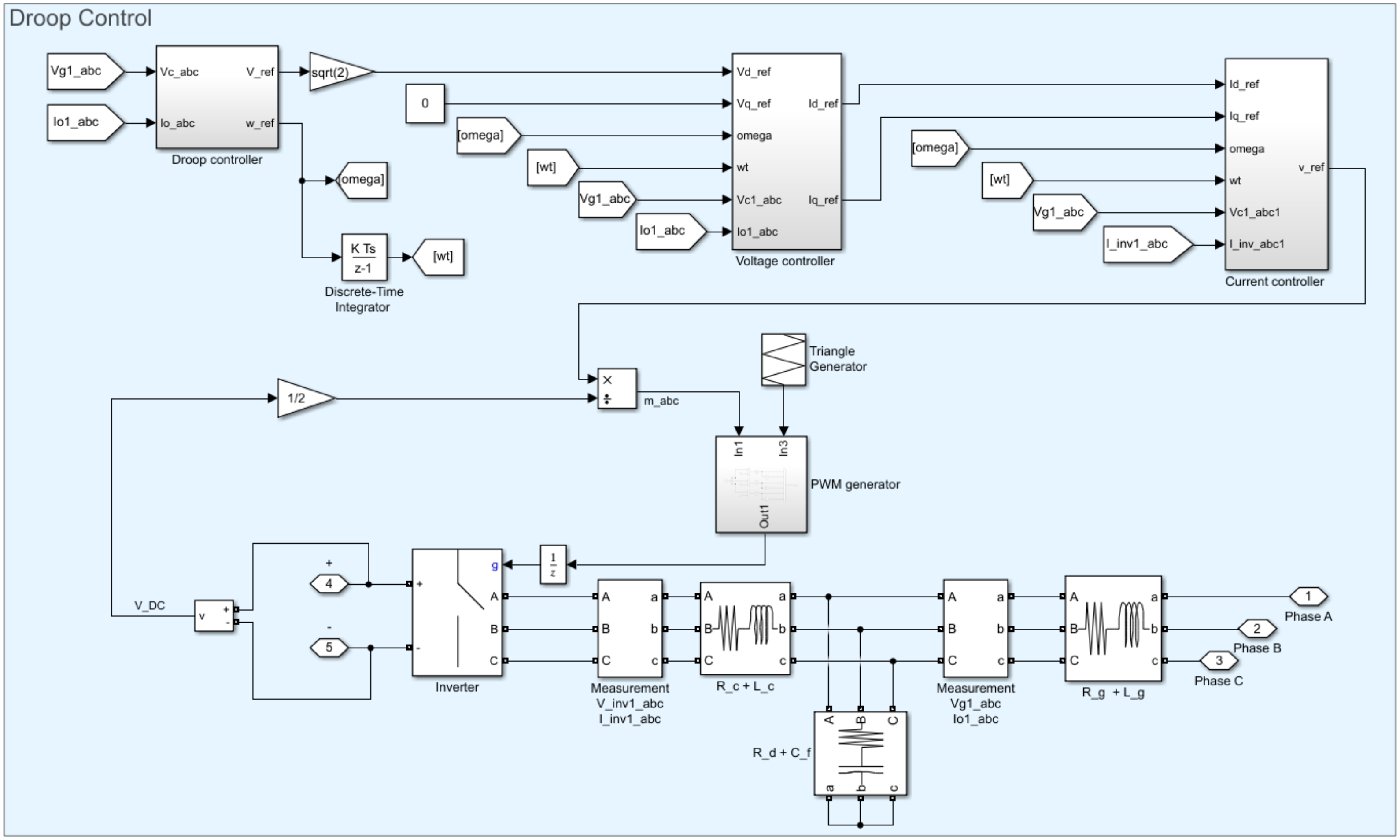

Figure 53: Simulink model: droop controlled inverter.

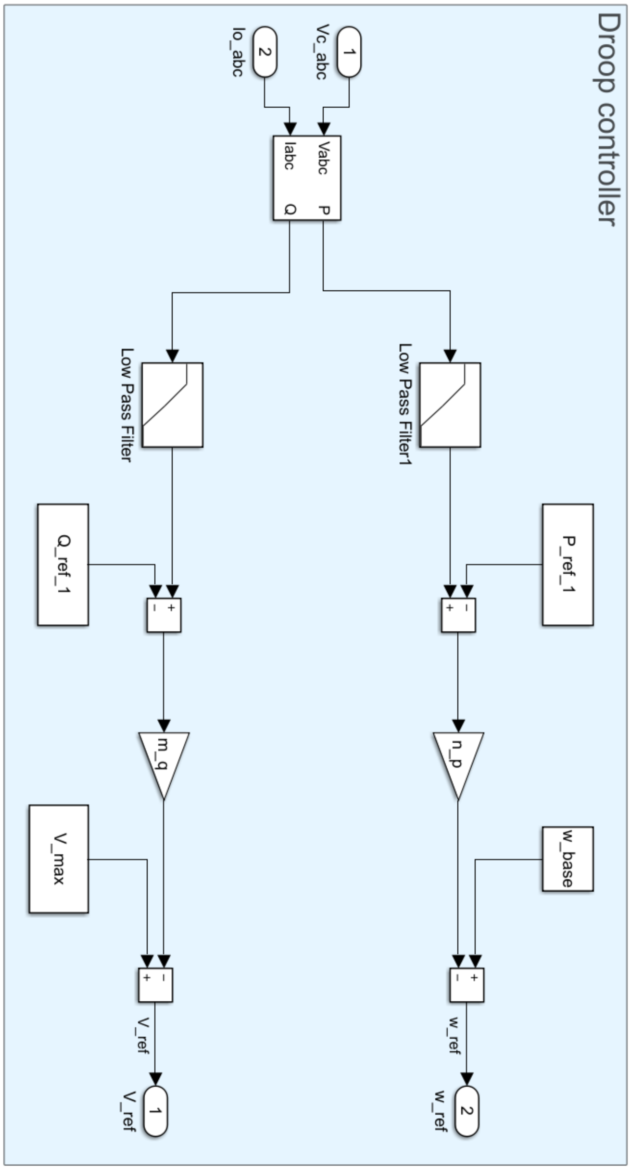

Figure 54: Simulink model: conventional droop controller.

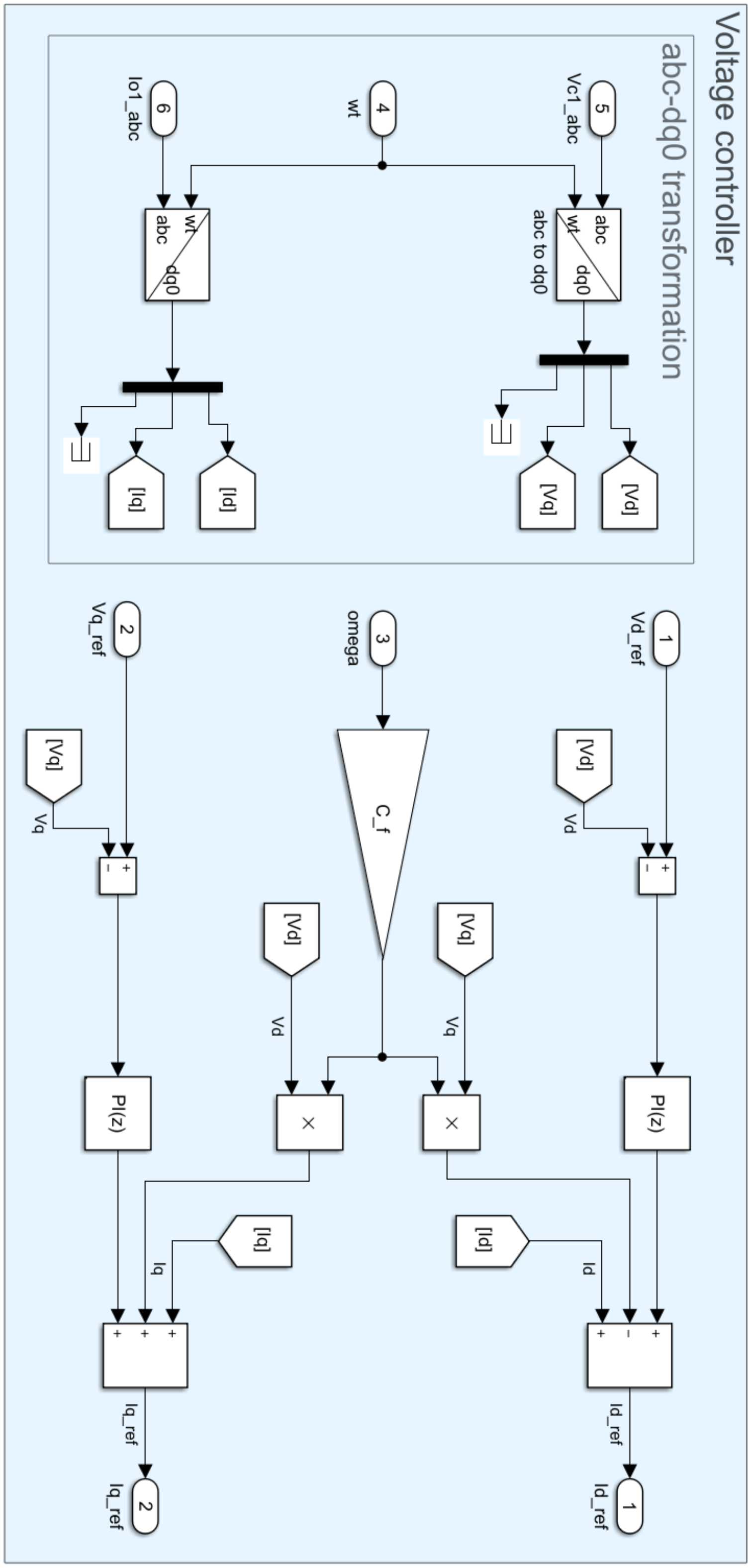

Figure 55: Simulink model: voltage controller in the droop control's inner loop.

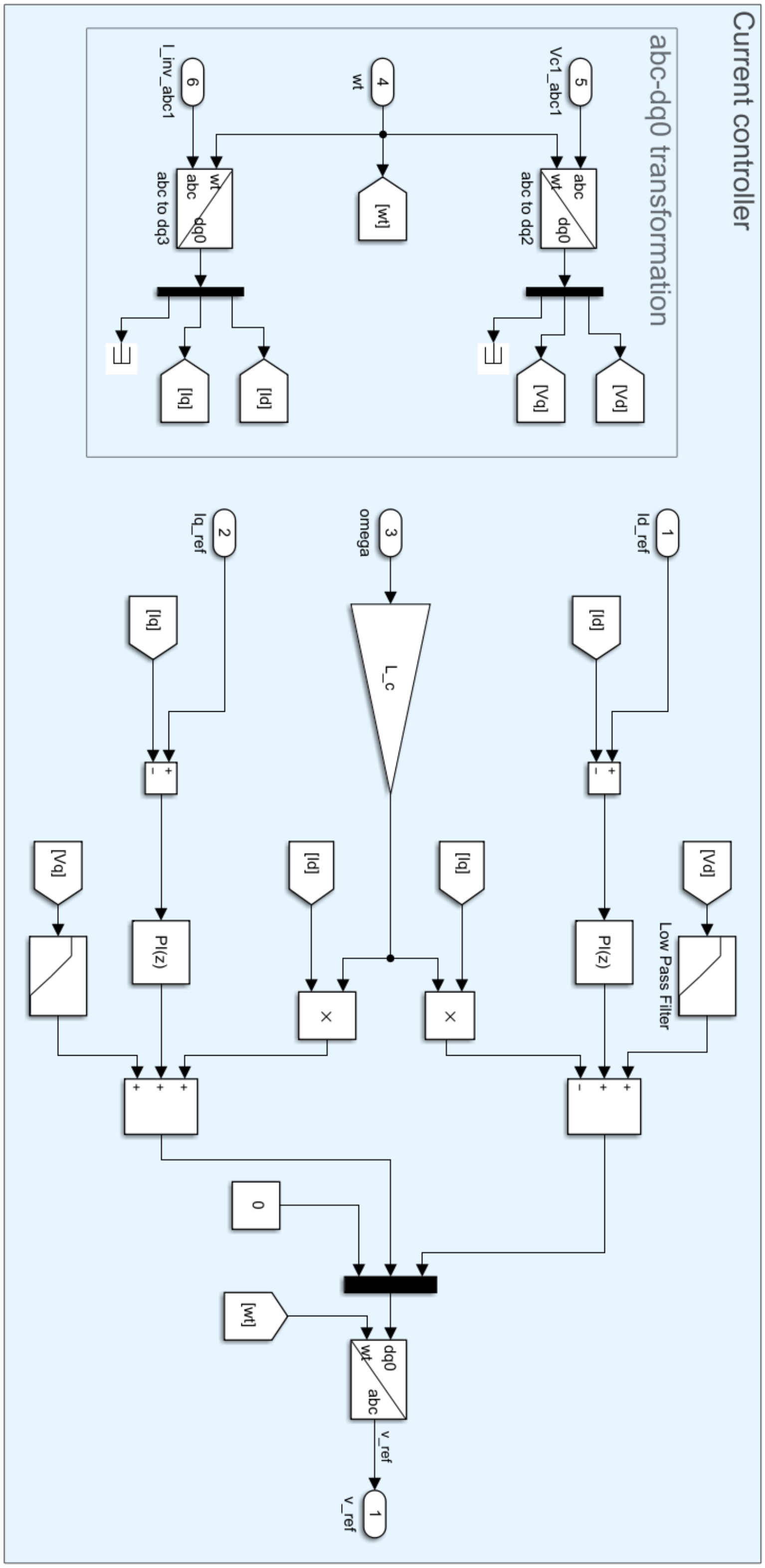

Figure 56: Simulink model: current controller in the droop control's inner loop.

12.4 MATLAB scripts

System parameters

```
%% VOC initialization
Ts = 2.5e-6; %Time step in simulation

%Parameters
V_LL = 400; %Line-Line
V_LN = V_LL/sqrt(3);
V_DC = 750;
f = 50; %Hz
w = 2*pi*f;
f_sw = 15e3;
P_rated = 10e3; %Per inverter
Q_rated = 10e3;
V_max = 1.05*V_LN;
V_min = 0.95*V_LN;
w_max = 1.005*w;
w_min = 0.995*w;

%Load
P_load = 2*0.8*P_rated;
Q_load = 2*0.2*Q_rated;

%LCL filter
L_c = 5.082e-4;
R_c = 0.3e-3;
C_f = 3.01e-5;
L_g = 3.05e-4;
R_g = 0.2e-3;
R_d = 0.84;

%DC side
V_pv = 400;
C_d = 2000e-6;
L_d = 8.29e-4;

%Line
R_line1 = 2*0.397; %Ohm/km from CIGRE benchmark LV microgird
X_line1 = 2*0.279; %Ohm/km from CIGRE benchmark LV microgird
L_line1 = X_line1/w;
R_line2 = 2*R_line1;
L_line2 = 2*L_line1;

%Base values
V_base = V_LN;
```

```
S_base = P_rated;
I_base = S_base/3/V_base;
```

Droop control

```
%Droop coefficients
DeltaW = 0.005;
DeltaV = 0.05;
n_p = DeltaW*w/P_rated; %P-f
n_q = DeltaW*w/Q_rated; %Q-f
m_p = DeltaV*V_max/P_rated; %P-V
m_q = DeltaV*V_max/Q_rated; %Q-V

%Power references
P_ref_1 = 0*P_load/2;
Q_ref_1 = 0*Q_load/2;
P_ref_2 = 0*P_load/2;
Q_ref_2 = 0*Q_load/2;

%Base values
V_base = V_LN;
S_base = P_rated;
I_base = S_base/3/V_base;

%Tuning the current control
w_0i = 2*pi*f_sw/10; %Bandwith of the current controller
rho = 1.1; %Damping coefficient
Kp_i = 2*rho*w_0i*L_c - R_c; %Proportional gain in current controller
Ki_i = w_0i^2*L_c; %Integral gain of current controller
V_filt = 1000; %1/timeconstant for filtering the voltage at the capacitor.

%Tuning the voltage controller
w_0v = w_0i/10; %Bandwidth of the voltage controller
Kp_v = 2*rho*w_0v*C_f; %Proportional gain in voltage controller
Ki_v = w_0v^2*C_f; %Integral gain in voltage controller
```

Virtual oscillator control

```
%Gain
V_gain = V_max;
I_gain = 3*V_min/Q_rated;
%Conventional or opposite droop
Phi = pi/2; %Select 0 for opposite droop or pi/2 for regular droop

%Droop coefficients translated into VOC parameters
```

```
DeltaW = 0.005;
DeltaV = 0.05;
if Phi == 0
    n_q = DeltaW*w/Q_rated; %Q-f
    m_p = DeltaV*V_max/P_rated; %P-V
    n = n_q;
    m = m_p;
elseif Phi == pi/2
    n_p = DeltaW*w/P_rated; %P-f
    m_q = DeltaV*V_max/Q_rated; %Q-V
    n = n_p;
    m = m_q;
end
sigma = 1/m * I_gain/6;
alpha = 2*sigma/3;
C = 1/n * I_gain/(6*V_gain);
L = 1/(C*(w)^2);
epsilon = sqrt(L/C);
```

NTNU
Norwegian University of
Science and Technology